

國立交通大學

材料科學與工程學系

博士論文

一維暨三維奈米結構對於電化學特性及
產氫應用的研究

Study on One- and Three-Dimensional
Nanostructures for Electrochemical
Characteristics and Hydrogen Production
Applications

研究生：林彥谷

指導教授：陳三元 博士

陳貴賢 博士

林麗瓊 博士

中華民國 九十九年 十一月

一維暨三維奈米結構對於電化學特性及產氫應用的研究

Study on One- and Three-Dimensional Nanostructures for
Electrochemical Characteristics and Hydrogen Production
Applications

研究生：林彥谷

Student : Yan-Gu Lin

指導教授：陳三元 博士

Advisor : Dr. San-Yuan Chen

陳貴賢 博士

Dr. Kuei-Hsien Chen

林麗瓊 博士

Dr. Li-Chyong Chen

國立交通大學

材料科學與工程研究所



A Dissertation

Submitted to Department of Materials Science and Engineering

College of Engineering

National Chiao Tung University

In Partial Fulfillment of the Requirements

For the Degree of

Doctor of Philosophy

in Materials Science and Engineering

November 2010

Hsinchu, Taiwan, Republic of China

中華民國 九十九年 十一月

中文摘要

由於對石化燃料的依賴導致近來發生的能源危機，從事發展新穎奈米結構材料在乾淨能源方面之應用變成非常重要的研究。本論文首先利用化學氣相沉積法所製備出垂直陣列之摻氮奈米碳管擁有獨特的微結構和電化學特性，藉由微結構、鍵結、電子轉移行為以及後續白金觸媒的電化學沉積等探討摻氮對於奈米碳管之影響。發現摻氮奈米碳管所形成的表面缺陷，導致近乎逆的電子轉移，並提供白金粒子於奈米碳管表面的成核點以應用於燃料電池。接著研發三種不同的奈米結構，即銅奈米粒子/氧化鋅奈米棒之奈米複合材料、微波活化氧化銅奈米針尖/氧化鋅奈米棒之奈米複合材料以及氧電漿活化氧化銅-氧化鋅之反蛋白石複合結構，以作為微型重組器的觸媒。首先使用銅奈米粒子/氧化鋅奈米棒之奈米複合材料為觸媒可於低重組溫度下(250 °C)達到高甲醇轉換率(93%)、高氫產率(183 mmol g_{cat}⁻¹ h⁻¹)、低一氧化碳濃度(170-210 ppm)。這可歸因於銅奈米粒子之高表面積和分散性、銅物種的電子結構被修飾以及金屬-承載體間存在強烈的交互作用。接著以微波處理對於氧化銅奈米針尖/氧化鋅奈米棒之奈米複合材料，證明可明顯改善甲醇重組反應之催化性能，此可歸因於氧化銅/氧化鋅界面處有缺陷形成與強交互作用力產生。然後利用氧電漿處理製備出含有高濃度氧空缺之氧化銅-氧化鋅反蛋白石複合結構，以提升甲醇重組反應的催化性能，即可於更低重組溫度下(230 °C)達到接近完全甲醇轉換率、高氫產率、低一氧化碳濃度與出色的穩定性。最後，利用碳改質之氧化鋅反蛋白石結構以作為光電化學分解水產氫的光電極。藉由加熱氧化鋅和聚苯乙烯蛋白石模板，可以直接在 ITO 基板上合成出碳嵌入氧化鋅基材的反蛋白石結構。於光子轉換成電流的量測中，相較於純氧化鋅結構在可見光波段，碳改質之氧化鋅反蛋白石結構其光反應表現出顯著的增加。於照明功率密度為 100 mW/cm² 下，碳改質之氧化鋅反蛋白石結構表現出高光電流密度(1 mA/cm²)與高光子轉換成氫的效率(0.75%)。這些結果顯示出碳改質之氧化鋅反蛋白石結構，具有應用於光電化學分解水的潛力。

關鍵字：奈米碳管，氧化鋅，銅，甲醇重組，氫，水分解

Abstract

There has become of interest in the development of novel and nanostructured materials for the application of clean energy. Part I is focused on “Effects of *in-situ* Nitrogen-doping on the microstructure and electrochemical activity of carbon nanotubes”. In this work, the CN_x NTs doped with an optimal N concentration resulted in a nearly reversible ET behavior due to uniform and high density of surface defects which are desirable for further nucleation of Pt particles on the surface of CN_x NTs to form a composited electrode for electrochemical energy device applications such as fuel cells and capacitors. In Part II, we have developed three kinds of different nanostructures, i.e. Cu nanoparticle (NP)/ZnO nanorod (NR) nanocomposites, microwave-activated CuO nanotip/ZnO NR nanocomposites, and O_2 plasma-activated CuO-ZnO inverse opals, for high efficiency of microreformer applications. The first one, high conversion of methanol (93%), high hydrogen production rate ($183 \text{ mmol g}_{\text{cat}}^{-1} \text{ h}^{-1}$), low CO formation (170-210 ppm), and good stability at a low-reformation temperature of $250 \text{ }^\circ\text{C}$ have been achieved for Cu NP/ZnO NR nanocomposites. The superb catalytic performance of the Cu NP -decorated ZnO NR nanostructures can be attributed to the larger surface area and enhanced dispersion of fine Cu NPs, formation of microstrain, the modification of electronic structure of Cu species, and the existence of strong metal-support interaction (SMSI) effect. The second one, microwave treatment to CuO nanotip/ZnO NR nanocomposites has been demonstrated to remarkably improve the catalytic performance in methanol reforming reaction. Comparative to conventional thermal annealing, microwave treatment significantly enhances the catalytic activity of the catalysts, which might be attributed to defect formation, i.e. microstrain, and strong interaction in CuO/ZnO interface. The third one, we report the use of oxygen vacancies-rich Cu-ZnO inverse opals via O_2 plasma treatment to further enhance the catalytic performance of methanol reforming

reaction at a low-reaction temperature of only 230 °C, yielding nearly complete conversion of methanol, ultrahigh hydrogen production rate, ultralow CO formation, and outstanding stability.

For the last Part III, we reported the simple synthesis of carbon-modified ZnO inverse opals, and their implementation as photoelectrodes in photoelectrochemical (PEC) cells for hydrogen generation from water splitting. The *in-situ* incorporating carbon into the ZnO matrix was synthesized directly on the ITO substrate through annealing of the blends of ZnO and polystyrene-opal template. Incident-photon-to-current-efficiency measurements carried out on PEC cell with carbon-modified ZnO inverse-opal photoanodes demonstrate a significant increase of photoresponse in the visible region compared to pure ZnO structures. Upon illumination at a power density of 100 mW/cm², carbon-modified ZnO inverse-opals show high photocurrent density of 1 mA/cm² with photon-to-hydrogen conversion efficiency of 0.75%. These results suggest substantial potential of carbon-modified ZnO inverse opals in PEC water splitting applications.

Keywords: carbon nanotube, zinc oxide, copper, methanol reforming, hydrogen, water splitting

Acknowledgments

在結束博士班生涯之際，首先要感謝指導教授陳三元博士與工研院鄭世裕博士，當初是你們的鼓勵並帶領我走向博士班的研究之路，使我有機會在博士班生涯裡繼續砌築知識之磚；同時，衷心感謝另外兩位指導教授台大凝態中心林麗瓊博士與中研院原分所陳貴賢博士，給我無限的機會和支持，讓我在研究的道路上可以盡情的發揮。除了感謝老師們讓我學習到正確作研究的方法與態度外，我也從老師們身上學習到很多做人處事的道理，這些都是書本上沒有教的！如果沒有你們的提攜與支持，我是不可能拿到博士學位的，謝謝你們！

此外，感謝台大 AML 實驗室的夥伴：徐裕奎博士、韓謝忱博士、裕凱、盈竹、逸帆、文勳、宜蓁、創年、昀紘和茹蘭，共享研究瓶頸之苦與休閒郊遊之樂；另外，也感謝交大實驗室的學長姐與學弟妹在過去給予的幫忙和協助在此一併致謝！

最後，我要感謝我的父母親，感謝他們多年來的茹苦養育與默默的支持付出，謝謝！！

Contents

中文摘要	I
Abstract	II
Acknowledgments	IV
Contents	V
Figure Captions	VII
Table Captions	XII
Chapter 1 introduction	1
Chapter 2 Literature Review	7
2.1 Direct methanol fuel cell	7
2.1.1 Catalyst supported on carbon nanotube	10
2.2 Methanol reforming	11
2.3 Photoelectrochemical water splitting	15
2.3.1 PEC hydrogen generation based on nanomaterial photoelectrodes ...	18
Chapter 3 Experiment Methods	28
3.1 Flowchart of experiment process	28
3.2 Preparation of nanomaterials	29
3.2.1 Synthesis of CN _x NTs and Pt NPs deposition	29
3.2.2 Fabrication of ZnO NRs and metallic Cu NPs deposition	29
3.2.3 Synthesis of microwave-activated CuO NT/ZnO NR nanocomposites	30
3.2.4 Preparation of O ₂ plasma-activated CuO-ZnO inverse opals	31
3.2.5 Preparation of carbon-modified ZnO inverse opals	32
3.3 Experimental measurements and characteristics analysis	33
Chapter 4 Effects of Nitrogen-Doping on the Microstructure, Bonding and Electrochemical Activity of Carbon Nanotubes	38
4.1 Introduction	38
4.2 Microstructure and Bonding of Nitrogen-Doped Carbon Nanotubes	39
4.3 Nitrogen-Doping Effect on Electrochemical Activity	43
4.4 Summary	47
Chapter 5 Nanostructured ZnO Nanorod@Cu Nanoparticle as Catalyst for Microreformers	56
5.1 Introduction	56
5.2 Structural Characterization of Cu Nanoparticle/ZnO Nanorod Nanocomposites	57
5.3 Test of Methanol Reforming Reaction	63
5.4 Summary	65
Chapter 6 Microwave-Activated CuO Nanotip/ZnO Nanorod Nanoarchitectures for Efficient Hydrogen Production	75

6.1 Introduction.....	75
6.2 Structural Characterization of CuO Nanotip/ZnO nanorod Nanocomposites.....	76
6.3 Test of Methanol Reforming Reaction.....	79
6.4 Summary.....	82
Chapter 7 O₂ Plasma-activated CuO-ZnO Inverse Opals as High-performance Methanol Microreformer	89
7.1 Introduction.....	89
7.2 Structural Characterization of O ₂ Plasma-treated CuO-ZnO Inverse Opals.....	92
7.3 Test of Methanol Reforming Reaction.....	96
7.4 Summary.....	98
Chapter 8 Enhance Photocatalytic Activity with Carbon-Modified ZnO Inverse Opals for Solar Water-Splitting	108
8.1 Introduction.....	108
8.2 Structural Characterization of Carbon-modified ZnO Inverse Opals	111
8.3 Test of Photoelectrochemical Reaction.....	113
8.4 Summary.....	115
Chapter 9 Conclusions.....	123
9.1 Effects of Nitrogen-Doping on the Microstructure, Bonding and Electrochemical Activity of Carbon Nanotubes	123
9.2 Novel Copper-Zinc Oxide Nanoarchitectures as Microreformation Catalysts for Hydrogen Production	123
9.3 Enhanced Photocatalytic Activity with Carbon-Modified ZnO Inverse Opals for Solar Water-Splitting.....	124
References.....	126
Curriculum Vitae	134
Publications	135

Figure Captions

Figure 2.1 Schematic operating principles of DMFC.....	21
Figure 2.2 Breakdown of anode, cathode, and electrolyte-related performance losses in a DMFC	21
Figure 2.3 Schematic illustration of the synthesis procedure of the composite.....	22
Figure 2.4 TEM images of Pt/CNT (inset: enlarged image).....	22
Figure 2.5 TEM images of 20 wt% PtRu/C nanocatalyst prepared with different molar ratios of Pt:Ru (a) LRTEM of 1:1, (b) HRTEM of 1:1	23
Figure 2.6 Typical TEM image of the CNT/PyPBI/Pt. Pt nanoparticles are loaded homogeneously on the PyPBI wrapped CNTs.....	23
Figure 2.7 Schematic diagram of the integrated methanol steam reformer system.....	24
Figure 2.8 Schematic of a typical PEC device and its basic operation mechanism for hydrogen generation from water splitting.....	25
Figure 2.9 Energy diagram of a PEC cell consisting of an n-type SC photoanode and a metal cathode for water splitting.....	25
Figure 2.10 Type of photoelectrode for PEC water splitting (SC-semiconductor; M-metal)	26
Figure 2.11 (a) Schematic representation of the electron transport through spherical particles and nanorods. (b) A schematic of a Fe ₂ O ₃ photoanode for water splitting. The small diameter of the nanowires ensures a short hole diffusion length	27
Figure 3.1 Schematic diagram of microwave-plasma enhanced chemical-vapor deposition (MPECVD) facility	35
Figure 3.2 Schematic diagram of electrochemical deposition facility.....	35
Figure 3.3 ZnO array preparation	36
Figure 3.4 Cu NP/ZnO NR nanocomposites preparation	36
Figure 3.5 Cu NT/ZnO NR nanocomposites preparation	37
Figure 3.6 Procedure for the preparation of CuO-ZnO inverse opals using polystyrene colloidal crystal templates.....	37
Figure 4.1 Cross-sectional SEM images of the vertically aligned CNTs synthesized at different flow rate of N ₂ : (a) 0, (b) 80, and (c) 120 sccm	49
Figure 4.2 (a) Comparison of the peak intensities and the full width at half maximum (FWHM) of the first-order Raman spectra for the vertically aligned CN _x NTs prepared with different N ₂ flow rate during growth. (b) D-band position as a function of N ₂ flow rate. (c) I_D/I_G as a function of N ₂ flow rate.....	50
Figure 4.3 (a) The C1s XPS spectra of the vertically aligned CNTs prepared with various N ₂ flow rate during growth. The inset is the FWHM of the C-N bonding component as a function of N ₂ flow rate. (b) The N1s XPS spectra	

of the vertically aligned CNTs prepared with different N ₂ flow rate. (c) The I_P and I_G as a function of the N ₂ flow rate for the N1s peak. (d) The N-doping concentration as a function of the N ₂ flow rate	51
Figure 4.4 (a) Cyclic voltammetry of the vertically well-aligned CNTs modified with different N-doping level in 1 M KCl and 5 mM K ₄ Fe(CN) ₆ . (b) The ferricyanide peak current versus the scan rate (v) ^{1/2} plot for CNTs using various flow rate of N ₂ for both anode and cathode. (★: 0 sccm, ■: 40 sccm, ●: 80 sccm, ◆: 120 sccm, ▲: 160 sccm) The inset shows the roughness factor as a function of the N ₂ flow rate. (c) The potential separation as a function of the N ₂ flow rate	52
Figure 4.5 AC impedance analysis of the vertically aligned CNTs with different N-doping level in 1 M KCl and 5 mM K ₄ Fe(CN) ₆ . The inset shows the internal resistance as a function of the N ₂ flow rate	53
Figure 4.6 TEM images of the Pt NP-CN _x NT hybrid nanostructures synthesized at different flow rate of N ₂ : a) 0, b) 40, and c) 120 sccm	54
Figure 4.7 Typical CV curve of the arrayed Pt NP-CN _x NT nanocomposites with different N ₂ flow rate at a scan rate of 50 mV/s in 1 M CH ₃ OH + 1 M H ₂ SO ₄ solution	55
Figure 5.1 Schematic diagram of the novel catalyst ZnO NR@Cu NP arrays grown on the inner surface of microchannel reactor	66
Figure 5.2 Photographs of the microchannels a) before and b) after homogeneously depositing the ZnO NR@Cu NP nanocomposites	66
Figure 5.3 a) Cross-sectional SEM image of vertically well-aligned ZnO NRs. b) Typical TEM image of a single ZnO NR showing the presence of stacking faults as marked with arrows. c) HRTEM image of the ZnO NR. d) Typical TEM image of the ZnO NR@Cu NP nanocomposites. e) HRTEM image of Cu NPs on the surface of one single ZnO NR. f) The size histogram of Cu NPs analyzed from the HRTEM image	67
Figure 5.4 a) TEM image and corresponding EDX elemental mapping of b) Cu and c) Zn	68
Figure 5.5 HRTEM image of ZnO NR@Cu NP heterostructures	69
Figure 5.6 a) XRD patterns of Cu NPs on the surface of ZnO NRs prepared with different decoration concentrations from 1 to 3 mM. b) Cu 2p XPS core level spectra of arrayed ZnO NR@Cu NP nanocomposites prepared with different Cu decoration concentrations from 0.5 to 3 mM. c) Cu K-edge XANES spectra of arrayed ZnO NR@Cu NP nanocomposites and bulk reference sample Cu foil. d) Comparative TPR profiles of ZnO NR@Cu NP nanocomposites and commercial catalysts (MDC-3: Sud-Chemie)	70
Figure 5.7 Large range of XRD patterns of Cu NPs on the surface of ZnO NRs prepared with different decoration concentrations from 1 to 3 mM. Peaks	

marked with ▲ are due to ZnO, the other marked with ■ is due to Cu	71
Figure 5.8 First derivative of the Cu K-edge XANES spectra of arrayed ZnO NR@Cu NP nanocomposites and bulk reference sample Cu foil	72
Figure 5.9 a) Methanol reforming reaction profiles for 2 mM arrayed Cu NPs/ZnO NRs nanocomposites (□) and commercial catalysts (●). b) Hydrogen production rate as a function of reaction temperature for 2 mM arrayed Cu NPs/ZnO NRs nanocomposites (□) and commercial catalysts (●). c) Kinetic constants as a function of reaction temperature for 2 mM arrayed Cu NPs/ZnO NRs nanocomposites (□) and commercial catalysts (●). d) Arrhenius plots for methanol reforming reaction for 2 mM arrayed Cu NPs/ZnO NRs nanocomposites (□) and commercial catalysts (●). Reaction conditions: H ₂ O/O ₂ /MeOH = 1/0.125/1, W/F = 21 kg _{cat} s mol ⁻¹ _{methanol}	73
Figure 5.10 Stability tests in methanol reforming reaction over 2 mM arrayed Cu NPs/ZnO NRs nanocomposites (□) and commercial catalysts (○). Reaction conditions: H ₂ O/O ₂ /MeOH = 1/0.125/1, Temperature = 250 °C, W/F = 21 kg _{cat} s mol ⁻¹ _{methanol}	74
Figure 6.1 (a) SEM images of CuO nanostructures (inset: high magnification). (b) SEM images of CuO NT/ZnO NR catalyst precursors (inset: high magnification)	83
Figure 6.2 HRTEM image of CuO nanodandelions, showing specific structural information about an individual nanosheet grown along the [11 $\bar{1}$] direction	83
Figure 6.3 (a) TEM and (b) HRTEM images of CuO NT/ZnO NR catalyst precursors, showing that NTs not only adhere to NR but also directly conjoin with the NR	84
Figure 6.4 (a) X-ray diffraction, (b) micro-Raman, (c) X-ray photo-electron spectroscopy, and (d) TPR spectra of the as-prepared, after thermal treatment, and after MW treatment CuO NT/ZnO NR catalyst precursors	85
Figure 6.5 HRTEM image of one single CuO NT, clearly showing a highly distorted lattice (indicated by the circle) as a result of MW irradiation	86
Figure 6.6 Methanol reforming reaction profiles : (a) Methanol conversion rate and (b) hydrogen production rate for Cu NTs/ZnO NRs working catalysts : as-prepared (■), after thermal treatment (◆), and after MW treatment (▲). Reaction conditions: H ₂ O/O ₂ /MeOH = 1/0.125/1, W/F = 21 kg _{cat} s mol ⁻¹ _{methanol} . (c) Stability test in MRR over MW-treated Cu NT/ZnO NR working catalysts at H ₂ O:O ₂ :MeOH = 1:0.125:1, Temperature = 250 °C, and W/F = 21 kg _{cat} s mol ⁻¹ _{methanol}	87
Figure 6.7 (a) Cu K-edge XANES and (b) Cu K-edge EXAFS of CuO NT/ZnO NR	

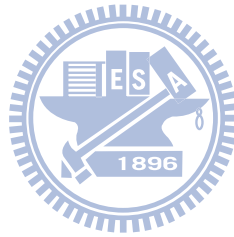
catalyst precursors with MW irradiation, MW-treated Cu NT/ZnO NR working catalysts, and MW-treated Cu NT/ZnO NR working catalysts after continuously operating 60 hours for MRR	88
Figure 7.1 Schematic diagram of the novel catalyst CuO-ZnO inverse opals fabricated on the inner surface of microchannel reactor.....	100
Figure 7.2 Procedure for the preparation of CuO-ZnO inverse opals using polystyrene colloidal crystal templates.....	100
Figure 7.3 (a) SEM image and (b) HRTEM image of CuO-ZnO 3DOM nanoarchitectures. (c) Micro- Raman spectra of CuO-ZnO inverse opals with different O ₂ -plasma exposure durations	101
Figure 7.4 N ₂ adsorption-desorption isotherm and pore-size distribution (inset) of CuO-ZnO inverse opals without O ₂ -plasma treatment	102
Figure 7.5 (a) TEM image of CuO-ZnO inverse opals. Corresponding energy-filtered TEM (b) copper and (c) zinc mapping images of CuO-ZnO inverse opals	103
Figure 7.6 Relative ratio of the integrated 575 cm ⁻¹ peak intensity to the sum of the 438 and 575 cm ⁻¹ peaks as a function of O ₂ -plasma exposure time for CuO-ZnO inverse opals	104
Figure 7.7 XPS spectra of (A) O 1s, (B) Cu 2p, and (C) Zn 2p _{3/2} transitions for CuO-ZnO 3DOM nanoarchitectures after O ₂ -plasma treatment for (a) 0, (b) 3, (c) 5, (d) 10, and (e) 15 min, respectively.....	105
Figure 7.8 (a) Rates of Methanol conversion and H ₂ production for Cu-ZnO catalysts with dense film, inverse opal, and O ₂ -plasma treated inverse opal nanostructure, respectively. (b) Stability tests of MRR with O ₂ -plasma treated Cu-ZnO inverse opal for plasma exposure time of 10 min (◇) and commercial catalysts (○). Reaction conditions: H ₂ O/O ₂ /MeOH = 1/0.125/1, Reaction temperature = 230 °C, W/F = 21 kg _{cat} s mol ⁻¹ _{methanol}	106
Figure 7.9 Cu K-edge X-ray absorption near-edge spectroscopy (XANES) of O ₂ -plasma treated CuO-ZnO inverse opals and O ₂ -plasma treated CuO-ZnO inverse opals after H ₂ reduction. From XANES analysis, after H ₂ reduction of O ₂ -plasma treated CuO-ZnO inverse opals, all the CuO will turn to metallic Cu	106
Figure 7.10 SEM image of Cu-ZnO catalysts with non-inverse opal nanostructure.	107
Figure 8.1 (a) SEM image and (b) HRTEM image of carbon-modified ZnO inverse opals. (c) Bright-field and (d) Z-contrast TEM images of carbon-modified ZnO inverse opals	117
Figure 8.2 (a) Typical TEM image of carbon-modified ZnO inverse opals. Corresponding energy-filtered TEM (b) oxygen mapping image of carbon-modified ZnO inverse opals. (c) XPS spectrum of C 1s peak of	

carbon-modified ZnO inverse opals. (d) Zn K-edge EXAFS spectra of carbon-modified ZnO inverse opals and pure ZnO structures.....	118
Figure 8.3 O K-edge XAS spectra of carbon-modified ZnO inverse opals and pure ZnO structures.....	119
Figure 8.4 (a) Measured IPCE spectra of carbon-modified ZnO inverse opals in the region of 300 to 800 nm at a potential of +0.25 V (vs. Pt) in two-electrode system. (b) Linear sweep voltammograms, collected at a scan rate of 10 mV/s at applied potentials from -0.19 to +1.0 V (vs. Ag/AgCl) for carbon-modified ZnO inverse opals in the dark, ZnO noninverse-opal structures, and carbon-modified ZnO inverse opals at 100 mW/cm ² . (c) Photoconversion efficiency of the PEC cell with carbon-modified ZnO inverse opal photoelectrode as a function of applied potential. (d) Amperometric I-t curves of the carbon-modified ZnO inverse opals collected at a potential of +1.0 V (vs. Ag/AgCl) for 5 h.....	120
Figure 8.5 UV-vis spectra of carbon-modified ZnO inverse opals showing a slight red shift of absorption wavelength to the visible region.....	121
Figure 8.6 Schematic diagram representing the charge-transfer process of the carbon-modified ZnO inverse opals.....	122



Table Captions

Table 2.1 Reactor temperature ranges for initial processing of different fuels and CO content of different process streams after the initial reaction	24
Table 5.1 Microstructure properties of Cu NPs on the surface of ZnO NRs prepared with different decoration concentrations	72



Chapter 1

Introduction

Global climate warming and environment pollution have stimulated scientists to develop new high-efficient and environmental-friendly energy technologies.[1] In recent years, fuel cell (FC) research and development have received much attention due to their higher energy conversion efficiency and lower or zero greenhouse gas emissions than thermal engines in the process of converting fuel into usable energies.[2] There are many different types of FCs, with the principle differences between them being the type of electrolyte and/or fuel that they use.[3] For instance, a proton exchange or polymer electrolyte membrane FC (PEMFC) and a direct methanol FC (DMFC) may have the same solid polymer electrolyte, but the DMFC uses liquid methanol for fuel whereas the PEMFC uses gaseous hydrogen. Among the various types of FCs, DMFC and PEMFC are being in the forefront stage, and have drawn a great deal of attention in both fundamental and application.

The use of methanol as energy carrier and its direct electrochemical (EC) oxidation in DMFCs represents an important challenge for the FC technology, since the complete system would be simpler without a reformer and reactant treatment steps.[4] In addition to the crossover problem of methanol from anode to cathode

side through the proton-exchange membrane, the poor kinetics of the anode reaction is one of the major issues in the development of DMFC. In order to achieve a sufficient reaction rate at low working temperature, the DMFC electrodes typically contain expensive noble metal catalysts, such as Pt. Quite a lot of promising approaches and results have been reported for the reduction of Pt loading through supporting tactics, such as high surface area carbon materials.[5] However, it is very difficult to maintain or improve catalyst layer performance when the loading of Pt catalyst is reduced. In order to achieve high catalytic performance of FCs with the low loading of Pt, great effort must be put on Pt utilization and the enhancement of catalyst activity. Of the several factors which influence electrocatalytic activity of carbon-supported Pt catalysts, particle size, dispersion, and structural effects, are of crucial importance.[4] The Pt-carbon support interaction has recently been paid more and more attention, e.g. the growth, the structure, and the dispersion of Pt particles on the carbon supports, thus providing the potential benefits to the improvement of catalytic properties and stability of the electrocatalyst.[5] In the past we have introduced heteroatom dopant such as nitrogen (N) *in-situ* during the carbon nanotube (CNT) growth and found it effective not only to change the atomic structure of the CNTs into bamboo like, but also to improve their EC performance down the road.[6,7] Although many reports on N-doped carbon nanotubes (CNx NTs) are available in the literature, the role of N-doping in CNT and its resultant

functionality is still not clearly understood.[8-10] Therefore, we first aims to understand the effect of N incorporation in CNTs on the morphology, microstructure, electronic states, and EC properties, which will be discussed in Chapter 4 in this thesis. Subsequent loading of Pt nanoparticles (NPs) on the CN_x NTs to study the correlation of N doping with surface defect density and distribution has also been carried out.

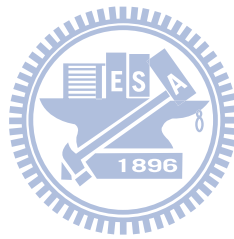
On the other hand, PEMFCs are a suitable power generation device for small scale and transport applications.[11] Hydrogen is an ideal fuel for PEMFCs, because it is lightweight, has high chemical energy, and forms water upon oxidation that is environmentally benign. However, direct-hydrogen FC is almost impossible to develop, because storage and transportation of hydrogen remains a severe problem.[11] Therefore, it is of significance to develop onsite hydrogen-generation methods for portable applications. One of the promising ways to generate hydrogen onsite for practical use is reforming of hydrocarbon fuels, e.g. reforming of methanol with the aid of special catalysts.[11,12] Even though the purpose of the methanol reforming reaction is the production of hydrogen, there are another products formed that must be taken into consideration, e.g. CO₂, and CO. Reminding that the hydrogen production is for PEMFC application, it is clear that the formation of CO must be minimized. More specifically, its higher limit must be lower than 10 ppm, otherwise it poisons the anodic catalyst (Pt) of the low

temperature FCs.[11] This highlights the importance of the catalyst performance in the reaction. Ideally, the catalyst should be highly active in order to achieve large amounts of hydrogen, highly selective CO_2 so that the CO produced is negligible and finally it should present long-term stability. Cu/ZnO-based catalysts are of great importance for industrial scale catalytic production of reformat hydrogen.[13] Owing to their wide commercial relevance, Cu/ZnO-based catalysts, prepared via several preparation routes, are being extensively investigated; and substantial improvements in their efficiency of catalytic activity brought about by addition of suitable promoter/support, combination with effective component, and implementation of new preparation techniques have been reported.[14-19] Unfortunately, use of nanostructured Cu/ZnO-based hybrids as reforming catalysts is still lacking to date. This thesis in Chapter 5, 6, and 7 will focus on the rational design of different nanoarchitectures, i.e. Cu NP/ZnO nanorod nanocomposites, microwave-activated CuO nanotip/ZnO nanorod nanocomposites, and O_2 plasma-activated CuO-ZnO inverse opals, with integrating direct synthesis of catalyst and its immobilization for achieving high efficiency of microreformer applications. In each section the strategies proposed to enhance the performance of the nanostructured catalysts are described.

Current hydrogen generation in commercial use is mainly from hydrocarbon fuels by steam reforming, which strongly relies on fossil fuel and produces undesired CO_2

as a side product. Hydrogen has to be produced from renewable and carbon-free resources using nature energies such as sunlight if one thinks of clean energy and environmental issues. Therefore, achievement of solar-hydrogen production from water has been urged.[20] Motivated by the idea of photosynthesis, hydrogen generation from water splitting (artificial photosynthesis) has attracted a lot of attention.[21] In this regard, a photoelectrochemical (PEC) cell consisting of semiconductor photoelectrodes that can harvest light and use this energy directly for splitting water is a more promising and cost-effective way for hydrogen generation. Among the various candidates for the photoelectrode, metal oxides are relatively inexpensive and have a better photochemical stability. [22-25] The efficiency of PEC devices has been limited by several key factors, such as the limited light absorption efficiency in the desired visible region and the recombination of photoexcited electrons and holes. The recent development of nanostructures opens up new opportunities in addressing these fundamental scientific issues. The primary reason is their unique physical and chemical properties compared to bulk materials as well as their potential applications in various technologies including energy conversion.[26] However, to the best of our knowledge, there has been no study to date regarding such inverse-opal nanostructure applied into PEC water splitting. This thesis in Chapter 8 concentrates on the synergistic effect of optical amplification with surface hybridization on the enhanced PEC efficiency of ZnO

inverse opals modified by carbon in a non-sacrificial electrolyte. This development can potentially contribute to the application of PEC devices having good efficiency, visible-light harvesting, and long lifetimes. Finally, conclusions and future researches will be summarized.



Chapter 2

Literature Review

2.1 Direct methanol fuel cell

During operation, a direct methanol fuel cell (DMFC) oxidizes an aqueous methanol solution, forming CO₂ gas and protons. It then releases the CO₂ into the anode structure. The protons that are generated at the anode pass through the solid polymer electrolyte membrane where they simultaneously combine with electrons and the oxidant (air or oxygen), which is reduced to water finally. The overall cell reaction in a DMFC leads to the production of CO₂ and water, as shown in Figure 2.1. Normally, with high concentration of methanol it will provide higher power density. However, it also causes severe methanol crossover to the electrolyte membrane and results in mixed potential at the cathode. Therefore, it will present low cell performance. By this reaction mechanism, methanol molecules will diffuse through the membrane and directly oxidized by oxygen on the cathode.

According to the literature, the goal of a maximum cell voltage or power density should be reached through employing methanol feed concentrations slightly below 50% by volume.[28] In addition, it was found that the performance of an operating cathode is not severely affected by an increase of the methanol concentration in the

anode compartment. Potential-lowering methanol crossover is already present at low concentrations and an increase in methanol permeation preferably leads to fuel losses via direct chemical oxidation. Questions about fuel utilization and methanol oxidation product distribution under these conditions have to be dealt with in order to optimize the overall system performance.[28]

The main disadvantage of the DMFC system is the relative low power density. Although the DMFC system relies on thermodynamically favorable reactions, in practice, both of the electrodes (anode and cathode) are kinetically hindered due to the irreversible nature of the reactions. Therefore, both the anode and cathode suffer from similarly large overpotentials.[4] Methanol will be oxidized to CO_2 at the anode of a DMFC system, but the oxidation reaction proceeds through the formation of CO as an intermediate, which strongly adsorbs on the surface of a Pt catalyst. Therefore, a potential that is much more anodic than the thermodynamic value is needed to obtain a reasonable reaction rate.[27] In contrast to the PEMFC where it is mainly only the cathode that is kinetically hindered, both electrodes suffer from kinetic losses in the DMFC system.

In reality, the reactions are both highly activated, and hence poor electrode kinetics (kinetic losses) cause the electrode reactions to deviate from their ideal thermodynamic values in such a way as to bring about a serious penalty on the operational efficiency of the DMFC. In Figure 2.2, a breakdown of the various

limiting effects is presented, including kinetics, resistance, methanol crossover, and mass transport. In order to draw a current from the DMFC, a far more positive potential (overpotential) is required at the anode and a more negative potential (overpotential) at the cathode to accelerate the reactions to reasonable rate (i.e., to produce a cell current). These are shown in Figure 2.2 as the dark gray areas (kinetic losses), and their effect on the efficiency of the cell is interpreted as a reduction in the light gray area, which represents the observed voltage from the cell.[4]

As Figure 2.2 demonstrates, the anode and cathode overpotentials reduce the cell potential by approximately similar amounts. Together, they may be responsible for a loss of DMFC efficiency of approximately 50%. [29] A simple argument shows why the oxygen reduction reaction (ORR) is a highly activated process: each O_2 molecule requires the transfer of four electrons for complete reduction, and the simultaneous transfer of these electrons is highly unlikely. In fact, partial electron transfer takes place, leading to the formation of surface intermediates such as superoxide.

The application of a Pt electrocatalyst allows the stabilization of these intermediates and allows the reaction to proceed at a reasonable and useful rate. In addition, the catalyst may accelerate the reaction by opening up new reaction pathways. In the case of methanol electrooxidation at the DMFC anode, the picture is less clear. The electrooxidation of methanol only occurs at a reasonable rate in the presence of Pt or a Pt-based electrocatalyst. However, a great deal of discrepancy

exists among experimental data; this may be due to the wide range of experimental conditions used in the studies.[4]

2.1.1 Catalyst supported on carbon nanotube

Novel carbon materials such as carbon nanotubes (CNTs) have been investigated as DMFC catalyst supports and enhanced catalytic performance has been demonstrated. However, difficulties involved in the preparation of CNT-supported catalysts diminish practical applications. Other nanostructured carbon materials such as carbon fibers and carbon nanohorns provided only minor improvements in electrocatalytic activity. Thermal treatment is a four step procedure that is an essential component of catalyst preparation (Figure 2.3).[30] Structure and morphology of Pt/CNT composites synthesized by thermal treatment were characterized by transmission electron microscopy and X-ray diffraction. As shown in Figure 2.4, Pt nanoparticles were highly dispersed and adhered to CNTs, yielding a structure that is similar to a Pt-Ru/C nanocatalyst (Figure 2.5).[31] Fujigaya et al. proved that catalyst reconstruction and distribution could be achieved with the use of CNT as a support (Figure 2.6).[32] Additionally, catalyst agglomeration could be avoided with the addition of polybenzimidazole. Prabhuram et al. synthesized Pt-Ru nanoparticles on CNTs by a simple reduction method using sodium borohydride as the reducing agent and tetraoctyl ammonium bromide as a stabilizer.[33]

Chunmei et al. observed that the electrocatalytic performance of Pt-RuO₂/CNTs

was strongly dependent on the amount of RuO₂ in the catalyst.[5] A Pt-RuO₂/CNTs catalyst with 15% Pt and 9.5% RuO₂ exhibited superior electrocatalytic activity for methanol oxidation. A change in specific capacitance of RuO₂/CNTs, determined by the degree of proton conductivity and electron transfer, caused an increase in electrocatalytic activity of Pt-RuO₂/CNTs. An electrocatalyst based on capacitance may be useful in the design of novel catalysts for DMFC.

Hollow Pt-Co nanosphere electrocatalysts supported on CNTs were prepared at room temperature in a homogeneous solution, with Co metal nanoparticles as sacrificial templates.[5] Hollow Pt-Co/CNTs electrocatalysts displayed enhanced electrocatalytic activity for methanol oxidation compared to CNT-supported solid Pt-Co nanoparticles and commercial E-TEK PT/C (20 wt% Pt) catalysts. The incomplete and porous shell of Pt-Co hollow nanospheres provides an ideal surface structure with high surface area, exhibiting enhanced electrocatalytic activity. This approach was successfully extended to the fabrication of Au, Pd, and bimetallic hollow nanospheres.

2.2 Methanol reforming

Hydrocarbon fuels have very high hydrogen contents, e.g. methane (CH₄) has hydrogen content as high as 25 wt%.[34] They may be of use for automobile and portable FCs if hydrogen could be extracted from them. Among the hydrocarbons, four of the best candidates for hydrogen generation are methanol, ethanol, gasoline,

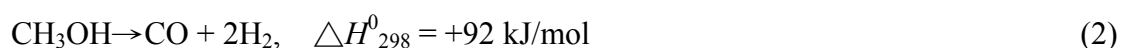
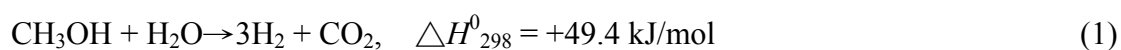
and diesel.[35] There are three ways to transform hydrocarbons into hydrogen, i.e. (i) direct decomposition, (ii) partial oxidation, and (iii) steam reforming.[11] The direct decomposition and partial oxidation of hydrocarbons require an elevated temperature and, at the same time, they produce a considerable amount of CO as a product or a byproduct (Table 2.1).[11] In a hydrogen FC, even a trace of CO can deteriorate the Pt electrode, e.g. on introducing 20 ppm CO into the polymer electrolyte membrane FC (PEMFC), the current density decreases to about 18% within 210h. In comparison with other impurities, the poisoning effect of CO is found to exert the largest impact on FC performance.

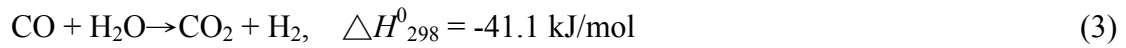
Steam reforming of hydrocarbons produces a lower CO content relative to the direct decomposition and partial oxidation of hydrocarbons, as listed in Table 2.1; hence, of the above three methods, steam reforming is a promising method to generate hydrogen for automobile and portable applications.[11] As the reforming of methanol requires a low temperature and produces one order of magnitude less CO than the other hydrocarbons (0.8% vs 10%-20%; see Table 2.1), it has attracted considerable attention in the past few decades in this research field.[35] In fact, the U.S. army is focusing on the development of the technology of reforming methanol to generate hydrogen for portable PEMFCs, which are used as energy source for robotics, sensors, auxiliary power, soldier systems, microclimatic devices, and other systems being proposed to meet the tactical requirements of the future

battlefield.[36]

In the following, the reforming of methanol is specifically introduced. Methanol is a single chemical compound (CH₃OH) and commercially is primarily formed from natural gas through a syngas route. It is a liquid under ambient conditions and has a low boiling point of 65°C, which allows for facile vaporization in roughly the same temperature range as that for water. For the typical range of operation in methanol reforming (45-60 wt% methanol), the freezing point of the fuel mixture ranges from -44 to -74°C, a distinct advantage for cold-weather development of methanol-fueled systems. However, the high toxicity of methanol may pose a problem for large-scale applications. Unlike gasoline or diesel, methanol does not cause vomiting when ingested. This means that any ingestion that is not deal with quickly will result in the formic-acid metabolism route internally.[35]

Methanol reacts with steam in the presence of Cu-based catalysts, e.g. Cu/ZnO/Al₂O₃, at temperatures higher than 150°C to form a hydrogen-rich gas.[13] The main products are H₂, CO₂, and CO. The formation of methane is thermodynamically favored, but Cu-based catalysts usually do not promote the formation of this byproduct. The methanol steam reforming process involves the following reactions:[11]





Equation (1) generates 12 wt% hydrogen, which is the algebraic summation of Eqs. (2) and (3). Equation (2) represents methanol decomposition. Equation (3) represents a water-gas shift (WGS) reaction, which is an important process to reduce CO content in the reformat gas. The steam reforming reaction is endothermic, and an external heat supply is required to maintain the reaction. Steam reforming of methanol over Cu-based catalysts was originally thought to have involved the above process, i.e. methanol decomposition, followed by WGS. However, in recent years, this is considerable evidence to suggest another pathway including a methyl formate intermediate.[35] At the same time, the mechanism for the formation of the CO byproduct is a controversial topic. Even so, it is generally observed that CO can be minimized by decreasing the contact time, increasing the steam to carbon ratio to facilitate the WGS reaction, and decreasing the temperature, which acts to suppress CO thermodynamically.[35] But the increase of the steam to carbon ratio requires more heating for vaporizing the additional water in the feed.[11]

As the CO tolerance of PEMFCs is about 10-20 ppm at the normal working temperature of 80°C in portable applications, further processing is needed to remove the small amount of CO (~0.8 vol%) from the reformat gas of methanol.[37] Nowadays, there are three most common approaches to reduce the CO content to ppm level, i.e. preferential CO oxidation, selective membrane separations, and

selective CO methanation.[35] Figure 2.7 displays a schematic representation of the integrated methanol steam reformer system, which shows the main steps and components of steam reforming of methanol to generate hydrogen for portable applications.[11,38]


Compared with DMFC, steam reforming of methanol does not have the methanol crossover and the high catalyst usage problems. Current DMFCs typically use a Pt alloy at a loading of 2-8 mg/cm² on the anode, which is much higher than 0.2-0.3 mg/cm² used for both the anode and cathode in PEMFCs.[35] The drawback of steam reforming of methanol is its thermal management, because the reactor works at temperature above 150°C and sometimes up to 300°C. For portable FCs, the device not only needs to be well insulated to eliminate hot surface but also the exhaust needs to be cooled sufficiently so that it does not burn anyone.[35] As external heat is required for steam reforming (Figure 2.7), recently an autothermal-reforming technology was developed, which is a combination of partial oxidation and steam reforming processes.[35] In this technology, methanol reacts with a mixture of steam and oxygen, and the partial oxidation and steam reforming are carried out simultaneously, where the exothermic oxidation supplies the energy for the endothermic reforming.

2.3 Photoelectrochemical water splitting

Photoelectrochemical (PEC) cells provides a powerful means for converting light

energy into chemical energy that can be stored in molecules, such as hydrogen, through electrochemical reactions, e.g. water splitting. The generation of hydrogen from PEC water splitting was first demonstrated in 1972 by Honda and Fujishima.[23] Besides electrolytes, the key components in a PEC cell are the electrodes (cathode and anode) on which redox chemical reactions involving electron transfer take place; at least one electrode should be a semiconductor (SC). Figure 2.8 shows a simple schematic of a typical PEC device. A conventional PEC cell is established with a SC photoanode and a Pt electrode as the cathode in the electrolyte solution. Under irradiation with the photon energy equal to or exceeding the band-gap energy of the SC photoanode, the electrons are excited and promoted from the valence band to the unoccupied conduction band. n-type SCs are preferred for the photoanode, and the depletion layer formed at the n-type SC-electrolyte interface will lead to energy-band bending as shown in Figure 2.9, which facilitates the separation of photogenerated electrons and holes. The electrons transport to the cathode and react with photons to generate hydrogen, while the holes accumulate on the surface of the photoanode and react with water molecules to produce oxygen. In the presence of sacrificial hole scavengers such as alcohols in the electrolyte solution, the photoexcited holes can oxidize these reducing reagents without producing oxygen. In this chapter, if not otherwise state, the photoanode serves as an oxygen evolution electrode, as shown in Figure 2.8.

To achieve efficient splitting of water, the SC photoanode should meet the following criteria: (i) photochemically stable with good corrosion resistance in aqueous solution; (ii) with a conduction band edge more negative than hydrogen evolution potential and a valence band edge more positive than the oxygen evolution potential; (iii) strong absorption in the solar spectrum region; (iv) high-quality material with low density of defects for efficient charge transfer and reduction of the electron-hole recombination; and (v) low cost.[41-43] Unfortunately, to date, there is no such material that can meet all the requirements simultaneously. Among the various candidates for the photoelectrode, SC metal oxides are relatively inexpensive and have a better photochemical stability. Many metal oxides have been extensively studied and considerable progress has been made in recent years.[26]



For a PEC cell, the conduction band of most metal oxide material is less negative than the hydrogen evolution potential; thus, a small external potential needs to be applied to facilitate the PEC reactions.

The SCs for PEC water splitting can be generally classified as metal oxide and conventional photovoltaic (PV) material. The SC photoelectrode can be n-type (Figure 2.10a), p-type (Figure 2.10b) or coupling of n-type and p-type (Figure 2.10c). This can be a single photosystem as in the n-type (TiO_2) or p-type (InP), but for the coupled n- & p-types involve two photosystems (n-GaAs/p-InP).[21,23] Several n-types can be layered together so their band gaps cover most part of the usable

solar spectrum or several p-types can also be done the same way (Figure 2.10d).

When involving more than one photosystem, it is important to match the currents generated by the different layers to obtain better efficiency and this is achieved by aligning complimentary band gaps and controlling the thickness or active area.[21]

In PEC water splitting, metal oxide and conventional PV material or their combination are used. The anode and cathode are usually physically separated, but can be combined into a monolithic structure either using a metal structure by depositing the anode on one side and cathode on the other and sealing the edges (Figure 2.10e) or stacking the anode on its own substrate with the cathode on its own substrate and providing an electrical connection between the two (Figure 2.10f).[21]

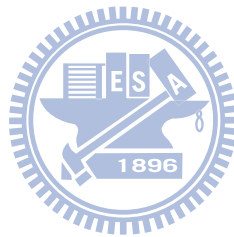
2.3.1 PEC hydrogen generation based on nanomaterial photoelectrodes

The use of nanomaterial-based PEC for water splitting dates back to 1997. Fitzmaurice and coworkers reported the studies of charge separation in a nanostructured TiO₂ membrane sensitized with Ru complexes.[44] The long-lived charge separation observed was an important finding that suggests that water splitting is practically feasible on nanostructured TiO₂ material. In the following few years, Khan and Akikusa reported the photoresponse of nanocrystalline n-TiO₂, n-TiO₂/Mn₂O₃, and n-Fe₂O₃ thin-film electrodes during water splitting reactions.[45,46] These results demonstrated that nanocrystalline metal oxide

photoanodes are stable for water splitting. Significantly, the nanocrystalline n-Fe₂O₃ films showed higher photoresponse compared to those prepared by compression of n-Fe₂O₃ powder or by thermal oxidation of metallic Fe sheets, indicating that high-quality nanostructured materials could improve the overall efficiency of the water splitting reaction. Since then, the PEC performance of different nanocrystalline metal oxide films has been studied.[26]

Besides 0D nanostructures, 1D nanostructures, such as nanotubes, nanowires, and nanorods, are expected to exhibit much improved transport properties than nanoparticles. The first demonstration of PEC water splitting using 1D nanostructure as photoelectrodes was reported by Lindquist and coworkers in 2000.[47,48] They reported the photoelectrochemistry of hematite nanorod arrays for the photoanode. It is generally accepted that recombination of electrons and holes, trapping of electrons by oxygen deficiency sites, and low mobility of the holes cause the low photoresponse for hematite films. In comparison to nanoparticles, nanorods improve the transportation of carriers and thus reduce the recombination losses at grain boundaries, as illustrated in Figure 2.11a. Moreover, the small diameter of the nanorods minimizes the distance for holes to diffuse to the SC/electrolyte interface, as shown in Figure 2.11b. Ideally, when the nanorod radius is smaller than the hole diffuse length of Fe₂O₃, the hole transportation limitation can be solved. Indeed, the nanorods proved to be able to generate high quantum yields without applied voltage,

well beyond the efficiencies reported for polycrystalline and nanocrystalline films of hematite. This work demonstrated that nanorod arrays could potentially address some of the fundamental PEC issues and increase the photon-to-current yield of hematite.



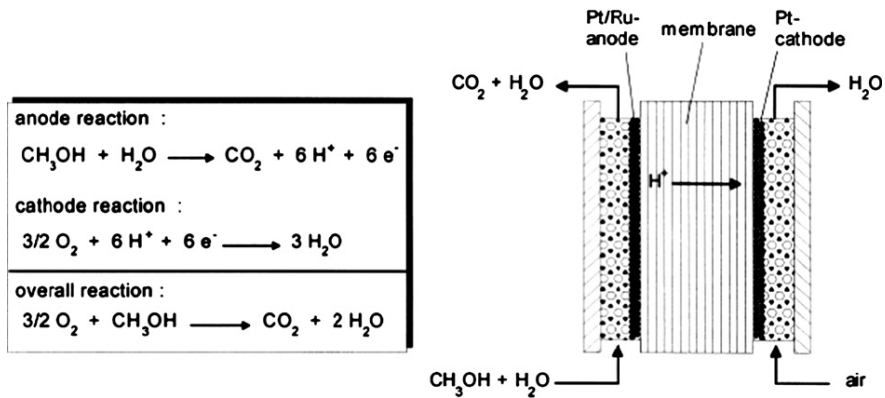


Figure 2.1 Schematic operating principles of DMFC.[27]

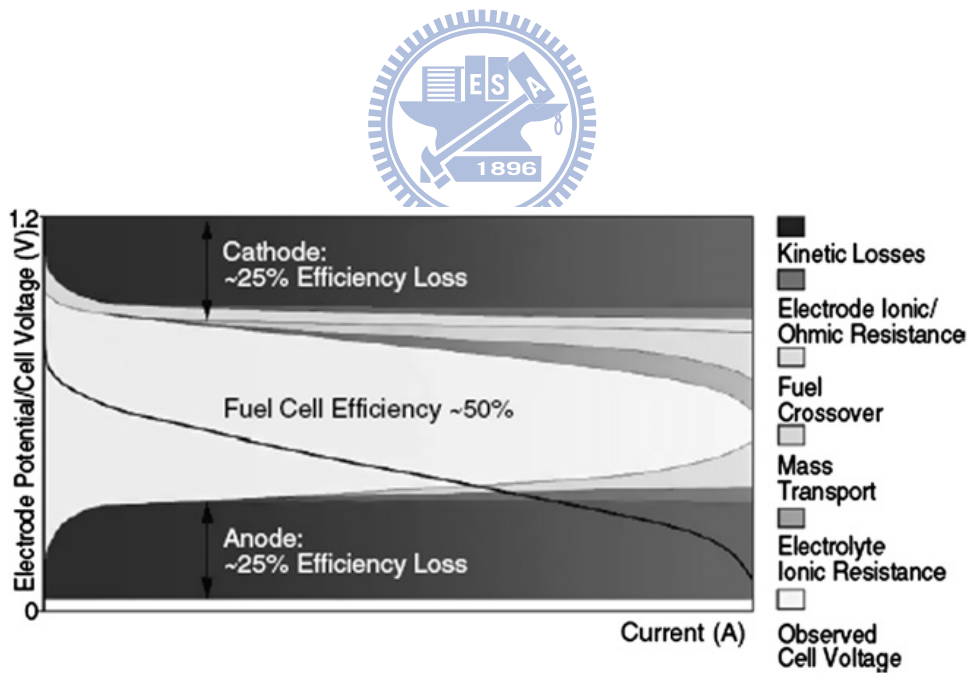


Figure 2.2 Breakdown of anode, cathode, and electrolyte-related performance

losses in a DMFC.[29]

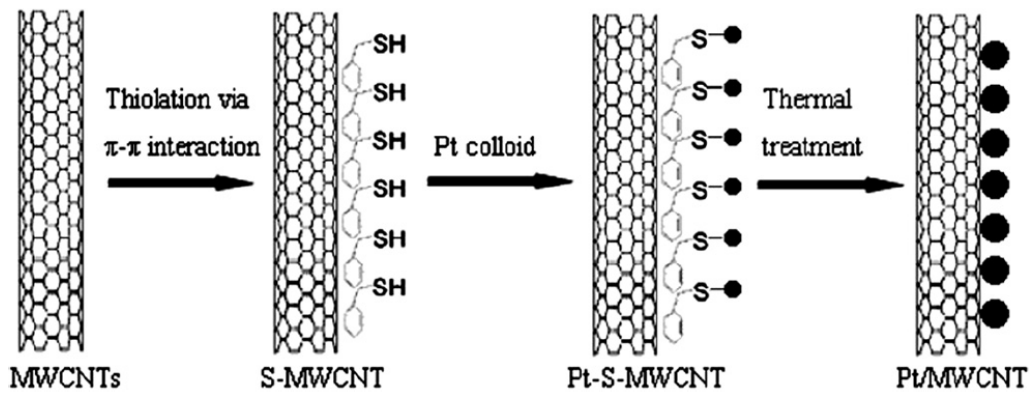


Figure 2.3 Schematic illustration of the synthesis procedure of the composite.[30]

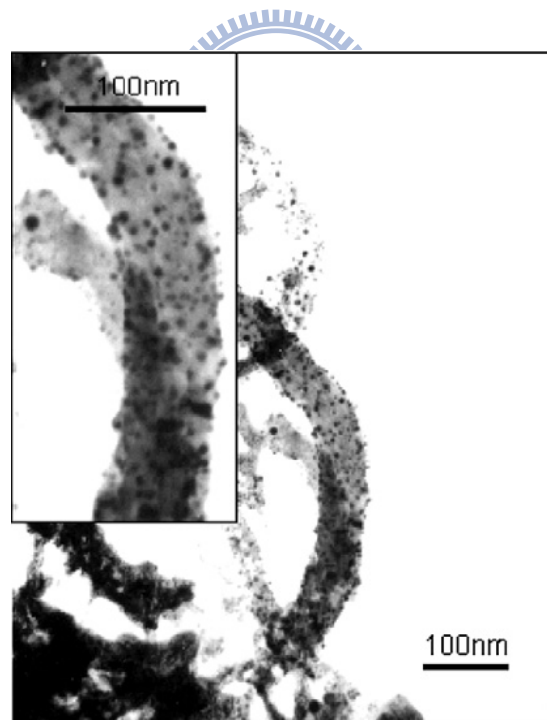


Figure 2.4 TEM images of Pt/CNT (inset: enlarged image).[30]

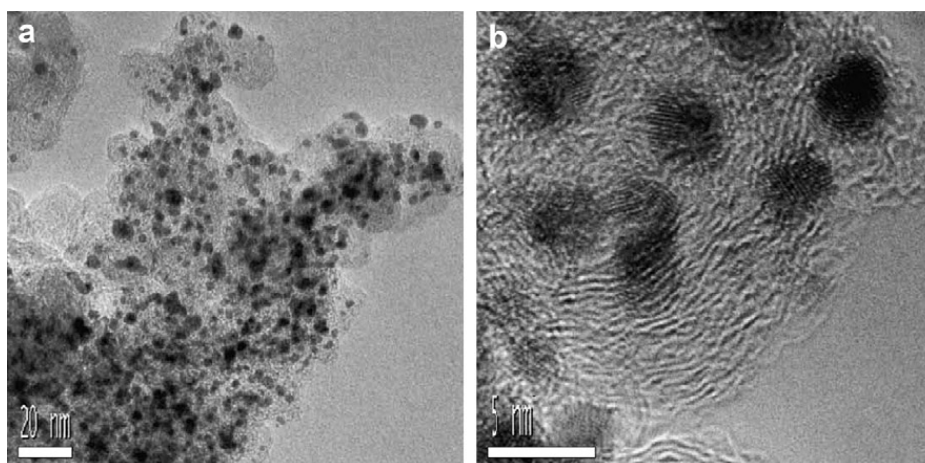


Figure 2.5 TEM images of 20 wt% PtRu/C nanocatalyst prepared with different molar ratios of Pt:Ru (a) LRTEM of 1:1, (b) HRTEM of 1:1.[31]

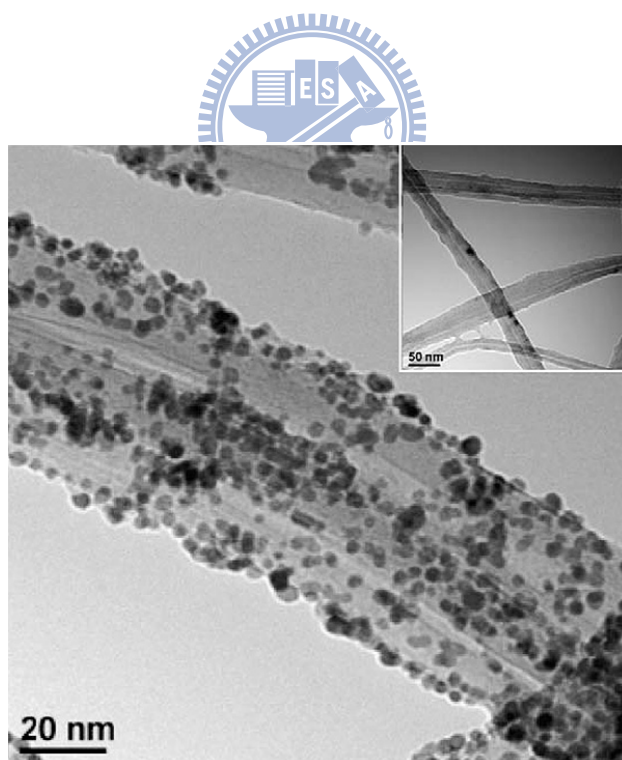


Figure 2.6 Typical TEM image of the CNT/PyPBI/Pt. Pt nanoparticles are loaded homogeneously on the PyPBI wrapped CNTs.[32]

Table 2.1 Reactor temperature ranges for initial processing of different fuels and

CO content of different process streams after the initial reaction.[11]

Reaction	Temperature range of initial processing (°C)	CO in the reaction product (vol%)
Steam reforming of		
Methane	700–800	11.2
Methanol	150–350	0.8
Ethanol	500–700	10–14
Muticarbon hydrocarbons	700–750	20.0
Partial oxidation of		
Methane	1200–1300	20.0
Muticarbon hydrocarbons	>250	25.0

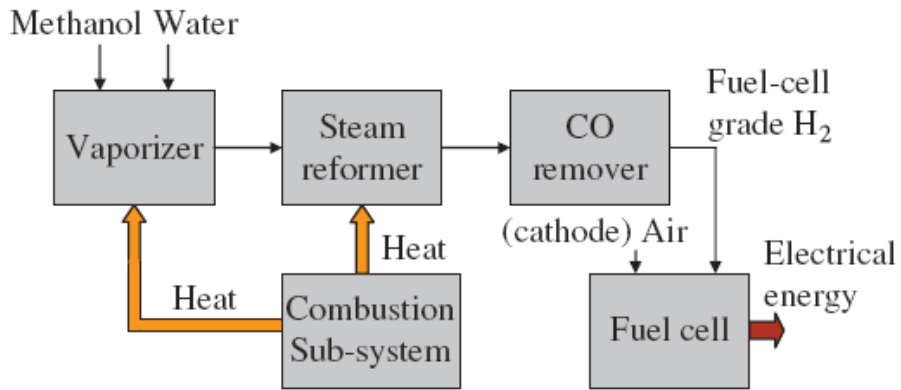
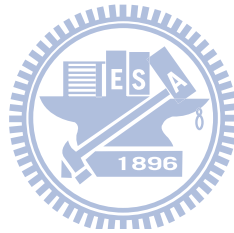


Figure 2.7 Schematic diagram of the integrated methanol steam reformer

system.[11,38]

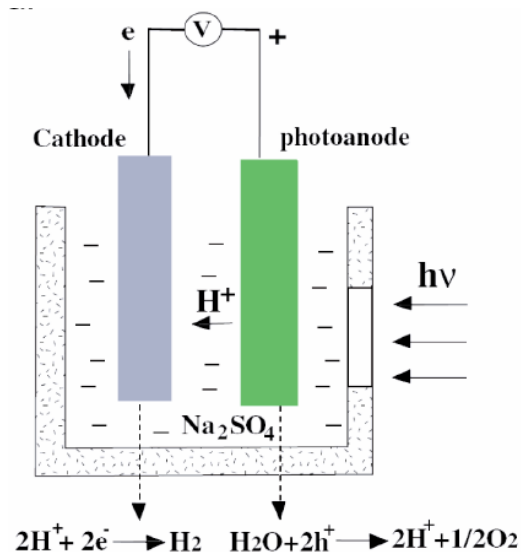


Figure 2.8 Schematic of a typical PEC device and its basic operation mechanism

for hydrogen generation from water splitting.[40]

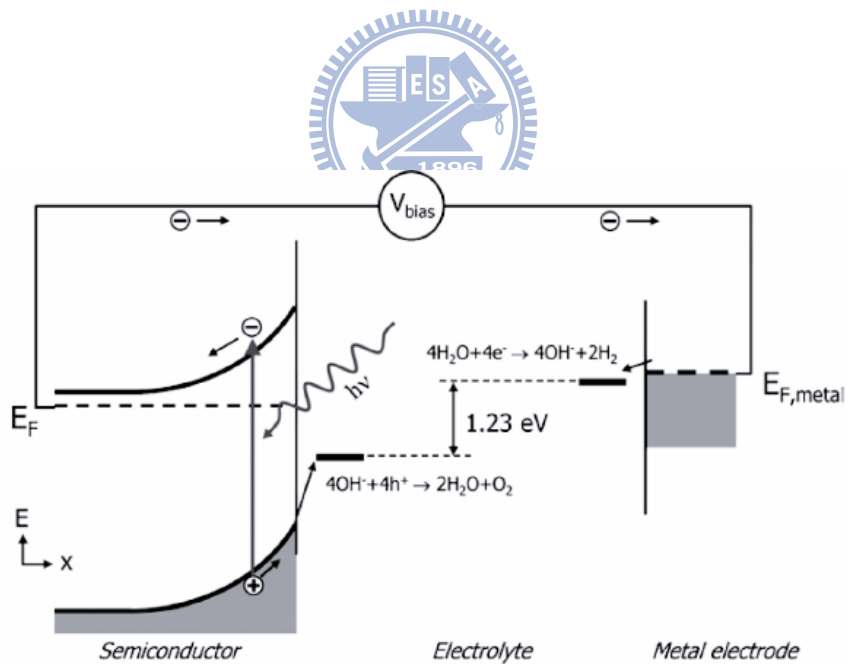


Figure 2.9 Energy diagram of a PEC cell consisting of an n-type SC photoanode

and a metal cathode for water splitting.[40]

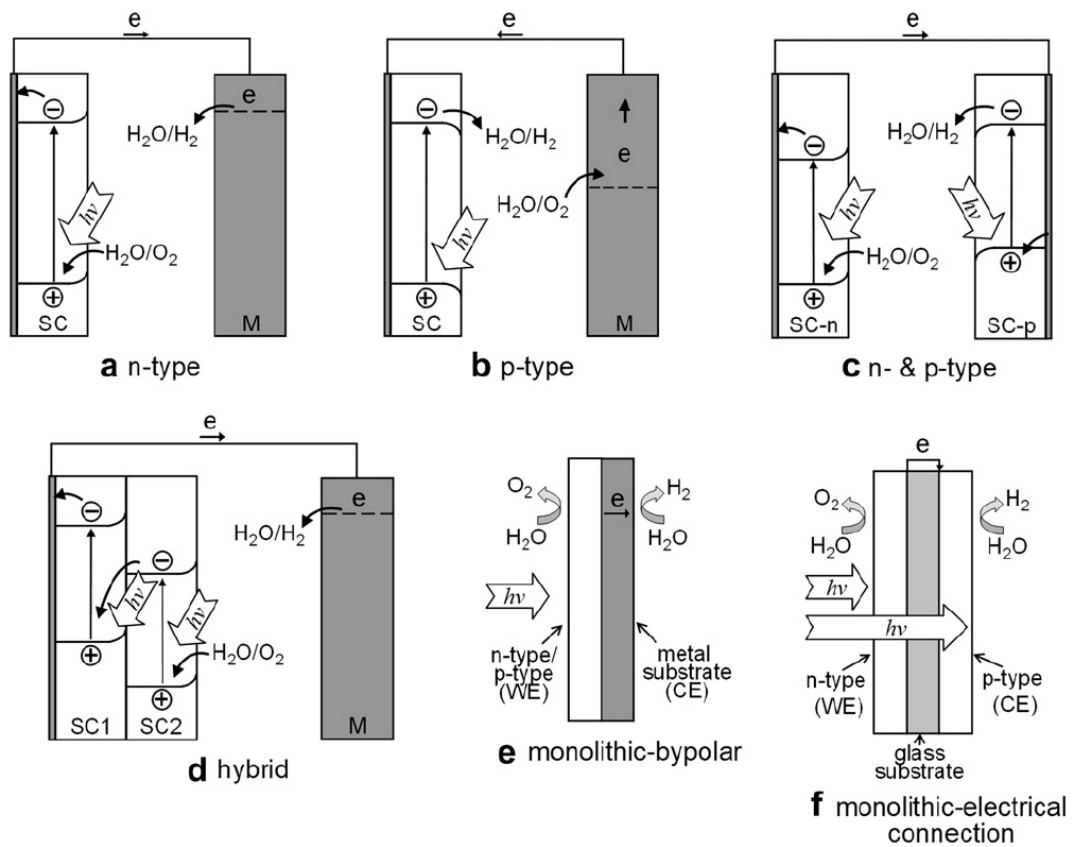


Figure 2.10 Type of photoelectrode for PEC water splitting (SC-semiconductor;

M-metal).[21]

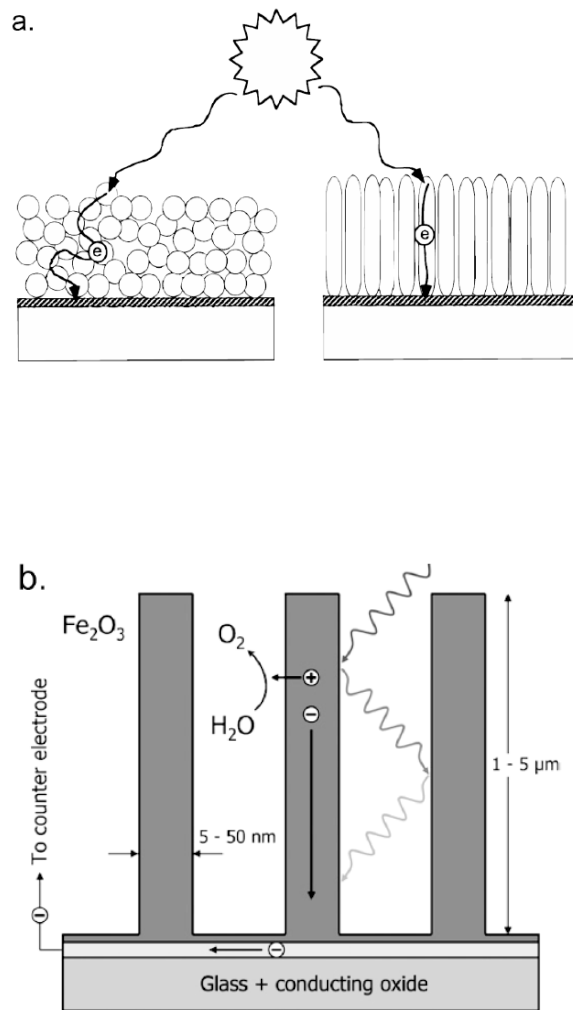
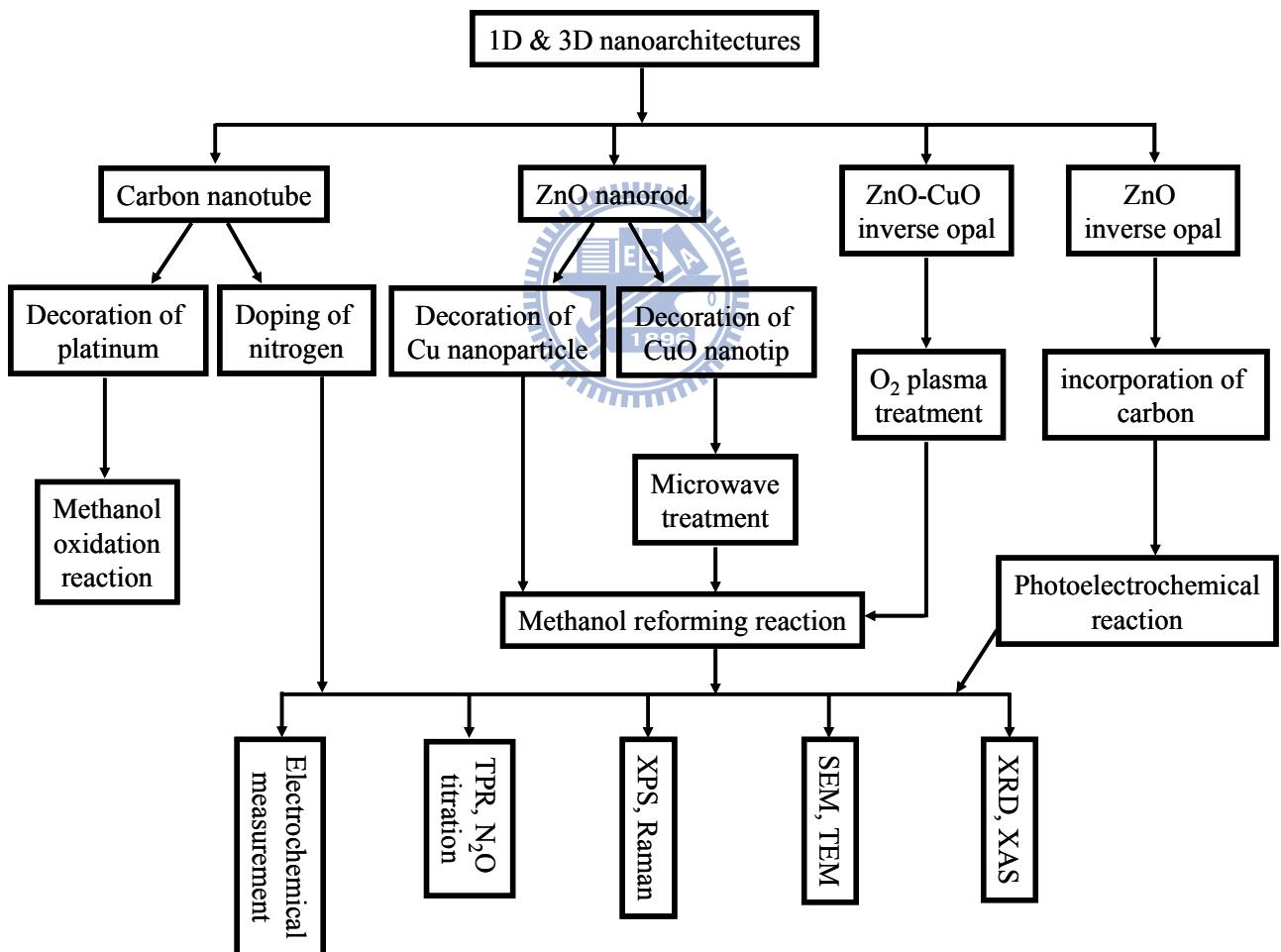


Figure 2.11 (a) Schematic representation of the electron transport through spherical particles and nanorods. (b) A schematic of a Fe₂O₃ photoanode for water splitting. The small diameter of the nanowires ensures a short hole diffusion length.[40,48]

Chapter 3

Experiment Methods

3.1 Flowchart of experiment process



3.2 Preparation of nanomaterials

3.2.1 Synthesis of CN_x NTs and Pt NPs deposition

For the synthesis of the CN_x NTs, an iron catalyst layer was deposited on Ti/Si substrates by ion beam sputtering prior to the NT growth step. Then CN_x NTs were grown on the precoated substrates by MPECVD method (Figure 3.1), which has been reported in our previous paper.[7] For Pt NPs deposition, a potential of -0.1 V vs Ag/AgCl in 0.5M H₂SO₄ & 0.0025M H₂PtCl₆ mixture solutions was performed for 15 sec as shown in Figure 3.2. Other details for the electrochemical deposition process are reported by Quinn and co-workers.[65]

3.2.2 Fabrication of ZnO NRs and metallic Cu NPs deposition

For ZnO array preparation, a thin film of ZnO was first deposited on the inner surface of microchannels prior to the NR growth step by solution method, which acted as a seed layer. This was followed by growth of aligned ZnO NRs on the precoated substrates by chemical bath deposition (CBD) method. The CBD growth was performed using equimolecular mixtures of zinc nitrate hexahydrate (99.5 %, Aldrich) and hexamethylenetetramine (99 %, Aldrich) as source precursors and a reaction temperature of 90 °C for 7 h (Figure 3.3). Other details of the NR array growth process were same as those described in the procedure proposed by Vayssieres.[84] A simplified attachment route, namely, direct impregnation method, was used in this study, which involved impregnation of the ZnO NR with Cu

precursor salts (copper nitrate trihydrate, 99.5 %, Aldrich) that were subsequently reduced (Figure 3.4). This reducing step is the boiling under reflux, which leads to Cu/Cu⁺ colloids. The synthesis of size-selected Cu NPs immobilized on ZnO NRs was carried out in ethylene glycol (EG; as reducing agent) solutions containing different amounts of sodium hydroxide (0.5 M NaOH in EG) with pH value between 9 and 11.[85] The decoration concentrations were controlled between 0.5 and 3 mM. The solutions were stirred for 30 min at room temperature, subsequently heated under reflux to 190 °C for 2 h, and then cooled in air. Dark brown solutions containing Cu NPs were formed in this manner, referred to as colloidal solutions in this work.



3.2.3 Synthesis of microwave-activated CuO NT/ZnO NR nanocomposites

For synthesis of ZnO nanorods inside the microchannels, chemical bath deposition growth was performed using the equimolecular mixtures of zinc nitrate hexahydrate (99.5 %, Aldrich) and hexamethylenetetramine (99 %, Aldrich) as source precursors, at a reaction temperature of 90 °C for 7 h. Other details for the NR array growth process were similar to the procedure proposed by Vayssieres.[84] Typically, the one-step direct impregnation method involved impregnation of ZnO nanorods/microchannel with Cu(NH₃)₄²⁺ complex cations aqueous solution as shown in Figure 3.5. The starting solution of copper (10 mM) was prepared by

mixing $\text{Cu}(\text{NO}_3)_2 \cdot 3\text{H}_2\text{O}$ (99.5 %, Aldrich) in deionized water (18.2 M Ω). $\text{Cu}(\text{NH}_3)_4^{2+}$ complex cations were prepared by adding a concentrated ammonia solution (28-30 wt %) dropwise into the above aqueous solution until the pH value reached 11 under vigorous stirring. The resulting homogeneous solutions were then gently heated in an oven at 90 °C for over 2 h. Finally, CuO nanotip/ZnO nanorod nanoarchitectures on the inner surface of microchannels were formed.

The as-derived CuO nanotip/ZnO nanorod catalyst precursors were processed in a microwave oven (2.45 GHz; TMO-17MA; TATUNG CO., Ltd.; Taiwan) for 10 min to obtain the final microwave-irradiated CuO nanotip/ZnO nanorod catalyst precursors. The microwave chamber was 452 mm in length, 262 mm in width, and 325 mm in height. During the microwave irradiation, the substrate temperature, environmental atmosphere and microwave power were maintained at room temperature, air and 600 W, respectively. For comparison, the as-derived CuO nanotip/ZnO nanorod catalyst precursors were also treated in a conventional annealing furnace at 450 °C for 1 h to obtain the conventional thermal-treated CuO nanotip/ZnO nanorod catalyst precursors

3.2.4 Preparation of O₂ plasma-activated CuO-ZnO inverse opals

For synthesis of CuO-ZnO inverse opals, 10 wt % of polystyrene (PS) colloidal suspension (Microparticles GmbH, 500 nm) was introduced into the microchannels. After room temperature evaporation of water from the suspension, PS opals with

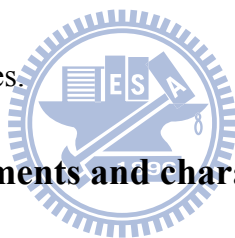
well-defined structures were formed inside the microchannels. These PS particle-packed microchannels were heated at 90 °C for 3-6 h in order to improve the connectivity between the neighboring particles. The copper-zinc precursor solution containing 0.5 M $\text{Cu}(\text{NO}_3)_2 \cdot 3\text{H}_2\text{O}$ (99.5%, Aldrich) and 0.5 M $\text{Zn}(\text{NO}_3)_2 \cdot 6\text{H}_2\text{O}$ (98%, Aldrich) in ethanol was then applied dropwise over the surface of the PS layer. These infiltrated samples were then placed in air at room temperature for 2-4 h. Finally, the resulting CuZnO/PS composites were heated in air to 300 °C to obtain the CuO-ZnO inverse opals (Figure 3.6).

These pristine CuO-ZnO inverse opals were then exposed to O_2 plasma for a short duration of 3-15 min to obtain O_2 -plasma treated CuO-ZnO inverse opals. The process of plasma-chemical surface modification was performed in a parallel-plate reactor with a DC flowing discharge (PCD-150; ALL REAL TECHNOLOGY CO., Ltd.; Taiwan). The distance between ground electrode and powered electrode was about 6 cm. The plasma chamber was 250 mm in diameter and 140 mm in height. The electrode was in the form of disk with around 6 inch in size. For the O_2 plasma treatment, the substrate temperature, total gas pressure and DC power were maintained at room temperature, 200 mTorr and 50 W, respectively.

3.2.5 Preparation of carbon-modified ZnO inverse opals

For synthesis of carbon-modified ZnO inverse opals, 10 wt % of PS colloidal suspension (Microparticles GmbH, 500 nm) was introduced on the ITO substrate.

After room temperature evaporation of water from the suspension, PS opals with well-defined structures were formed on the ITO substrate. These PS particle-packed templates were heated at 90 °C for 3-6 h in order to improve the connectivity between the neighboring particles. The zinc precursor solution containing 0.5 M $\text{Zn}(\text{NO}_3)_2 \cdot 6\text{H}_2\text{O}$ (98%, Aldrich) in ethanol was then applied dropwise over the surface of the PS layer. These infiltrated samples were then placed in air at room temperature for 2-4 h. Finally, the resulting ZnO/PS composites were heated in air to 300 °C to obtain the carbon-modified ZnO inverse opals. For comparison, the ZnO noninverse opals could be prepared by the same fabrication procedure only without using PS particle-packed templates.



3.3 Experimental measurements and characteristics analysis

For methanol reforming reaction, the Al-alloy (6061) chip of the microreactor was made by ourselves through a laser machining method. Ten microchannels per Al-alloy chip were separated by 800 μm fins. The width, depth and length of the microchannels were 500 μm , 200 μm and 4.3 cm, respectively. For the calculation of the catalyst weight for the steam reforming reactions, we measure the total weight by precision electronic balance (± 0.1 mg; Sartorius). After reduction of catalysts in a H_2/N_2 (5/95) at a flow rate of 50 mL min^{-1} at 200 °C for 1 hr, premixed water, oxygen and methanol with a $\text{H}_2\text{O}/\text{O}_2/\text{MeOH}$ molar ratio of 1/0.125/1 were fed into the preheater maintained at 200 °C by means of microfeeder. The feed and product

gas streams were analyzed online with a thermal-conductivity-detector gas chromatograph (TCD-GC; China Chromatography CO., LTD.) and CO detector (Gastech CO., Ltd.; GTF200).

For photoelectrochemical measurement, a water-splitting photoelectrode was used as the working electrode with surface area of 0.5-1 cm², a platinum plate as counter electrode, and Ag/AgCl as reference electrode. All PEC studies were operated in a 1M Na₂SO₄ (pH7.0) solution as supporting electrolyte medium by using Electrochemical Multichannel Solartron Analytical System. The water-splitting photoelectrode was illuminated with a xenon lamp equipped with filters to simulate the AM1.5 spectrum.



For material characterization, XRD analyses were performed on a Bruker D8 Advance diffractometer with Cu (40 kV, 40 mA) radiation. SEM measurements were made on a JEOL 6700 field-emission SEM. XPS spectra were obtained using a Microlab 350 system. For obtaining TEM images, the products on the substrate were scratched and dispersed on a carbon-coated Cu grid, and analyzed using a JEOL JEM-2100 TEM system. Micro-Raman analyses were performed on a Jobin Yvon Labram HR800 spectrometer. XAS analyses were performed on a beamline BL17C1 and BL20A1 at the National Synchrotron Radiation Research Center (NSRRC), Taiwan. TPR and N₂O titration were carried out with a Micromeritics AutoChem II 2920 instrument.

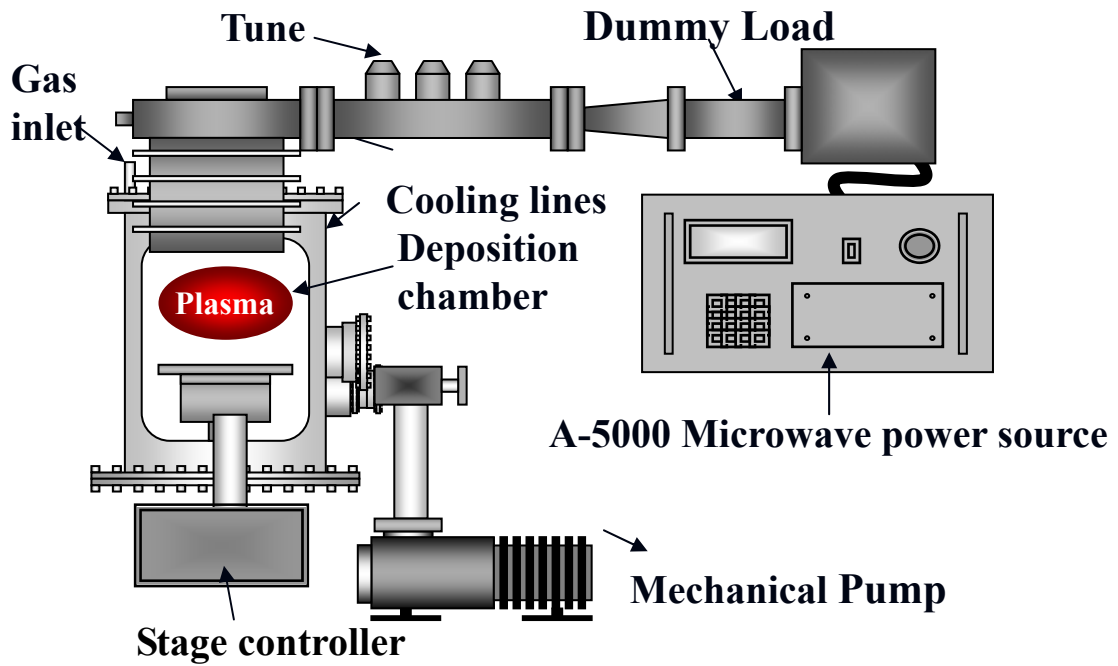


Figure 3.1 Schematic diagram of microwave-plasma enhanced chemical-vapor

deposition (MPECVD) facility.

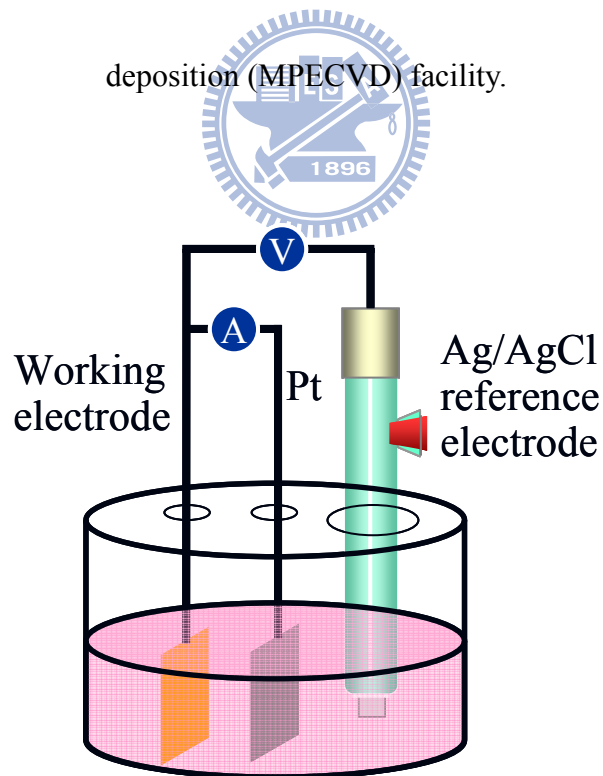


Figure 3.2 Schematic diagram of electrochemical deposition facility.

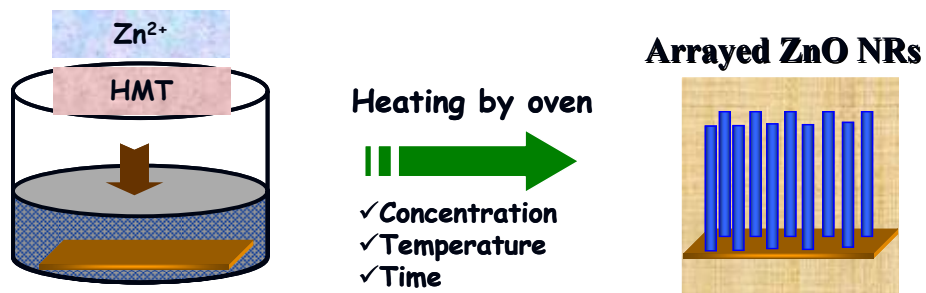


Figure 3.3 ZnO array preparation.

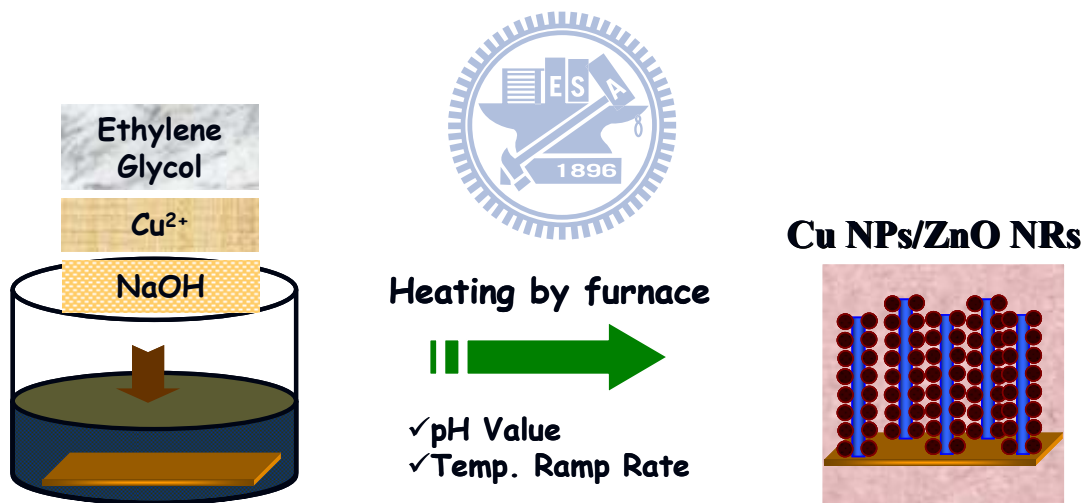


Figure 3.4 Cu NP/ZnO NR nanocomposites preparation.

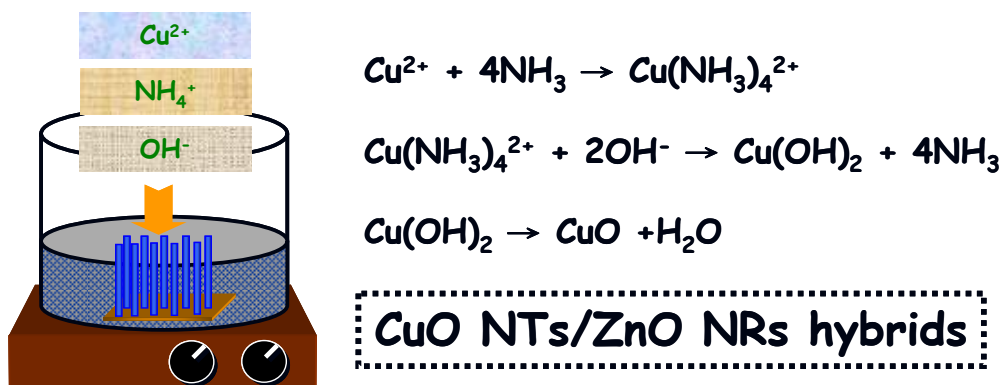


Figure 3.5 Cu NT/ZnO NR nanocomposites preparation.

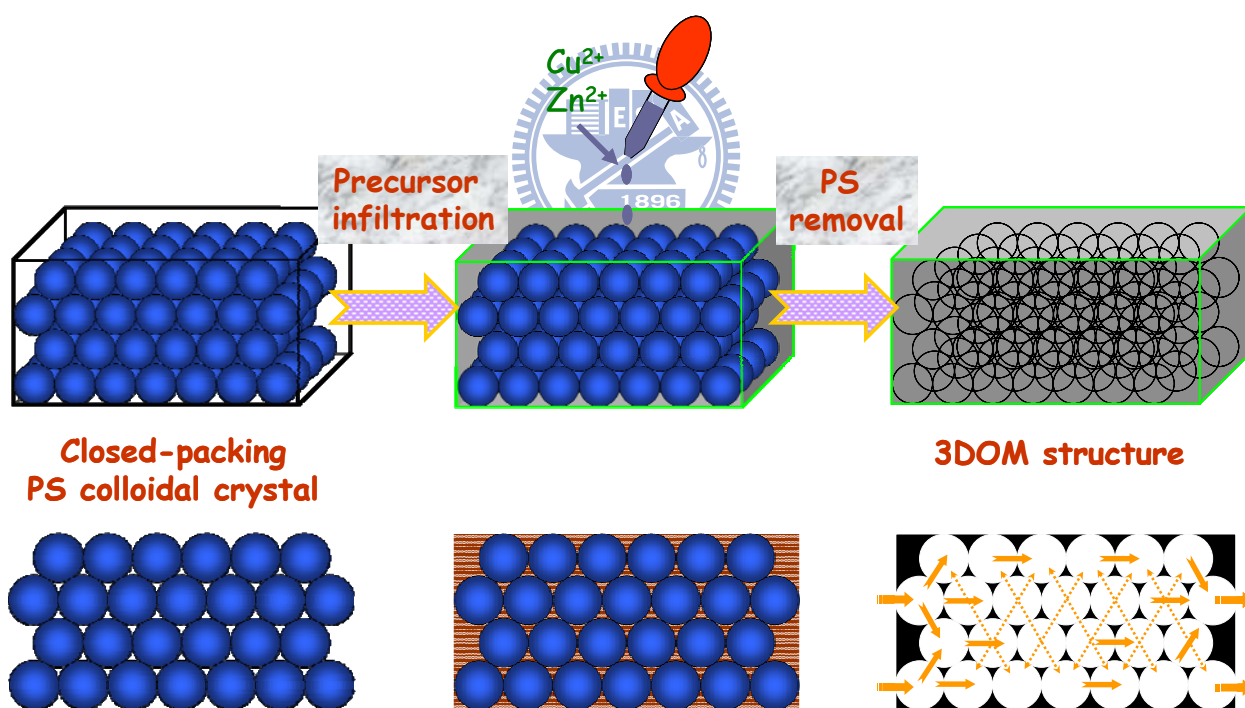


Figure 3.6 Procedure for the preparation of CuO-ZnO inverse opals using polystyrene colloidal crystal templates.

Chapter 4

Effects of Nitrogen-Doping on the Microstructure, Bonding and Electrochemical Activity of Carbon Nanotubes

4.1 Introduction

Carbon nanoscience and nanotechnology have been developed very rapidly over the past decade since the discovery of carbon nanotubes (CNTs). Miniaturization of electronic and electrochemical (EC) devices using the single-walled CNTs has been demonstrated.[49-51] Meanwhile, the remarkable structure of CNTs offers attractive scaffolds for further anchoring of nanoparticles (NPs) and biomolecules, which is highly desirable for energy conversion/storage and molecular sensing applications.[6,52-62] For these applications, surface modification of the CNTs or attaching functional groups on the sidewall become a key issue. In particular, surface modification offers an opportunity to improve the EC reactivity of CNTs through facilitating an efficient route for their electron-transfer (ET) kinetics with ambient species or specific biomolecules. Therefore, understanding the ET behavior between the CNT surface structures and the active entities are essential.

Several approaches such as acid-based wet-chemical oxidation, amidation, or esterification, diimide activation and solubilization of CNTs have been adopted to

effectively functionalize CNTs surface.[63,64] Despite that many solutions to modify CNTs are available, simple and reliable process to achieve such goal is still lacking. In the past we have introduced heteroatom dopant such as nitrogen (N) *in-situ* during the CNT growth and found it effective not only to change the atomic structure of the CNTs into bamboo like,[7] but also to improve their electrochemical (EC) performance down the road.[6] Although many reports on nitrogen doped carbon nanotubes (CN_x NTs) are available in the literature,[7-10] the role of N-doping in carbon nanotube and its resultant functionality is still not clearly understood.

In this paper, systematic studies on the effect of N incorporation in CNTs on the morphology, microstructures, electronic states, and electrochemical properties have been carried out. CN_x NTs with different nitrogen content have been produced using a simple *in-situ* nitrogen doping in a microwave plasma enhanced chemical vapor deposition (MPECVD) reactor.[7] Comparative studies to correlate the nitrogen content, microstructure, electronic structure, and EC performance of the CN_x NTs have been carried out. Subsequent loading of Pt NPs on the CN_x NTs to study the correlation of N doping with surface defect density and distribution has been carried out.

4.2 Microstructure and Bonding of Nitrogen-Doped Carbon Nanotubes

Figure 4.1 shows the cross-sectional scanning electron microscopy (SEM) images of the vertically aligned CNTs synthesized using different flow rate of N₂ gas but otherwise identical growth parameters. The diameters of the CNTs thus produced are in the range of 20-50 nm with an approximate length of 2-4 μm. Bamboo-like structure of the CN_x NTs is observed, as reported in our previous paper.[7] However, as the N₂ gas flow is higher than 80 sccm the average diameter of the CNTs goes beyond 100 nm with a reduced length of 1-2 μm. This may be attributed to the higher growth temperature at higher N₂ flow rate, which is deviated from the nominal growth condition.

The Raman spectra of the CN_x NTs prepared under different nitrogen flow rate are presented in Figure 4.2. The 1350 cm⁻¹ peak (D band) in Figure 4.2(a) corresponds to the disorder-induced feature due to the finite particle size effect or lattice distortion, while the 1580 cm⁻¹ peak (G band) corresponds to the in-plane stretching vibration mode E_{2g} of single crystal graphite.[66] A D' band around 1620 cm⁻¹ at the shoulder of the G band is attributed to the symmetry breaking due to the microscopic sp² crystallite size.[67] The D-band position and the ratio of the D- and G-band integrated intensities as a function of N₂ flow rate are depicted in Figure 4.2(b) and 4.2(c), respectively. As the N₂ flow rate increases from 0 to 40 sccm the position of the D band up-shifts slightly and eventually down-shifts over 40 sccm nominal N₂ flow rate. In contrast, the position of the G band does not show clear

dependence on the N₂ flow rate. Interestingly, the intensity ratio $I(D)/I(G)$ increases strongly as the N₂ flow rate is increased to 40 sccm and also decreases above the 40 sccm optimal flow rate. In principle, the $I(D)$ increases rapidly as a result of the enhanced defect density. Therefore, the up-shift of the D band and the increase in the ratio of the integrated intensities can be attributed to the increase of defect density in the graphitic structure and/or the enhancement of the edge plane by N-induced deformation in CN_x NTs. However, further increase of N₂ flow rate over 40 sccm leads to a higher growth temperature and results in enhanced graphitization degree. The growth temperature determined by pyroelectric thermal detector is 420, 450, and 750 °C at the N₂ flow rate of 0, 40, 160 sccm, respectively.

In order to obtain better understanding on the electronic structures of the CN_x NTs, X-ray photoemission spectroscopy (XPS) is applied to samples grown using different N₂ flow rates. Figure 4.3(a) shows the C 1s spectra of the CN_x NTs after background subtraction using Shirley's method.[68] The C 1s spectra thus obtained can be decomposed into three Gaussian peaks including C1 peak at 284.4±0.1 eV representing the delocalized sp²-hybridized carbon or graphite-like C-C bonding,[69] C2 peak at 285.1±0.1 eV reflecting defect-containing sp²-hybridized carbon associated with the trigonal phase with a sp² bonding,[69,70] and the C3 peak at 290.5±0.5 eV originating from the CO-type bonding generated by the oxygen contamination of the CNTs exposed to the ambient air.[69,71] Detailed study of the

peak position shows a slight up-shift from 0 to 40 sccm optimal N₂ flow rate followed by a down-shift at higher flow rate. This result is in agreement with the variation in the degree of structural disorder, which is associated with the electron density of the defect-containing sp²-hybridized carbon and reflected in the FWHM of the C2 peak as illustrated in the inset of Figure 4.3(a). The C2 FWHM reaches a maximum value at 40 sccm manifesting that the most pronounced disruption in the sp² carbon framework due to the incorporation of N atoms into the graphene lattice occurs at a N₂ flow rate of 40 sccm.

Likewise, the N 1s XPS spectra of the CN_x NTs with increasing N₂ flow rate are fitted by two Gaussian lines as shown in Figure 4.3(b). The peaks at 398.1±0.2 eV (denoted by *I_P*) and 400.8±0.2 eV (*I_G*) are assigned to tetrahedral nitrogen bonded to a sp³-hybridized carbon (so-called substitutional pyridine-like dopant structure) and trigonal nitrogen bonded to a sp²-coordinated carbon (so-called substitutional graphite-like dopant structure), respectively.[69] Figure 4.3(c) displays the fraction of pyridine-like and graphite-like defects as a function of the N₂ flow rate. Increasing N₂ flow rate is shown to give rise to an increase of the peak intensity ratios of the N-sp³ C bonding (*I_P*), which is strongly related to graphene sheets. However, increasing N₂ flow rate, keeping the rest of the process parameters the same, also led to an increase in the reaction temperature. As a result, it is suggested the graphene sheets are easily buckled, facilitating the cross linking between the

graphene planes through the sp^3 -coordinated carbons. Meanwhile, the peak intensity ratios of the N- sp^2 C bonding decreases slightly over 40 sccm nominal N_2 flow rate. In general, N-doping is shown to lower the energy of pentagon defects in the graphite-like dopant structures. Thus, through the N- sp^2 C bonding, N atoms are easily incorporated in the graphene sheets. The total N-doping levels for the peak ratio of $N/(N + C)$ are plotted against the respective N_2 flow rate in Figure 4.3(d). The CN_x NTs with N_2 flow rate of 40 sccm contain maximum N atomic ratio.

4.3 Nitrogen-Doping Effect on Electrochemical Activity

The ET behavior of CN_x NTs are explored using a potassium ferrocyanide redox probe (5 mM $K_4Fe(CN)_6$ in 1M KCl). A typical CV curve of CN_x NTs microelectrode in this redox couple system is shown in Figure 4.4(a). The well-defined peaks obtained in the forward and reverse scans are due to the Fe^{3+}/Fe^{2+} redox couple. The reversible redox reaction of the CN_x NT microelectrodes is further evidenced by the linear I_{pa} and I_{pc} vs $v^{1/2}$ plots shown in Figure 4.4(b), where I_{pa} , I_{pc} and v are the corresponding peak current densities of the cathodic and anodic reactions and the scan rate, respectively. These data indicate that the whole reactions are limited by semi-infinite linear diffusion of the reactants to the electrode surface. Moreover, the effective surface area of CN_x NT arrays can be evaluated from the slope of I_p vs $v^{1/2}$ based on Randles-Sevcik equation in the reversible redox system. The roughness factor, which is the ratio of the effective

CN_x NTs surface to the geometrical electrode surface area, as a function of N₂ flow rate is depicted in the inset of Figure 4.4(b). It is noted that the roughness factor of CN_x NT microelectrode prepared with N₂ flow rate of 40 sccm is ~33, showing significant enhancement in the effective surface area. Clearly, the N-doping induced electrochemically active sites on the surface of CN_x NT microelectrodes prepared with N₂ flow rate of 40 sccm are optimized.

The peak-to-peak separation (ΔE_p) of potassium ferrocyanide redox probe is strongly dependent on the ET rate, namely, the reactivity of electrode materials to the electrolyte. In Figure 4.4(c), ΔE_p of CN_x NTs with N₂ flow rate of 40 sccm is around 59 mV, reflecting excellent ET reactions. This is also related to the reduced internal resistance of the CN_x NT structures, which was determined by EC impedance (EIS) in 1M KCl solution containing 5 mM K₄Fe(CN)₆ at an AC frequency varying from 0.1 to 100 kHz as shown in Figure 4.5. From the point intersecting with the real axis in the range of high frequency, the internal resistance of the electrode is obtained. As shown in the inset of Figure 4.5, the arrayed CN_x NTs microelectrode prepared with N₂ flow rate of 40 sccm shows the lowest resistance of all, which is in good agreement with the above mentioned measurements. Moreover, the Nyquist complex plane plot of the CN_x NT microelectrodes exhibits nearly straight line, which is characteristic of a diffusion-limiting step in the EC process, indicating that CN_x NTs possess better ET

capability with selective N dopant.

The enhanced ET kinetics observed at CN_x NTs surface may in part be attributed to higher electronegativity of the CN_x NTs surface. The attractive interaction between the C-N dipoles present at the surface may attract the negatively charged members of the Fe(CN)₆^{3-/4-} and accelerates the redox reactions. In fact, the rate constant for ET from the reactant to the electrode can be expressed as

$$k_{ox} = \int d\epsilon (1 - f(\epsilon, T)) w_{ox}(\epsilon),$$

where w_{ox} is the rate of ET from an occupied level of the reactant to an empty level of the electrode.[72] This ET rates are given in terms of the density of available states, the electron-resonance width and the strength of the coupling to the phonon bath.[73,74] The activation energy for the reaction decreases with increasing electronic interaction width. The structure of the NTs, as well as their local density of states, might be responsible for the increase of the electronic-energy interaction width. In our case, arrayed CN_x NT microelectrode prepared with N₂ flow rate of 40 sccm has higher local-density of states (including surface defects induced states from XPS results), and promotes the enhanced ET kinetics.

The unique structures thus created in the *in-situ* N doping process can be verified by selective EC deposition technique, which is a direct and quantitative measure of the surface defects on individual CNTs. In this technique, a sequence of EC potentials were applied to the electrode, resulting in selective nucleation and

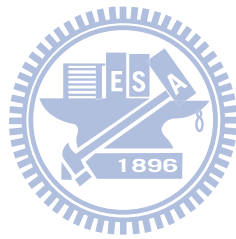
deposition of metal at the chemical reactive sites such as the defect sites on CN_x NTs. Figure 6 shows the comparative TEM images of the CN_x NTs prepared with various N₂ flow rate during growth and followed by 0.5M H₂SO₄ & 0.0025M H₂PtCl₆ mixture solutions. In Figure 4.6(a) most of the Pt particles aggregate on the top of the electrode to form large agglomerates, indicating lack of nucleation sites on the side surface of CN_x NT prepared with no N₂ flow during growth. Figure 4.6(b) shows more uniform and higher density of Pt NPs nucleating on the side surface of CN_xNTs prepared with 40 sccm N₂ flow rate during growth. However, excessive N₂ flow rate may cause adverse effect. Figure 4.6(c) shows Pt agglomerates of tens of nanometers scattered throughout the CN_x NTs, which can be attributed to low nucleation density at this growth condition (120 sccm N₂ flow rate). Figure 4.6(b) shows clear indication of the nearly monodisperse Pt NPs of 2-5 nm on the side surface of CN_x NTs having optimal defect density created under the 40 sccm N₂ flow rate during growth. Furthermore, a typical CV curve measured in 1 M CH₃OH/1 M H₂SO₄ solution for the arrayed Pt NP-CN_x NTs hybrid nanocomposites was shown in Figure 4.7. Remarkably, a significantly enhanced electrocatalytic activity is yielded for 40 sccm nominal N₂ flow rate mainly due to keep higher accessible surface area of discrete Pt NPs finely dispersed on CN_x NT. In sharp contrast, the arrayed Pt NPs supported by CN_x NTs without N₂ and with N₂ flow rate of 120 sccm display relatively low electrocatalytic activities. As described above,

the pretty good electrocatalytic activity can be obtained from Pt NP/CN_x NT nanocomposites with the N₂ flow rate of 40 sccm dopant, indicating that this arrayed cable-like nanocomposites can be the most promising candidate for useful catalytic applications in the μ FCDs.

4.4 Summary

Vertically aligned CN_x NTs have been synthesized using microwave plasma enhanced chemical vapor deposition with different nitrogen flow rate. The microstructure, bonding and electrochemistry properties have been investigated utilizing Raman, XPS, CV and AC impedance measurements to establish correlations among the N content, electronic structure, microstructure and EC activities. The results show that nitrogen incorporation provides a simple pathway to engineering/modifying the microstructure and electronic bonding structure, which is crucial to the ET kinetics of the CN_x NT electrode. *In-situ* N doping of the CNTs at an optimal 3.5 at. % N is effective in converting the nanotubes into bamboo-type morphology and promoting substitutional graphite-like defect structure, which is favorable for fast ET in electrochemistry. The surface defects thus created further enhance anchoring of Pt atom in the subsequent selective EC deposition to produce ultrahigh density Pt NPs to form nanocomposite, which is ideal for many applications such as fuel cell electrocatalyst. Therefore, the *in-situ* N doping of CNTs provides a simple and effective technique to produce CN_x NTs, which are

highly desirable in many EC based applications.



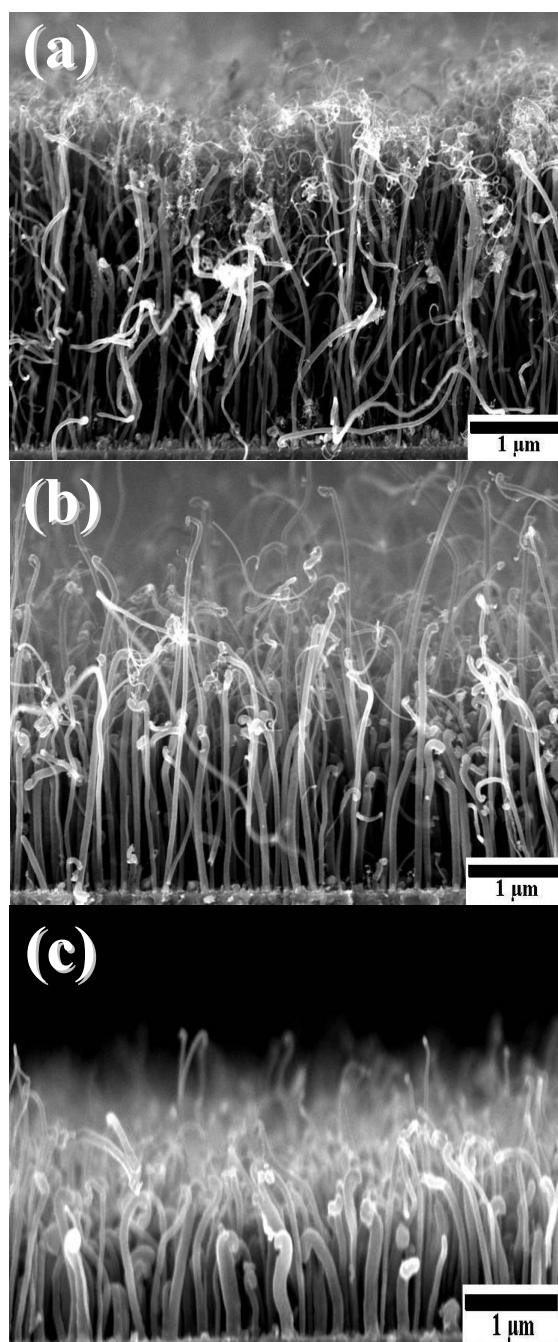


Figure 4.1 Cross-sectional SEM images of the vertically aligned CNTs synthesized at different flow rate of N_2 : (a) 0, (b) 80, and (c) 120 sccm.

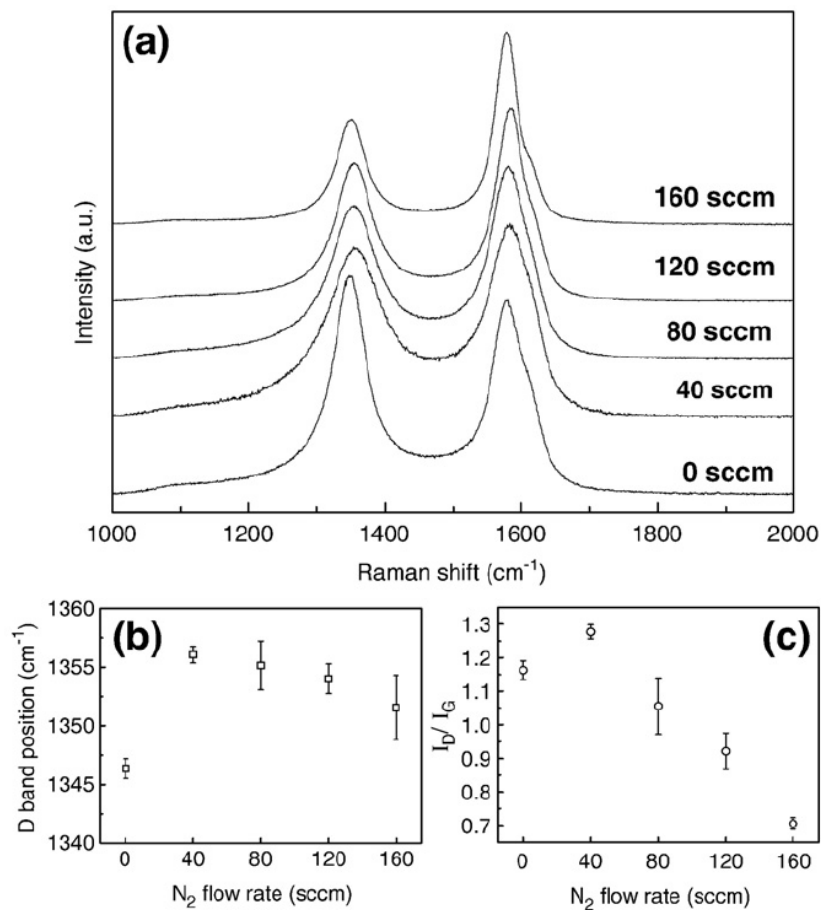


Figure 4.2 (a) Comparison of the peak intensities and the full width at half maximum (FWHM) of the first-order Raman spectra for the vertically aligned CN_x NTs prepared with different N₂ flow rate during growth. (b) D-band position as a function of N₂ flow rate. (c) I_D/I_G as a function of N₂ flow rate.

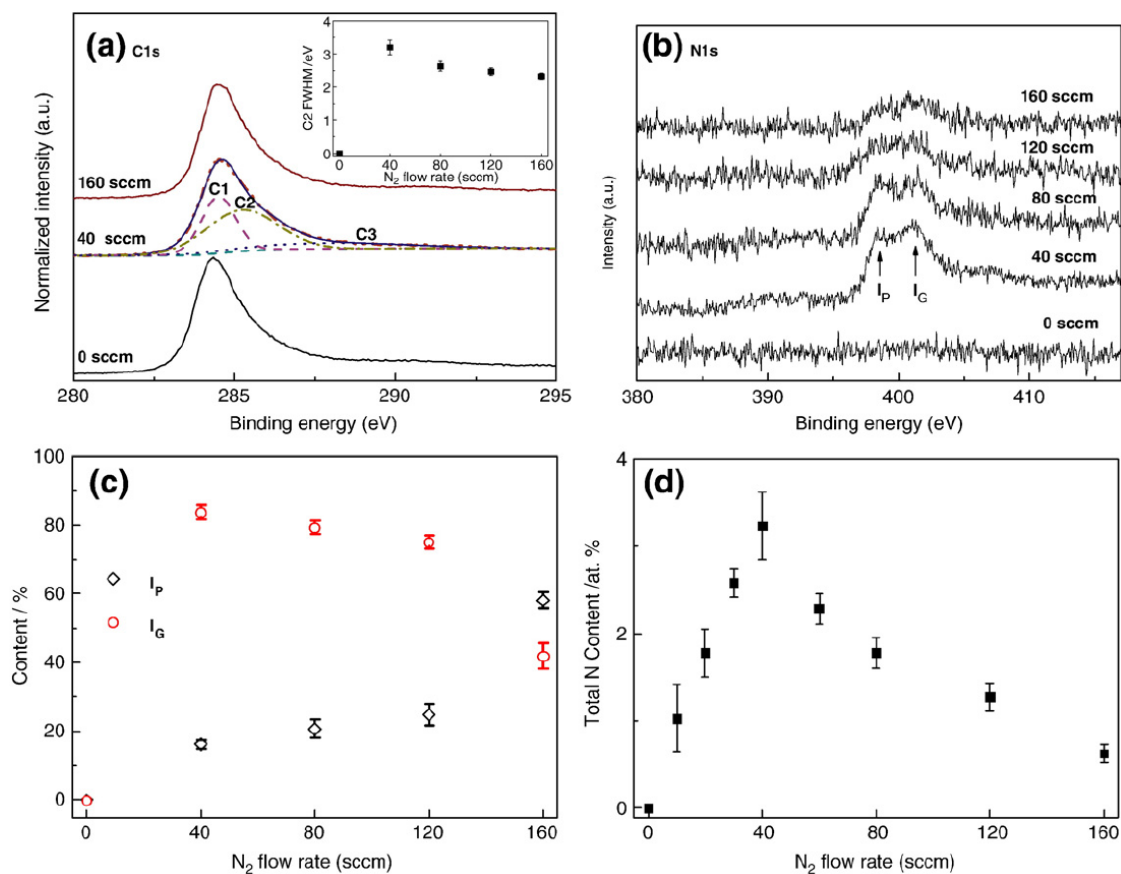


Figure 4.3 (a) The C1s XPS spectra of the vertically aligned CNTs prepared with various N₂ flow rate during growth. The inset is the FWHM of the C-N bonding component as a function of N₂ flow rate. (b) The N1s XPS spectra of the vertically aligned CNTs prepared with different N₂ flow rate. (c) The *I_P* and *I_G* as a function of the N₂ flow rate for the N1s peak. (d) The N-doping concentration as a function of the N₂ flow rate.

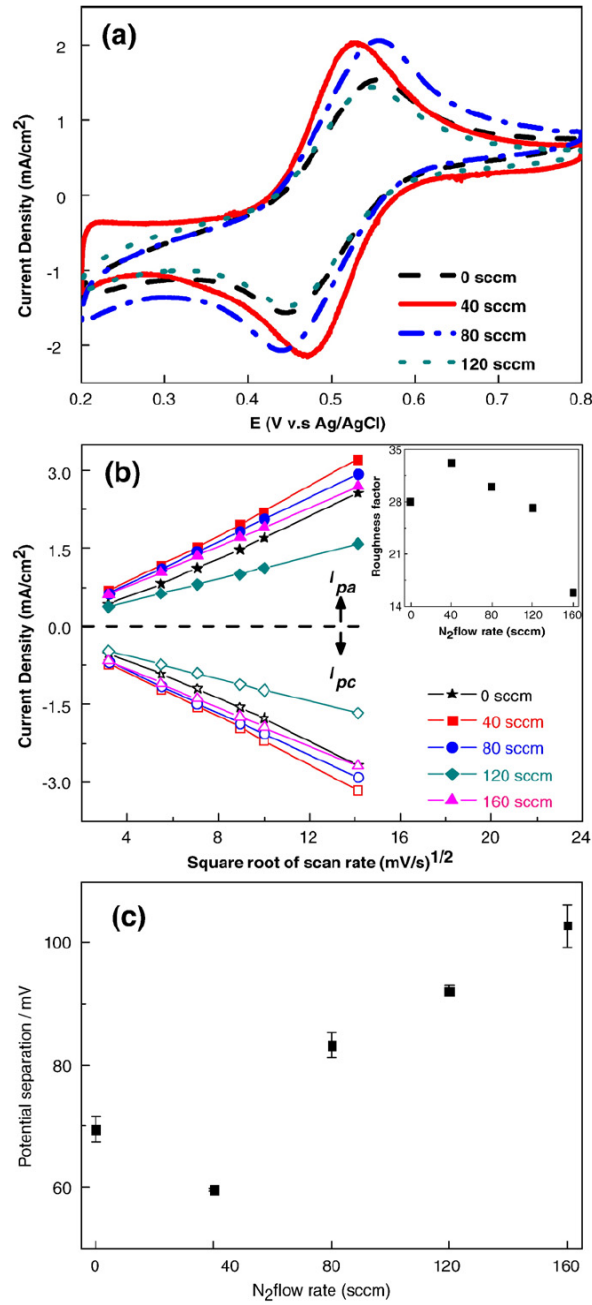


Figure 4.4 (a) Cyclic voltammetry of the vertically well-aligned CNTs modified with different N-doping level in 1 M KCl and 5 mM K₄Fe(CN)₆. (b) The ferricyanide peak current versus the scan rate (v)^{1/2} plot for CNTs using various flow rate of N₂ for both anode and cathode. (★: 0 sccm, ■: 40 sccm, ●: 80 sccm, ◆: 120 sccm, ▲: 160 sccm) The inset shows the roughness factor as a function of the N₂ flow rate. (c) The potential separation as a function of the N₂ flow rate.

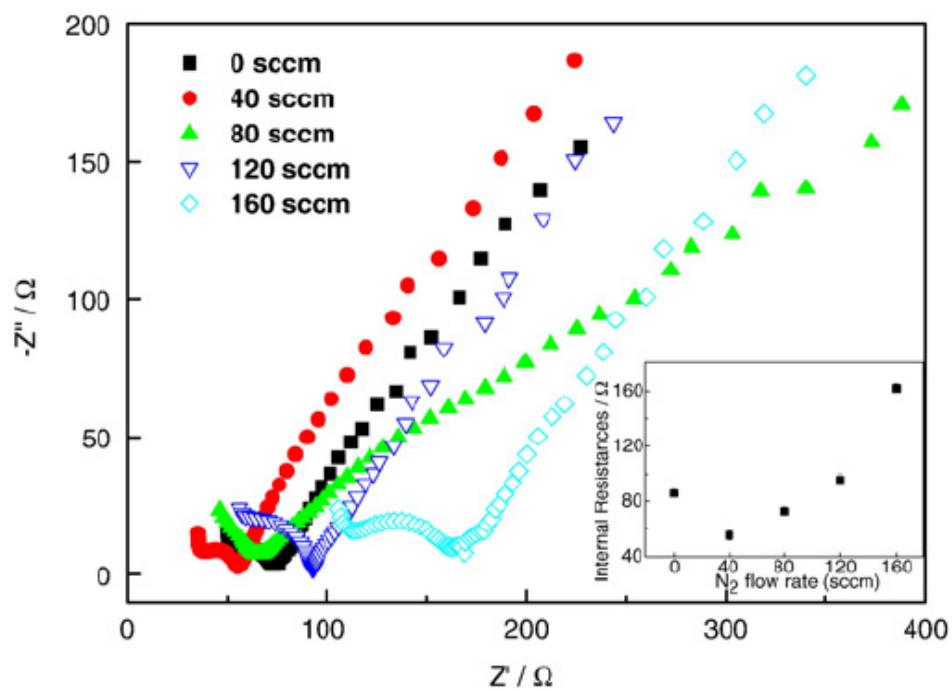


Figure 4.5 AC impedance analysis of the vertically aligned CNTs with different N-doping level in 1 M KCl and 5 mM K₄Fe(CN)₆. The inset shows the internal resistance as a function of the N₂ flow rate.

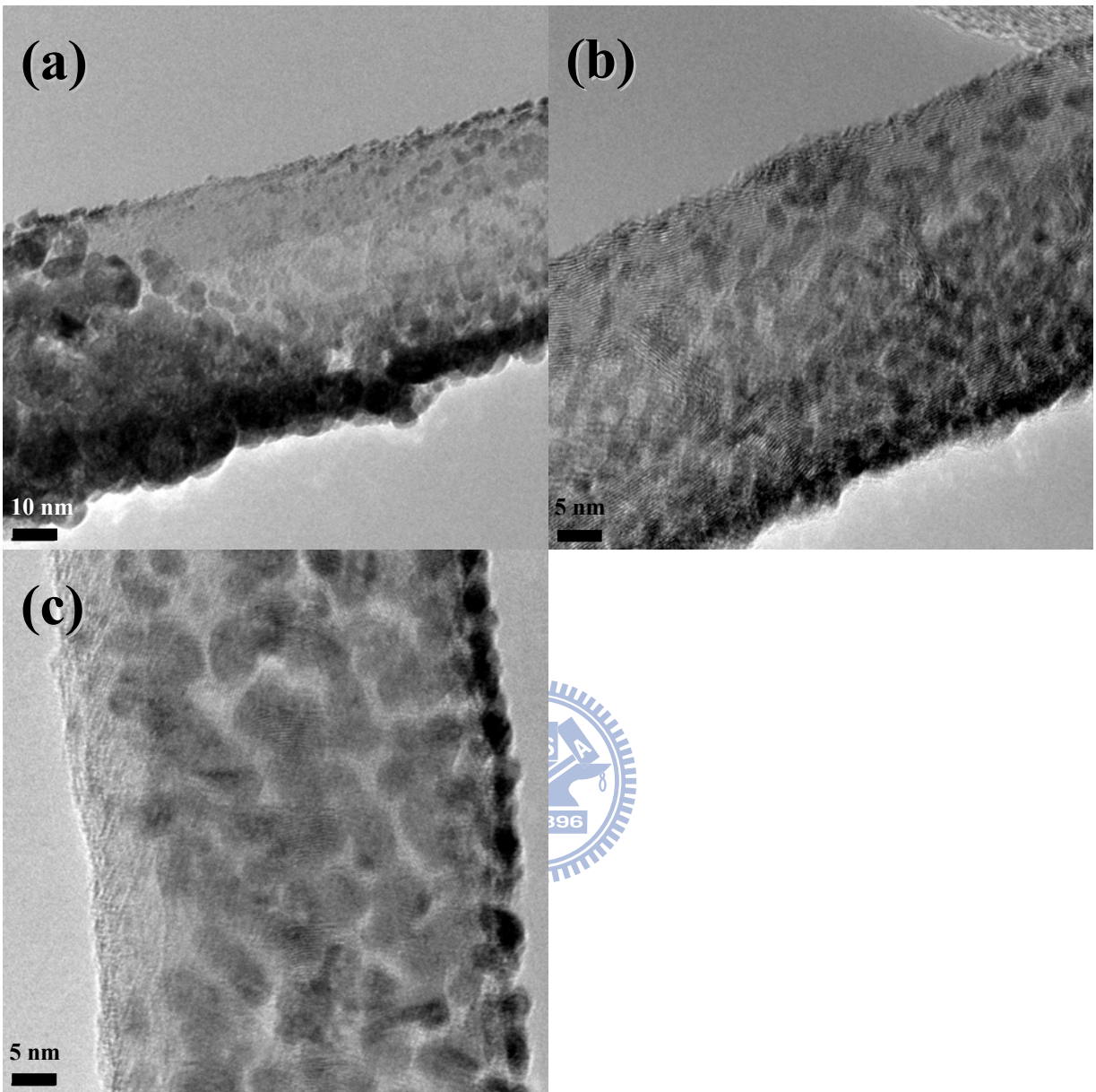


Figure 4.6 TEM images of the Pt NP-CN_x NT hybrid nanostructures synthesized at different flow rate of N₂: a) 0, b) 40, and c) 120 sccm.

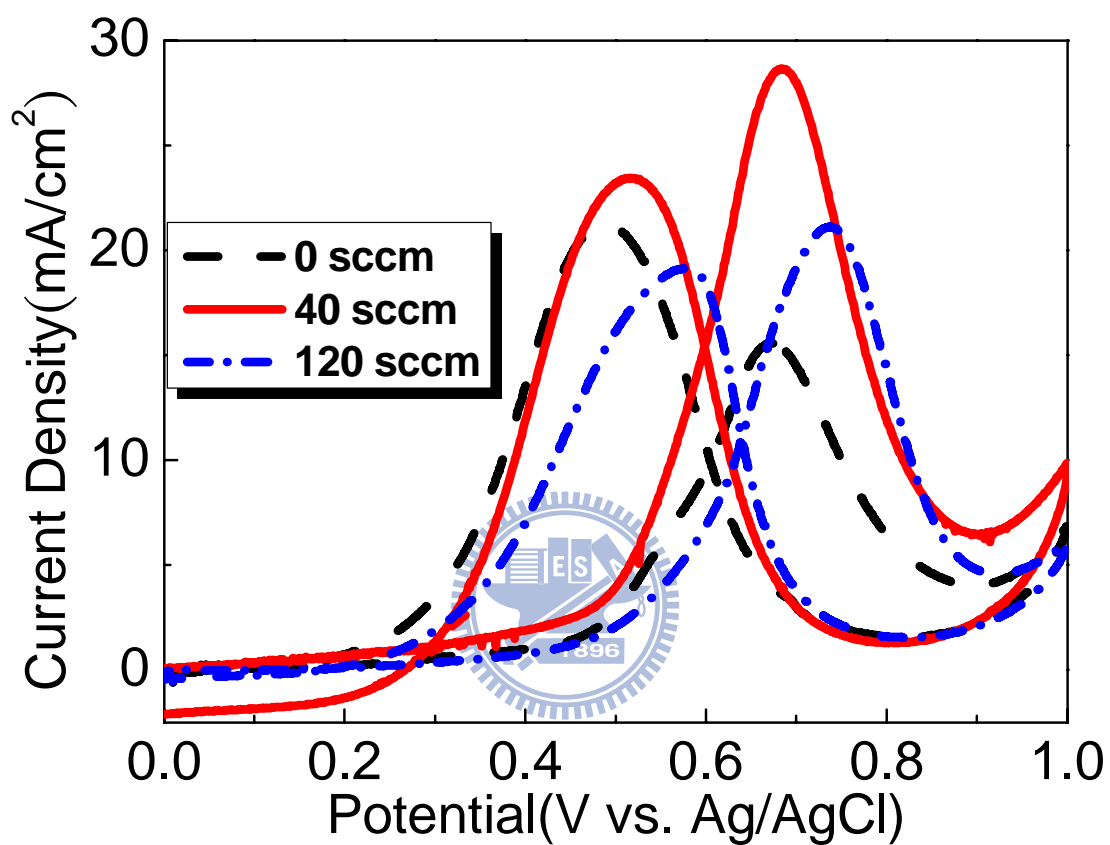


Figure 4.7 Typical CV curve of the arrayed Pt NP-CN_x NT nanocomposites with different N₂ flow rate at a scan rate of 50 mV/s in 1 M CH₃OH + 1 M H₂SO₄ solution.

Chapter 5

Nanostructured ZnO Nanorod@Cu Nanoparticle as Catalyst for Microreformers

5.1 Introduction

The use of hydrogen for energy generation has attracted significant attention in the recent years as a clean, sustainable and transportable fuel alternative, and has consequently sparked a rapid global development of hydrogen fuel cells for electric power generation.[1] Catalytic reformation of hydrocarbons, with careful attention to avoid storage and safety issues,[75,76] is currently the predominant process for hydrogen generation. One of the leading and most promising techniques for hydrogen generation is catalytic reformation of methanol.[77,78] Cu/ZnO-based catalysts are, therefore, of great importance for industrial scale catalytic production of reformat hydrogen.[13] Owing to their wide commercial relevance, Cu/ZnO-based catalysts, prepared via several preparation routes, are being extensively investigated; and substantial improvements in their efficiency of catalytic activity brought about by addition of suitable promoter/support, combination with effective component, and implementation of new preparation techniques have been reported.[14-19,77,78] Unfortunately, use of Cu/ZnO-based

hetero-nanostructures as reforming catalysts is still lacking to date. This inspired us to design the core-shell nanostructured catalyst, consisting of a ZnO nanorod (NR) core and an outer shell of Cu nanoparticles (NPs), *i.e.* NR@NPs, for achieving high efficiency of catalytic conversion.

In addition, the idea of using microreformers is highly attractive for several applications such as on-board hydrogen sources for small vehicles and portable fuel cells (FCs).[79,80] However, two key issues have hindered the realization of microreformers for catalysis, *viz.* poor adhesion between the catalyst layer and the microchannels; and poor utilization of catalyst layer deposited in the form of thick film.[81] Notwithstanding the several approaches investigated to overcome these issues, catalyst immobilization and its efficient utilization inside the microchannel remains a challenge.[82,83] Most of these approaches involve a two-step process, wherein active catalysts are prepared in the first step, followed by its immobilization on the surface of the microchannels in the second step. In this communication, we report a simple and reliable method for integrating *in-situ* synthesis of catalyst and its immobilization for microreformer applications.

5.2 Structural Characterization of Cu Nanoparticle/ZnO Nanorod Nanocomposites

The ZnO NR arrays were first grown on a microchannel-reactor using a simple template-free aqueous approach. A simple mixture of Cu salts, aqueous media and

ZnO NR arrays at low temperature subsequently resulted in spontaneous formation of the cable-like nanostructures. Since the ZnO NR@Cu NP nanocomposites were *in-situ* synthesized directly on microreactor, the arrayed ZnO@Cu nanocomposites were strongly anchored onto the microchannel. This was evidenced by observation of no material loss after sonication in the water for several hours, which highlighted the strong mechanical anchorage of nanostructured catalysts on the surface of microchannel. The interaction between Cu NP and ZnO NR was studied by several analytical techniques, including electron microscopy (EM), X-ray diffraction (XRD), X-ray photoelectron spectroscopy (XPS), X-ray absorption spectroscopy (XAS), and temperature-programmed reduction (TPR). The structure of the microreactor design based on the ZnO NR@Cu NP nanocomposite is illustrated in Figure 5.1, which is evidenced by the photographs comparing the microchannels before and after the deposition of the ZnO NR@Cu NP nanocomposite (see Figure 5.2).

One of the most significant advantages of the core-shell nanocomposites, which are clearly distinct from the traditional catalysts, is the large surface area they offer for effective surface contact between the reactants and catalysts. Figure 5.3a illustrates the cross-sectional SEM image of vertically aligned ZnO NRs grown on the inner surface of the microchannel. The size of the NRs range from 35 to 50 nm in diameter and around 5 μm in height as determined directly from the SEM micrograph. The TEM image of a typical NR is shown in Figure 5.3b, indicating

uneven surface with arrow-marked stacking faults, which is shown in greater detail in Figure 5.3c. Figure 5.3d displays the typical TEM image of ZnO@Cu hybrid nanocomposites at Cu decoration concentration of 2 mM. Close attachment of Cu NPs on the ZnO NR cores can clearly be observed. More detailed TEM images with EDX elemental mapping of Cu and Zn are shown in Figure 5.4, which further confirms the attachment of Cu NPs on the ZnO NR cores. Further, a high-resolution TEM image, shown in Figure 5.3e, yielded the spacing of the { 111 } lattice planes of the fcc copper crystal to be 0.21 nm. A histogram of the diameter of Cu NPs determined from the TEM measurement is shown in Figure 5.3f, indicating a diameter range of 3 to 8 nm with an average of 5 nm. Moreover, a high-resolution TEM image of the Cu NP/ZnO NR heterostructures reveals that the (111) plane of the Cu NP is immobilized on the (002) plane of ZnO NR with clear evidence of the lattice-mismatched region (see Figure 5.5).

Figure 5.6a shows XRD patterns of Cu deposited on ZnO NRs prepared with different Cu decoration concentrations from 1 to 3 mM. A large range XRD patterns can be as reference in the Figure 5.7. No obvious Cu peak could be detected below 1 mM decoration concentration. Figure 5.6a also shows that as the decoration concentration gradually increases, Cu(111) peak at 43.5 degree becomes more prominent. The greater FWHM of this peak for samples prepared with 2 mM and 3 mM decoration concentrations compared to that of the metallic Cu indicates smaller

size of Cu particles in the nanocomposite samples. Furthermore, the FWHM increases as the decoration concentration decreases, indicating formation of finer particles at lower decoration concentration, which is also confirmed in the results of larger Cu surface area and higher dispersion determined via N_2O decomposition method (see Table 5.1). In addition, in Figure 5.6a, a shift in the position of this peak to higher 2θ values as compared to the metallic Cu peak is also observed with decreasing decoration concentration. This can be attributed to the existence of defects at the interface between Cu NP and ZnO NR or partial dissolution of Cu into the ZnO lattice. The defects, either microstrain or structural disorder, can originate at the interface due to the lattice mismatch between Cu and ZnO, but can be quickly overwhelmed by the strong metallic Cu(111) peak from larger sized particles deposited at higher decoration concentrations, as can be observed from Figure 5.6a.

A detailed inspection of the electronic states of the surface metal species was carried out through XPS analysis. Figure 5.6b depicts the Cu 2p core level XPS of NR-Cu composite nanostructures prepared at different decoration concentrations. In order to differentiate between the oxidation states of Cu, the main peak of the Cu $2p_{3/2}$ core level spectra was fitted with two components at 932.8 and 933.7 eV corresponding to Cu^0/Cu^+ and Cu^{2+} species, respectively.[86] It can be seen that a large fraction of Cu is present as Cu^0/Cu^+ after deposition in the nanocomposite samples. Additionally, an absence of any shake-up satellite features in the spectra at

binding energies above 940eV further indicates a lower Cu oxidation state.[87]

When the decoration concentration was decreased, the position of the Cu main peak shifted slightly toward higher binding energy. This is strongly related to the modification of the electron density on smaller Cu species at lower decoration concentrations.[86] Moreover, it appears that the fraction of atomic Cu on the surface, as estimated from the ratio of Cu/(Cu + Zn + O) peaks tends to increase with increasing decoration concentration. In contrast, the fraction of atomic Cu on the surface is lower than 8 at. % while the decoration concentration is decreased to 1 mM, which is consistent with the XRD results in Figure 5.6a. Meanwhile, similar trend can be obtained for the surface ratios of Cu/Zn and ZnO/Cu through XPS measurements (see Table 5.1). However, it is rather unfortunate that Cu⁰ state cannot be distinguished from Cu⁺ state by XPS analysis due to their spectral overlap. X-ray absorption spectroscopy (XAS) measurements were hence used to resolve this issue. The X-ray absorption near edge structure (XANES) spectra are associated with the excitation of a core electron to bound and quasi-bound states. To determine the valence of copper in the arrayed ZnO NR@Cu NP nanocomposites, the Cu K-edge XANES spectra are compared with those of Cu foil in Figure 5.6c. The XANES spectra of arrayed nanocomposites exhibit the edge absorption at 8979 eV together with a well-resolved doublet in the post-edge region. These are in good agreement with that of Cu foil, indicating a predominant presence of metallic Cu in these

nanocomposites. A more detailed understanding may be gained from the derivative of the XANES spectra (see Figure 5.8). The intensity of the edge absorption for arrayed nanocomposites is relatively low compared to that of Cu foil. This could be related to the smaller (nano-sized) dimensions of the Cu particles.[88] Additionally, it may be noted that the nanocomposite samples display lower intensity as well as a shift towards higher energy of the peak at ca. 8990 eV, together with the shoulder around 8984 eV, as compared to the derivative of Cu foil. These features suggest some changes in the chemical environment around the copper species in these nanocomposites. The reason may be attributed to a further distortion of the copper lattice due to the presence of microstrain at the interface between Cu NPs and ZnO NRs. Thus, the XAS results seem to agree well with the XRD results.

To investigate the reducibility of NR@Cu NP nanocomposites prepared at different decoration concentrations, TPR measurements were carried out in the temperature range of 140 to 300 °C, as shown in Figure 5.6d. It is known that the reduction of bulk CuO is indicated by a single reduction peak at a considerably higher temperature of 320 °C.[89] Clearly, the Cu NP-immobilized ZnO NR nanoarchitectures with 2 mM decoration concentration exhibits a significant shift in the position of the reduction peak to lower temperature in addition to the reduction in FWHM of the main peak as compared to that with 3 mM decoration concentration, indicating superior redox properties of the nanocomposites. The advantage of the

NR@Cu NP catalysts can be emphasized by the lower reduction temperature than the commercial catalysts (Cu-ZnO-Al₂O₃; MDC-3: Sud-Chemie) as shown in the same figure. The reason can be attributed to the enhanced dispersion of fine Cu NPs and strong metal-support interaction (SMSI) effect under NR@NP nanosystems, which facilitates the reduction of the supported Cu species. However, at decoration concentrations of higher than 2 mM, the increase in the size of Cu particles plays a predominant role in the structural change of ZnO@Cu nanocomposites, which also weakens the interaction between Cu and ZnO and consequently undermines the catalytic activity.

5.3 Test of Methanol Reforming Reaction

Methanol conversion and hydrogen production rate for the arrayed ZnO@Cu nanocomposites and the commercial catalysts are shown in Figure 5.9a and 5.9b, respectively. Each data point represents a 12-hour experimental run with very small deviation observed with repeated runs, which is indicated by the small error bars in the figures. The methanol conversion rate over the arrayed ZnO@Cu nanocomposites is as high as 93 % with a hydrogen production rate of 183 mmol g_{cat}⁻¹ h⁻¹ at 250 °C. Both these rates are significantly higher than those obtained with the commercial catalysts. Small amounts of CO were detected by CO detector in the outlet gas stream. Surprisingly, the carbon monoxide concentration of only 170-210 ppm was detected during these experimental runs at 250 °C, which is much lower

than ca. 1000 ppm formed by the commercial catalysts. The present results thus provide a promising alternative to the commercial catalyst for use in catalytic generation of high purity hydrogen without necessitating additional processes to remove CO down stream. For a better comparison of the catalytic activities of NR@NP nanoarchitectures and commercial catalysts, kinetic parameters were evaluated from the conversion data.[90] The kinetic constant at a given temperature can be calculated from the equation:

$$\kappa = 1/\tau [\varepsilon x + (1+\varepsilon)\ln (1-x)],$$

where κ , τ , x , and ε are the kinetic constant, contact time, fractional conversion, and fractional expansion of the system, respectively. As shown in Figure 5.9c, the kinetic constant data manifest higher activity of the nanostructured NR@NP arrays than the commercial catalysts. This can be attributed to the greater external surface area, the existence of SMSI effect, the presence of microstrain at the interface, and the modification of electronic structures in the nanocomposites. These effects are consistent with the TEM, XRD, XPS, XANES, and TPR data. Based on the reaction temperature dependence of the kinetic constant, the apparent activation energy was calculated from the slope of the Arrhenius plot (Figure 5.9d). It is evident that the reaction activation energy for the nanostructured NR@NP arrays is noticeably lower (about 27.5 KJ mol⁻¹) than the 36.8 KJ mol⁻¹ of the commercial catalyst, indicating that methanol reforming reaction would proceed significantly faster on these

nanostructured catalysts than on the commercial catalysts. Last but not least, the advantage of the nanostructured NR@NP arrays catalyst is further exemplified by the higher stability (11.5 % reduction after 36 hours operation) in methanol reforming reaction, which is significantly superior to the 33.8 % reduction for the commercial catalysts (see Figure 5.10).

5.4 Summary

In summary, we have successfully demonstrated an easy-to-fabricate route to prepare arrayed ZnO NR@Cu NP heterostructures on the inner surface of microchannels via direct *in-situ* synthesis for microreformer applications. The superb catalytic performance and stability of the Cu NP-decorated ZnO NR nanostructures can be attributed to the larger surface area and enhanced dispersion of fine Cu NPs, formation of microstrain, the modification of electronic structure of Cu species, and the existence of SMSI effect. These results present new opportunities in the development of highly active and selective NR@NP nanoarchitectures for a wide range of different catalytic reaction systems.

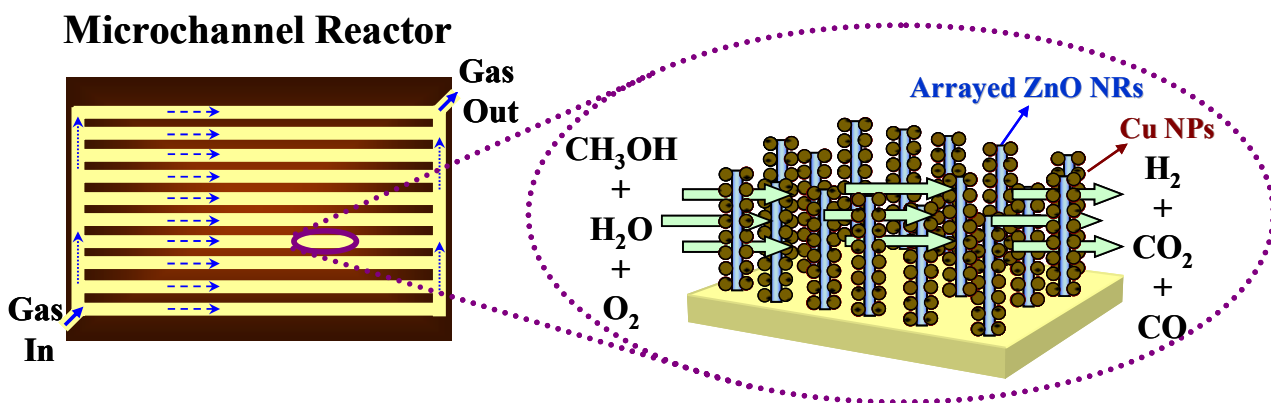


Figure 5.1 Schematic diagram of the novel catalyst ZnO NR@Cu NP arrays grown on the inner surface of microchannel reactor.

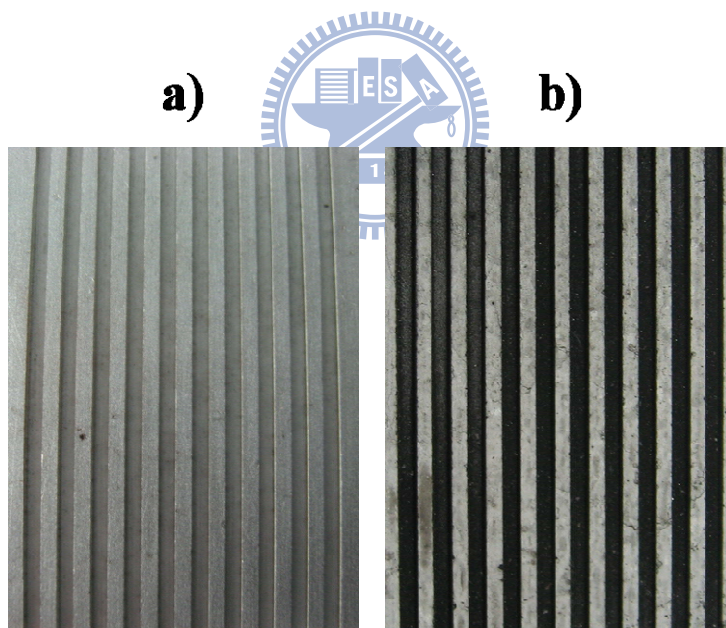


Figure 5.2 Photographs of the microchannels a) before and b) after homogeneously depositing the ZnO NR@Cu NP nanocomposites.

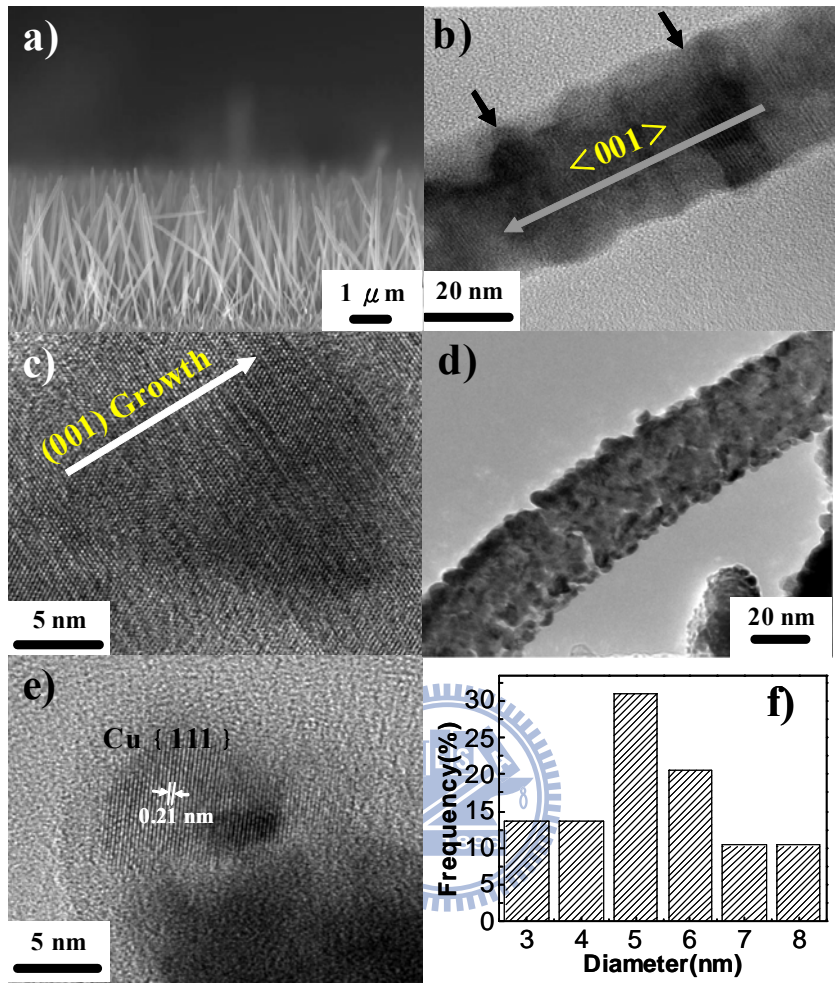


Figure 5.3 a) Cross-sectional SEM image of vertically well-aligned ZnO NRs. b) Typical TEM image of a single ZnO NR showing the presence of stacking faults as marked with arrows. c) HRTEM image of the ZnO NR. d) Typical TEM image of the ZnO NR@Cu NP nanocomposites. e) HRTEM image of Cu NPs on the surface of one single ZnO NR. f) The size histogram of Cu NPs analyzed from the HRTEM image.

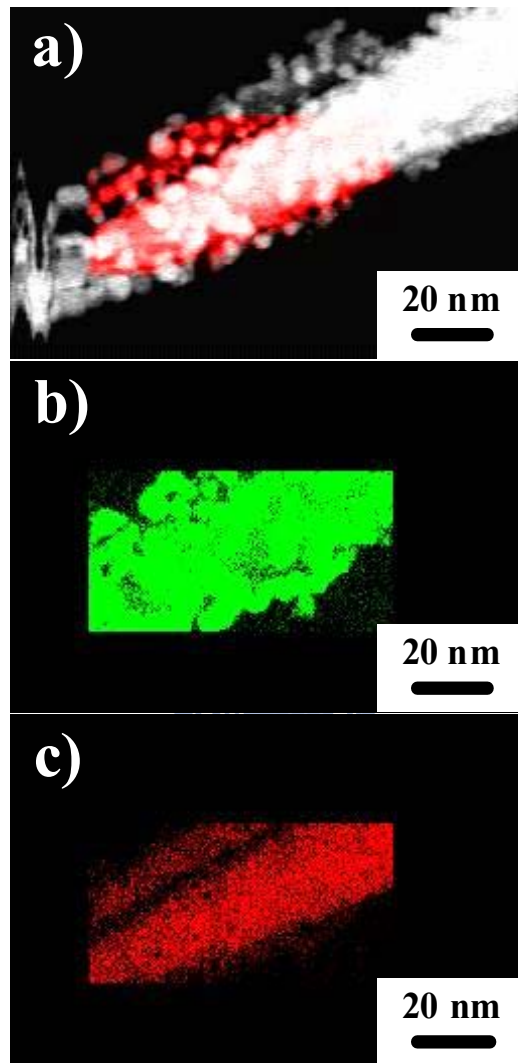


Figure 5.4 a) TEM image and corresponding EDX elemental mapping of b) Cu and c)

Zn.

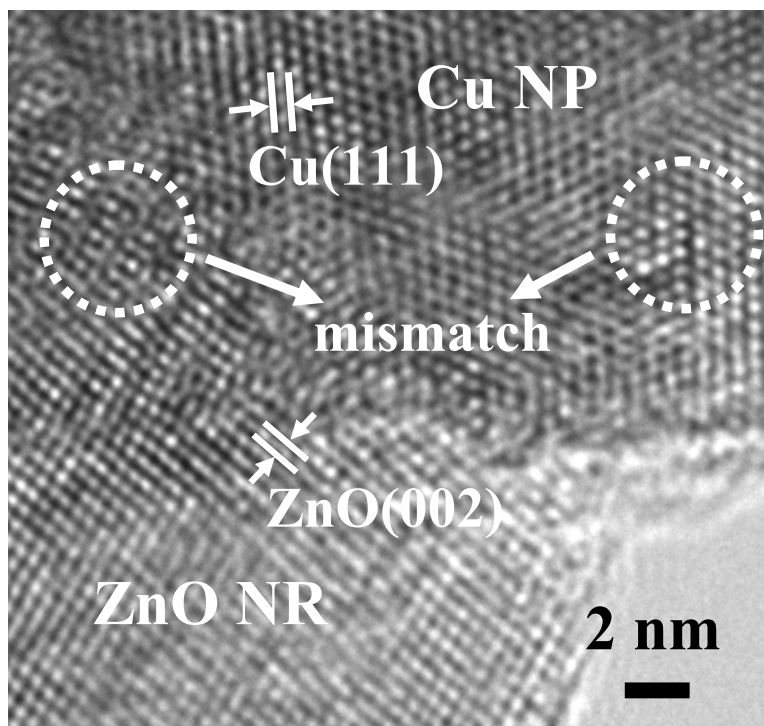


Figure 5.5 HRTEM image of ZnO NR@Cu NP heterostructures.

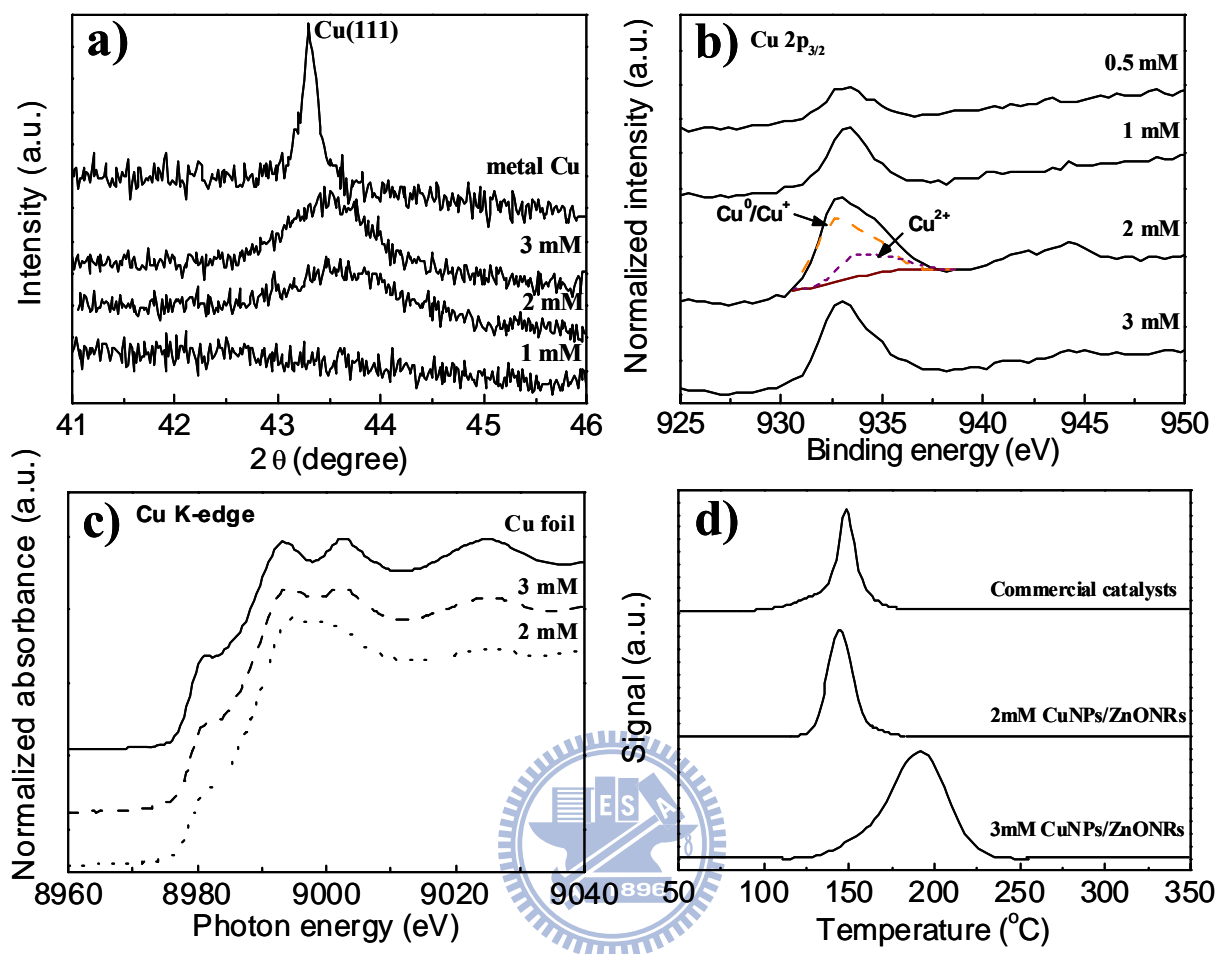


Figure 5.6 a) XRD patterns of Cu NPs on the surface of ZnO NRs prepared with different decoration concentrations from 1 to 3 mM. b) Cu 2p XPS core level spectra of arrayed ZnO NR@Cu NP nanocomposites prepared with different Cu decoration concentrations from 0.5 to 3 mM. c) Cu K-edge XANES spectra of arrayed ZnO NR@Cu NP nanocomposites and bulk reference sample Cu foil. d) Comparative TPR profiles of ZnO NR@Cu NP nanocomposites and commercial catalysts (MDC-3: Sud-Chemie).

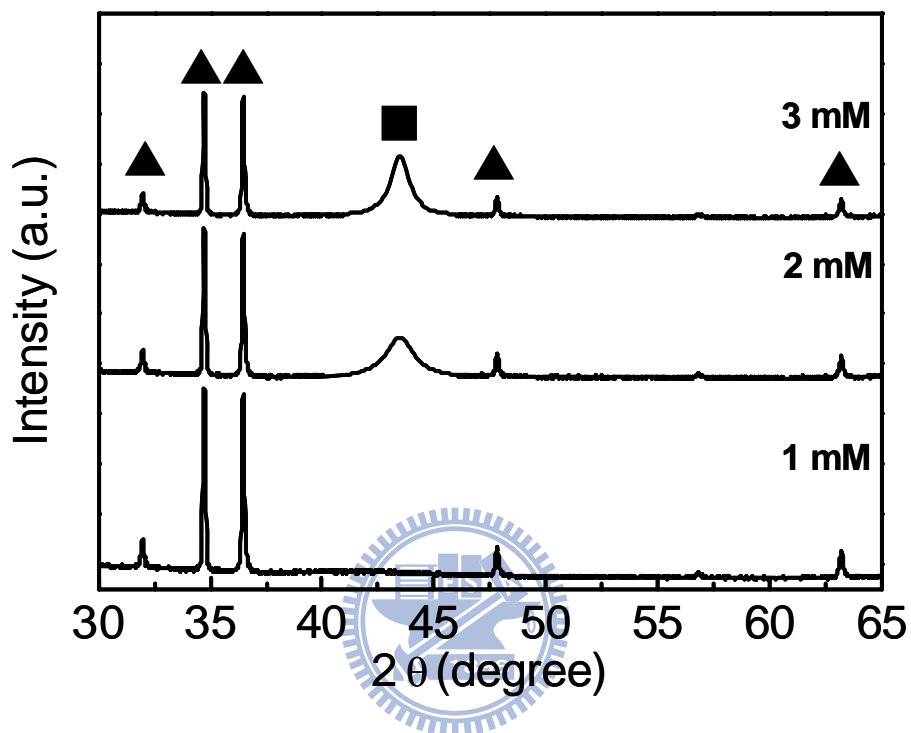


Figure 5.7 Large range of XRD patterns of Cu NPs on the surface of ZnO NRs prepared with different decoration concentrations from 1 to 3 mM. Peaks marked with \blacktriangle are due to ZnO, the other marked with \blacksquare is due to Cu.

Table 5.1 Microstructure properties of Cu NPs on the surface of ZnO NRs prepared with different decoration concentrations.

Catalyst	Cu/Zn surface atomic ratios (at. %)	Cu surface area ($\text{m}^2 \text{g}^{-1}$)	Cu dispersion (%)	ZnO/Cu molar ratios (%)
2mM Cu on ZnO NRs	0.75	42.4	13.5	2.7
3mM Cu on ZnO NRs	1.2	26.3	4.4	1.75

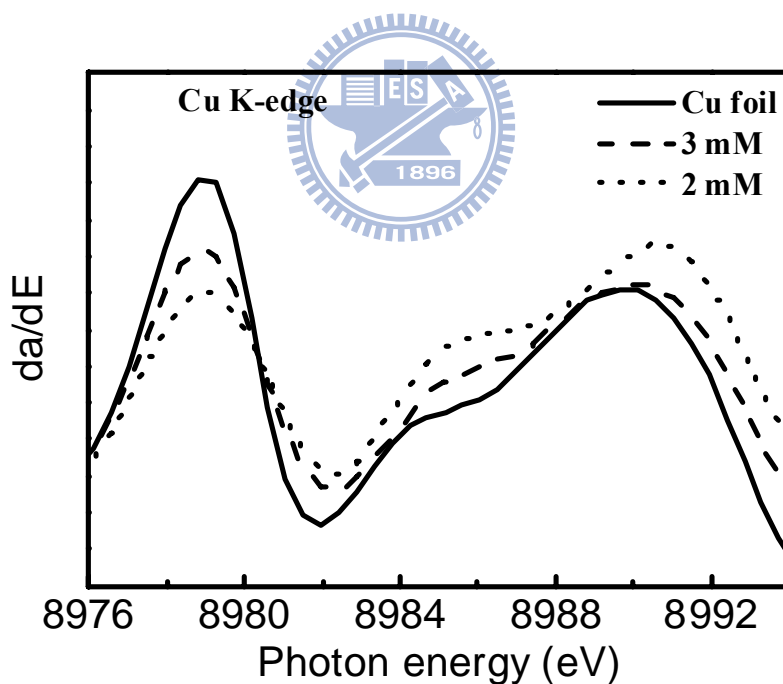


Figure 5.8 First derivative of the Cu K-edge XANES spectra of arrayed ZnO NR@Cu NP nanocomposites and bulk reference sample Cu foil.

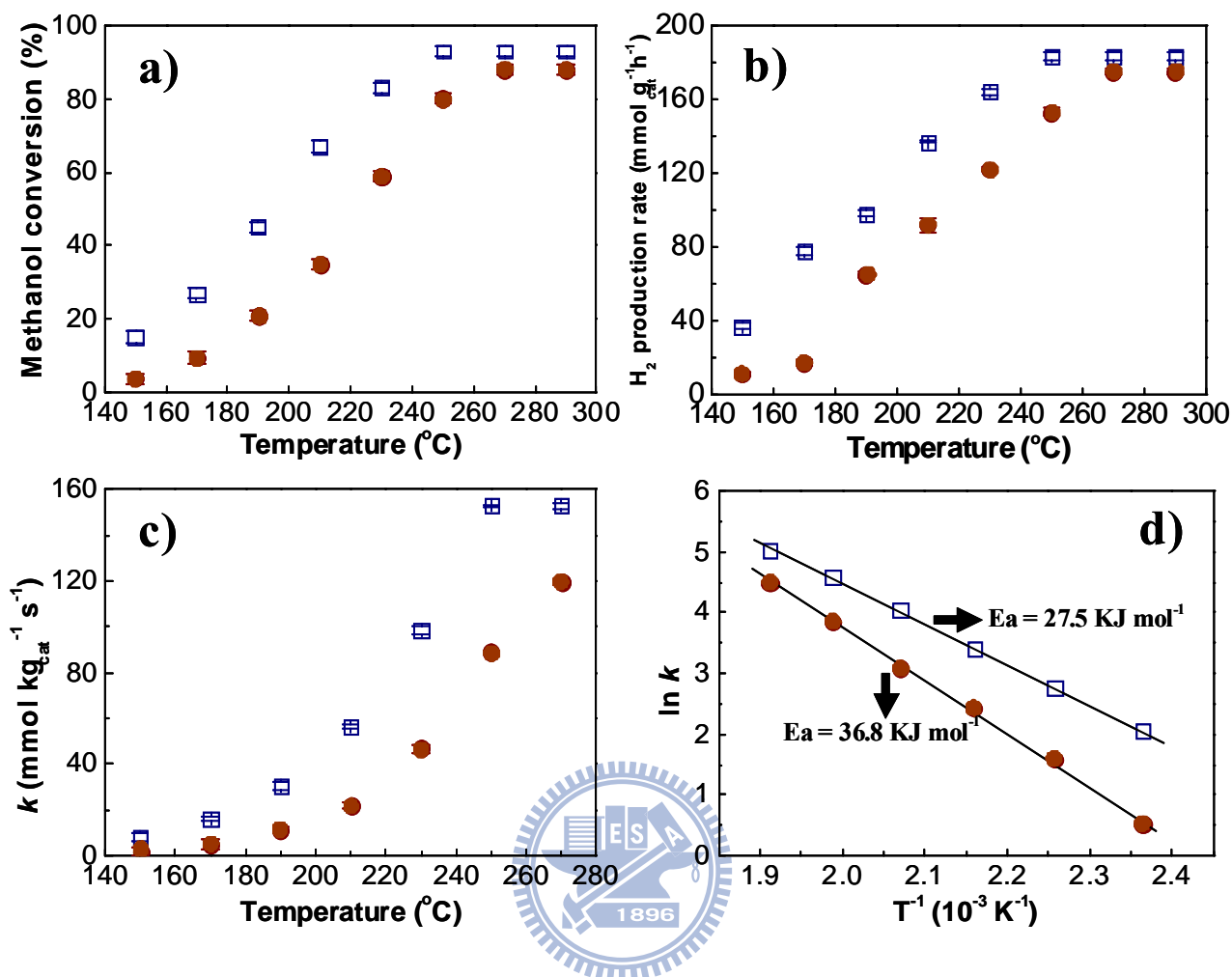


Figure 5.9 a) Methanol reforming reaction profiles for 2 mM arrayed Cu NPs/ZnO NRs nanocomposites (□) and commercial catalysts (●). b) Hydrogen production rate as a function of reaction temperature for 2 mM arrayed Cu NPs/ZnO NRs nanocomposites (□) and commercial catalysts (●). c) Kinetic constants as a function of reaction temperature for 2 mM arrayed Cu NPs/ZnO NRs nanocomposites (□) and commercial catalysts (●). d) Arrhenius plots for methanol reforming reaction for 2 mM arrayed Cu NPs/ZnO NRs nanocomposites (□) and commercial catalysts (●).

Reaction conditions: H₂O/O₂/MeOH = 1/0.125/1, W/F = 21 kg_{cat} s mol⁻¹_{methanol}.

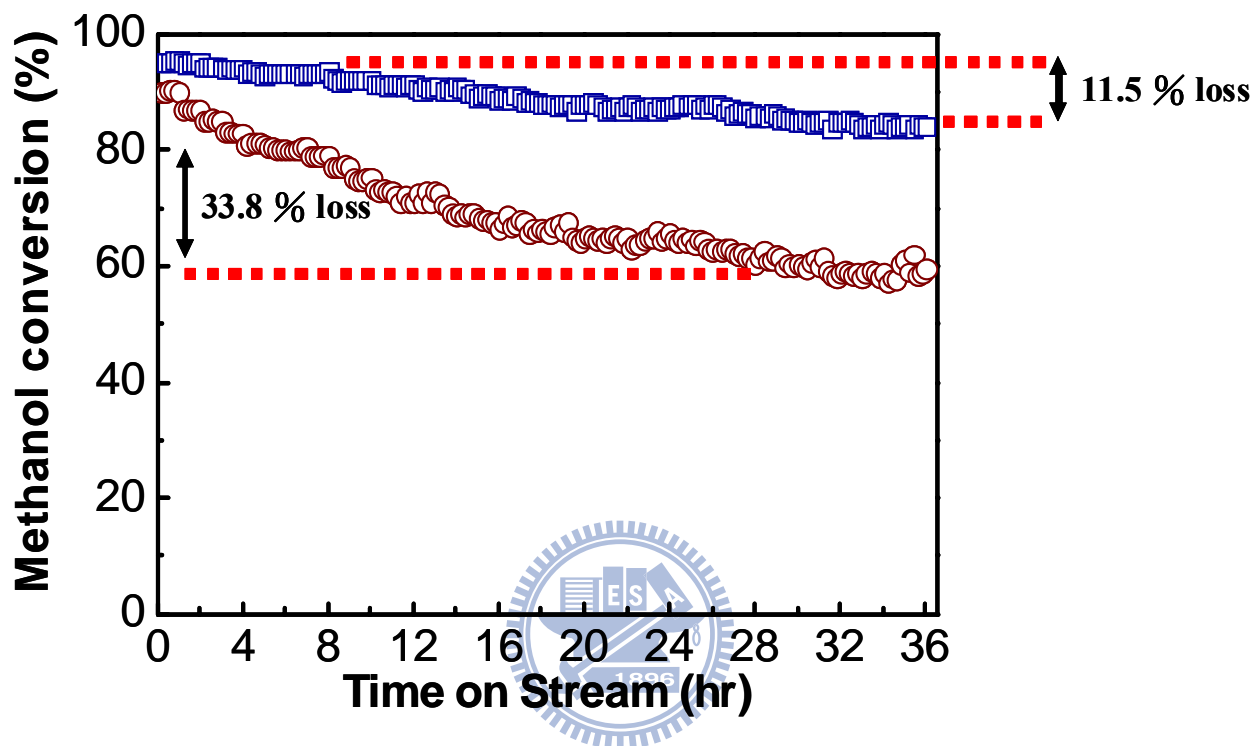


Figure 5.10 Stability tests in methanol reforming reaction over 2 mM arrayed Cu

NPs/ZnO NRs nanocomposites (□) and commercial catalysts (○). Reaction

conditions: $\text{H}_2\text{O}/\text{O}_2/\text{MeOH} = 1/0.125/1$, Temperature = 250 °C, $\text{W}/\text{F} = 21 \text{ kg}_{\text{cat}} \text{ s}$

$\text{mol}^{-1}_{\text{methanol}}$.

Chapter 6

Microwave-Activated CuO Nanotip/ZnO Nanorod Nanoarchitectures for Efficient Hydrogen Production

6.1 Introduction

In the field of development of advanced energy-related devices, nanostructured materials have attracted great interest in recent years due to their intriguing physical and chemical properties that are significantly different from their bulk counterparts.[91-93] Nanostructured catalysts are expected to be the key components in the advancement of future energy technologies. Hence, new strategies for the synthesis of high-performance nanomaterials are widely pursued.[94] In particular, Cu/ZnO-based catalysts have been extensively investigated because of their importance in several industrial applications, such as methanol synthesis, CO removal, and hydrogen generation.[17,35,78,95-99] Nanostructured catalysts consisting of microporous structures are attractive for flow-type gas-solid reactions due to their effective diffusion of reactants and heat. In our previous work, strong metal-support interaction (SMSI) effect in arrayed ZnO NR@Cu nanoparticle (NP) nanocomposites was shown to cause microstrain in the Cu NPs, to which an increase in catalytic performance was attributed.[100]

These findings led us to design and develop a much effective technique to tailor the Cu/ZnO interface.

In recent years, microwave (MW) irradiation has become an effective tool in synthetic organic chemistry, yielding dramatic increases in reaction rates and yields.[101-104] Moreover, since the magnitude of MW absorption is related to dipole oscillation in a material, MW annealing can provide selective heating and lead to a new route for material processing. Recently, application of MW as selective annealing technique has attracted tremendous attention for improving the efficiency of polymer organic photovoltaic devices.[105] In this communication, we report MW treatment of nanoarchitectures of CuO nanotip (NT) on ZnO nanorod (NR) framework as catalyst precursors for methanol reforming reaction (MRR).

6.2 Structural Characterization of CuO Nanotip/ZnO nanorod Nanocomposites

Our initial attempts employing a surfactant-free approach (ammonia-evaporation-induced synthetic method) for synthesis of CuO nanostructures[106] resulted in formation of radiating nanosheets as shown in Figure 6.1a. The high-resolution transmission electron microscopy (HRTEM) image in Figure 6.2 provides specific structural information about an individual nanosheet grown along the $[11\bar{1}]$ direction. Interestingly, while ZnO NRs were introduced as scaffolds for the heterogeneous nucleation and growth of CuO,

different morphologies of CuO were observed, ranging from nanosheet to NT (Figure 6.1b). Figure 6.3 presents the TEM and HRTEM images of CuO NT/ZnO NR catalyst precursors synthesized in this work, showing that NTs not only adhere to but also directly conjoin with the NR. While detailed understanding of the growth mechanism is essential, the nanoarchitecture provides opportunity for advanced applications such as nano-catalysis.

In order to gain an insight into the changes in microstructure, electronic configuration, and reducibility of various CuO NT/ZnO NR catalyst precursors, X-ray diffraction (XRD), X-ray photoelectron spectroscopy (XPS), X-ray absorption spectroscopy (XAS), N₂O titration, micro-Raman spectroscopy, and temperature-programmed reduction (TPR) investigations were performed. Figure 6.4a presents the XRD patterns of CuO NT/ZnO NR catalyst precursors after MW irradiation and conventional thermal annealing. Noticeable shifts in the CuO diffraction peaks are observed, especially after MW irradiation. This is due, presumably, to CuO being partially dissolved in the ZnO lattice, leading to creation of microstrain between NTs and NRs. Moreover, the CuO(111) peak shows a significant up-shift after MW irradiation, implying that a specific MW treatment can enhance the degree of microstructural disorder in CuO NTs. In contrast, there is no remarkable change in the position of CuO(111) peak of NT/NR nanocomposites after conventional thermal annealing. The above

observations are well complemented by the micro-Raman results presented in Figure 6.4b, in which a main peak at around 438 cm^{-1} corresponding to the characteristic $E_2(\text{high})$ vibrational mode of ZnO, and another major peak at about 286 cm^{-1} (A_g mode) attributed to the vibrations of oxygen atoms in CuO were observed.[107,108] Significant variations in peak position as well as full width at half maximum (FWHM) of both $E_2(\text{high})$ and A_g modes occur as a result of the formation of CuO/ZnO nanoarchitectures. These variations are believed to be strongly related to the strain-induced shift and broadening of the phonon modes. Moreover, higher FWHMs of $E_2(\text{high})$ and A_g modes after MW treatment suggest a significant change in band structure of NT/NR nanoarchitectures, indicating that specific MW treatment can enhance the magnitude of lattice distortions. Further evidence is obtained by HRTEM observations (presented in Figure 6.5), that clearly shows a highly distorted lattice as a result of MW irradiation.

Figure 6.4c presents the Cu 2p core level XPS spectra of NR-NT catalyst precursors after MW irradiation and conventional thermal annealing. The position of the main peak, corresponding to Cu $2p_{3/2}$ transition, shifts to higher binding energy for CuO/ZnO catalyst precursors. This clearly indicates a modification of the electron density on CuO species due to the interactive coupling between CuO and ZnO. Furthermore, unlike that for the conventional thermal annealing, the position of the

main Cu $2p_{3/2}$ peak continues to up-shift after MW irradiation. This up-shift results from further distortions of the CuO lattice due to the presence of microstrain between NTs and NRs. This behavior agrees well with the XRD and micro-Raman results discussed above. TPR analysis was also carried out to determine the reducibility of surface oxygen in CuO/ZnO catalyst precursors presented in Figure 6.4d. In contrast to CuO NDs, the CuO NT/ZnO NR catalyst precursors apparently lower the reduction temperature of CuO. This is probably due to weakening of the Cu-O bond due to the presence of strongly bound ZnO species. More surprisingly, CuO NT-immobilized ZnO NR catalyst precursors exhibit a notable shift in the reduction peak to the lowest temperature after MW irradiation, as compared to the conventional thermal annealing. Furthermore, a narrower TPR peak is observed in the MW-treated CuO NT/ZnO NR sample. They indicate far superior redox properties for CuO NT/ZnO NR catalyst precursors, due to the SMSI effect caused by MW irradiation.

6.3 Test of Methanol Reforming Reaction

Figure 6.6a and 6.6b compare the effects of MW and conventional thermal treatments on the methanol conversion as well as hydrogen production rates. After H_2 pre-reduction of CuO NT/ZnO NR catalyst precursors, all experiments were run for 12 hours with a working catalyst (Cu NT/ZnO NR). The chemical state of Cu could be determined via X-ray absorption near-edge spectroscopy

(XANES) measurements (Figure 6.7a), showing all the CuO will turn to metallic Cu (served as active species for MRR). Meanwhile, most experiments were repeated for several catalysts. No significant deactivation of catalysts was noted in these experiments. In addition, the structural factor such as morphology and Cu surface area, which would generally affect the activity of Cu-based catalysts for MRR, have been completely excluded via N₂O titration measurement, showing no remarkable change of Cu surface area (about 45.7 m²g⁻¹) with or without MW irradiation and conventional thermal annealing. The methanol conversion and hydrogen production rates over the pristine Cu/ZnO working catalysts were close to 70 % and 170 mmol g_{cat}⁻¹ h⁻¹ at 290 °C, respectively. Interestingly, after MW irradiation, the methanol conversion and hydrogen production rates increased to 96 % and 230 mmol g_{cat}⁻¹ h⁻¹ (at only 250 °C) respectively, which are significantly higher than those obtained by the conventional thermal annealing of the NT/NR catalysts. Furthermore, the amounts of CO produced in the gas outlet is another indication of the activity. The CO concentration of only 170-210 ppm at 250 °C produced from the MW-treated Cu NT/ZnO NR catalyst is substantially lower than the typically 300 ppm CO produced from a conventional thermal annealed samples. Therefore, the new catalyst developed here represents a promising candidate for use in catalytic generation of high purity hydrogen for fuel cell applications.

Previous investigations pertaining to heat treatment of the catalytic materials using MW irradiation also revealed selective heating of specific catalytic sites and led to “molecular hot spots” in the catalysts.[109] For the binary system comprising CuO/ZnO catalyst precursors, only the CuO component is known to be strong MW absorber.[110] Therefore, hot spot formation at CuO sites decorated on the ZnO support is likely to result in pronounced microstructural rearrangement at the NT/NR interface due to selective MW absorption by CuO. This may account for the good correlation between the increase in defects in NTs and the enhancement in catalytic performance after MW treatment. In this respect, MW processing of the hybrid CuO NT/ZnO NR catalyst precursors appears to provide a unique opportunity for generating significant microstructural deformation at the NT/NR interface due to the formation of hot spots as a consequence of selective dielectric heating, thus leading to the desired creation of highly strained CuO NTs. Last but not least, the advantage of MW-treated NT/NR working catalysts is further exemplified by the excellent stability (only 6 % reduction after 60 hours operation) in MRR as shown in Figure 6.6c. The reason is the chemical state of metallic Cu (served as active species) could be maintained after long-term operation in MRR as shown in Figure 6.7a. This is significantly enhanced comparative to the 11.5% and 33.8% reduction after 36 hours operation for other catalysts without MW-treatment reported earlier.[5] The slight decay of methanol conversion may be due to the decrease of crystallinity in

Cu lattice after continuous 60 hours operation (Figure 6.7b). From extended X-ray absorption fine structure (EXAFS) analyses as shown in Figure 6.7b, a apparent decrease in the intensity of the first-shell (Cu-Cu bonding) over MW-treated Cu NT/ZnO NR working catalysts after long-term operation in MRR could be observed.

6.4 Summary

In summary, we have demonstrated an effective MW-treatment technique to enhance the catalytic activity of CuO NT/ZnO NR nanostructures for MRR. Not only higher conversion efficiency and lower operation temperature, but also lower CO production and remarkably enhanced stability of the MW-treated catalysts have been achieved. It's believed that formation of defects, microstrains and SMSI due to the selective heating by MW-treatment may have contributed to such enhancement in catalyst performance. This finding offers an alternative route using MW-treatment to enhance the activity of a wide range of catalysts.

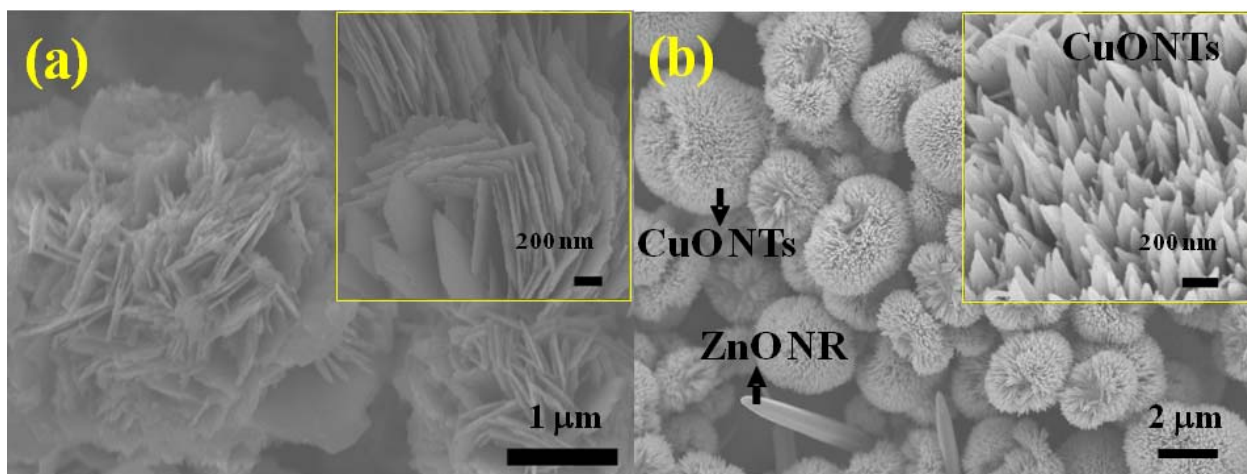


Figure 6.1 (a) SEM images of CuO nanostructures (inset: high magnification). (b) SEM images of CuO NT/ZnO NR catalyst precursors (inset: high magnification).

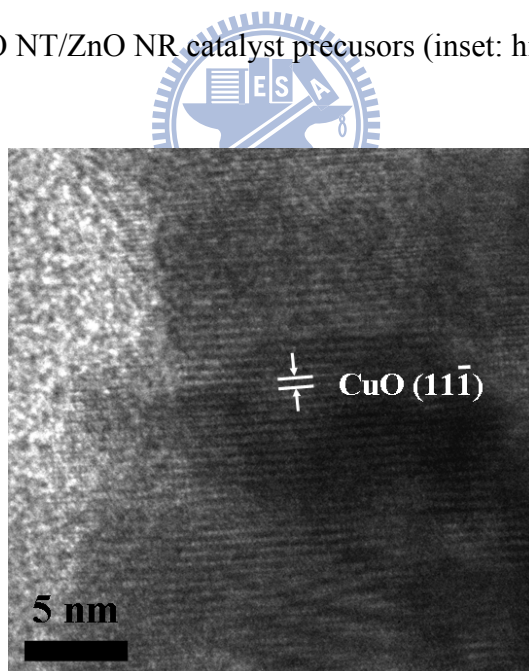


Figure 6.2 HRTEM image of CuO nanodandelions, showing specific structural information about an individual nanosheet grown along the $[11\bar{1}]$ direction.

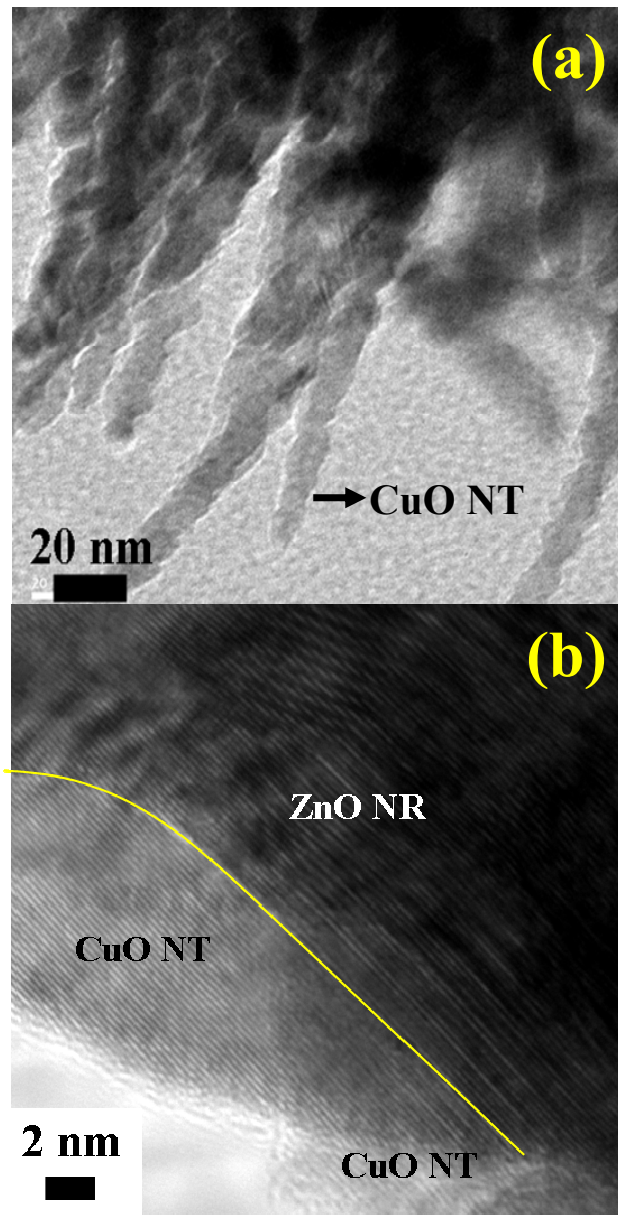


Figure 6.3 (a) TEM and (b) HRTEM images of CuO NT/ZnO NR catalyst precursors, showing that NTs not only adhere to NR but also directly conjoin with the NR.

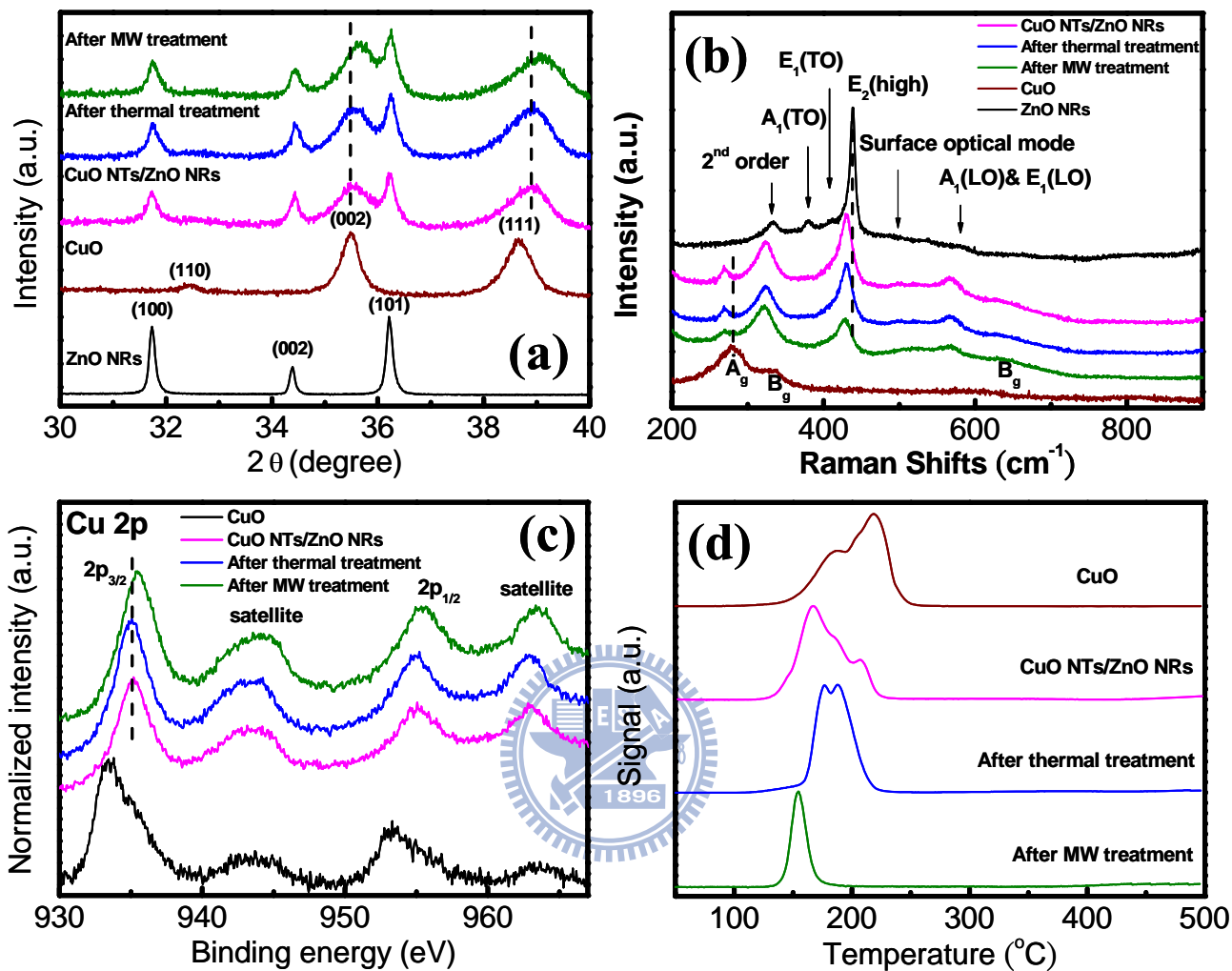


Figure 6.4 (a) X-ray diffraction, (b) micro-Raman, (c) X-ray photo-electron spectroscopy, and (d) TPR spectra of the as-prepared, after thermal treatment, and after MW treatment CuO NT/ZnO NR catalyst precursors.

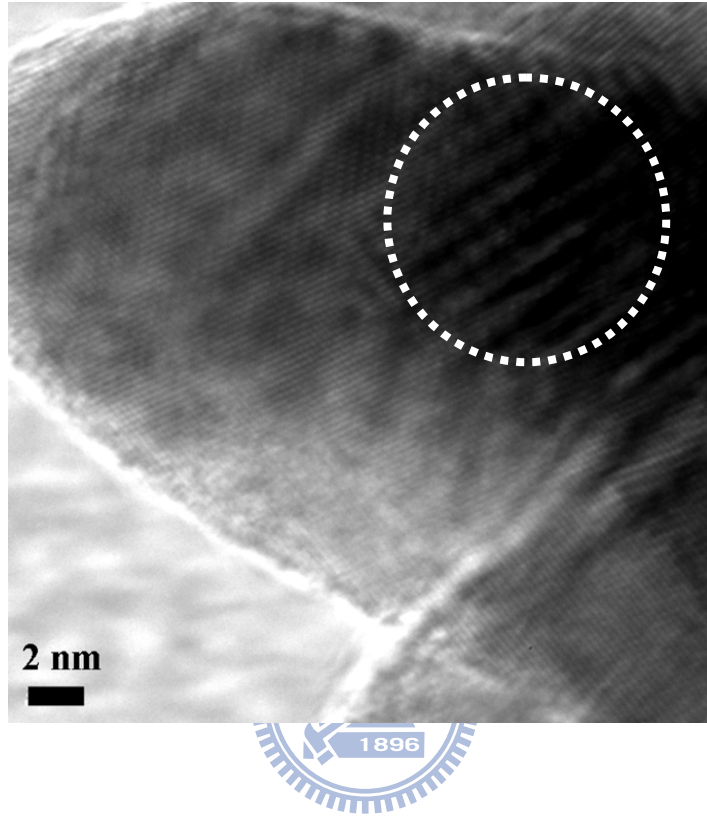


Figure 6.5 HRTEM image of one single CuO NT, clearly showing a highly distorted lattice (indicated by the circle) as a result of MW irradiation.

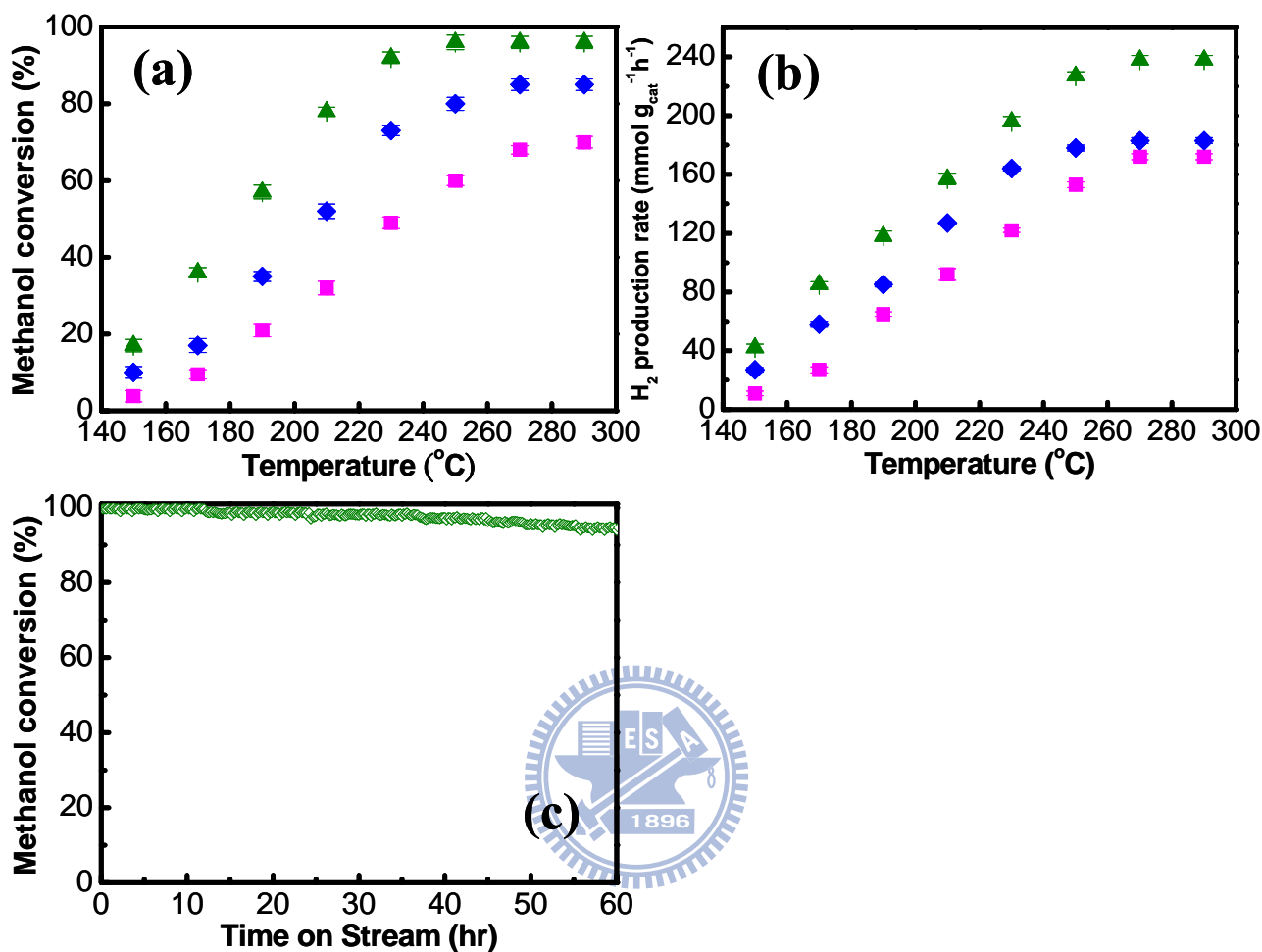


Figure 6.6 Methanol reforming reaction profiles : (a) Methanol conversion rate and (b) hydrogen production rate for Cu NTs/ZnO NRs working catalysts : as-prepared (■), after thermal treatment (◆), and after MW treatment (▲). Reaction conditions: $\text{H}_2\text{O}/\text{O}_2/\text{MeOH} = 1/0.125/1$, $\text{W}/\text{F} = 21 \text{ kg}_{\text{cat}} \text{ s mol}^{-1}_{\text{methanol}}$. (c) Stability test in MRR over MW-treated Cu NT/ZnO NR working catalysts at $\text{H}_2\text{O}:\text{O}_2:\text{MeOH} = 1:0.125:1$,

Temperature = 250 °C, and $\text{W}/\text{F} = 21 \text{ kg}_{\text{cat}} \text{ s mol}^{-1}_{\text{methanol}}$.

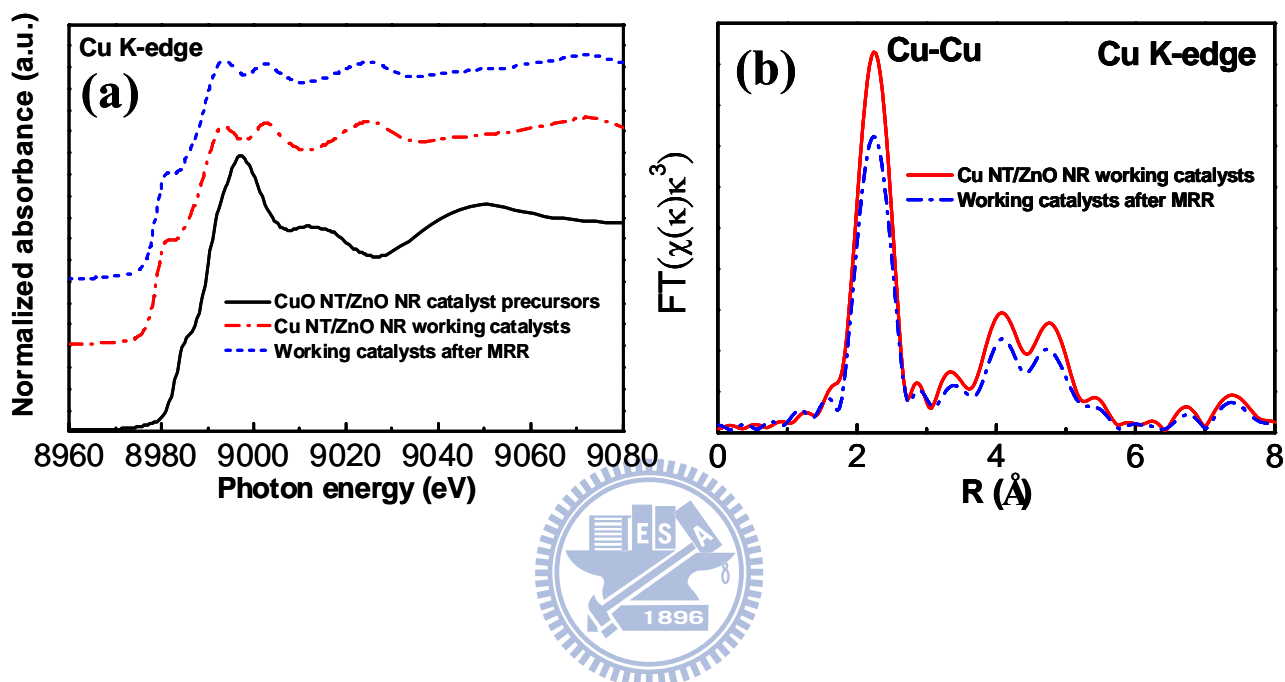


Figure 6.7 (a) Cu K-edge XANES and (b) Cu K-edge EXAFS of CuO NT/ZnO NR catalyst precursors with MW irradiation, MW-treated Cu NT/ZnO NR working catalysts, and MW-treated Cu NT/ZnO NR working catalysts after continuously operating 60 hours for MRR.

Chapter 7

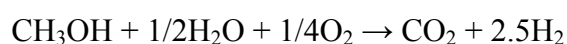
O₂ Plasma-activated CuO-ZnO Inverse Opals as High-performance Methanol Microreformer

7.1 Introduction

Three-dimensionally ordered macroporous (3DOM) nanostructures (so-called inverse opals) have attracted considerable attention in recent time owing to a large variety of their potential applications such as photonic crystals, molecular sieves, catalysts, antireflective coatings, sensors, as well as electrodes for fuel and solar cells.[111] In addition, such well-ordered nanoarchitectures also exhibit several advantages, such as quick transfer of heat and mass, low pressure drop, and high contact area between the catalysts and reactants, that render them ideal for gas catalyses.[112-114] With the recent upsurge in non-conventional energy generation, and environmental and resource conservation research, there is a growing interest in the development of novel catalysts that can effectively and selectively promote the desired reactions related to the production of clean energy.[115] Hydrogen is an efficient energy source that can combine with oxygen in a fuel cell to produce electricity and water without generating pollutants, and thus represents an environmentally benign fuel of the future. Catalytic reforming of methanol in a

microreactor is a promising approach for hydrogen generation for use in portable power sources, which avoids the hydrogen storage and safety related issues.[35,116]

The typical oxidative steam reforming of methanol, which combines the endothermic steam reforming reaction with the exothermic partial oxidation reaction can be generalized as follows[35,116]



However, one of the most critical impediments that hinders the realization of microreformers for catalyses is poor utilization and low efficiency of catalyst layer deposited inside the microchannels, usually in the form of a dense film.[81]

Recent approaches for overcoming this issue typically involve a two-step process, wherein active catalysts are prepared in the first step, followed by its immobilization on the surface of the microchannels in the second step. Various deposition techniques have also been reported for several heterogeneously catalyzed processes in microreactors.[117] These methods, however, do not yield sufficient effective surface required for the reactants to effectively access the catalytically active sites. Therefore, evolution of 3DOM nanoarchitectures that enable integration of direct synthesis of catalyst and its immobilization on the surface is essential for efficient catalytic reforming of methanol at low temperature.

Extensive research efforts are recently being devoted to the syntheses of

various Cu-based catalysts for high-performance methanol reformers or methanol synthesis due to their low cost, environmental friendliness, and natural abundance as compared to the conventional precious-metal catalysts (Pt, Pd).[14,15,17,77,118] More recently, numerous studies have focused on gaining in-depth understanding of the effect of oxide supports/promoters towards enhancement of catalytic performance, including their electronic structure, nanostructure, morphology, and surface defect characteristics.[78,90,92,97,100,119] It is particularly noteworthy that native defects (oxygen vacancies; V_o) on the surface of oxide supports have been shown to generate active entities that facilitate the reforming reaction as well as CO oxidation, when doped with rare earth or transition-metal elements.[120-123] Nevertheless, these doping approaches are unfavorable for the low cost objectives and environmental benignity, especially from the point of view of the lack of “green chemistry”. To address this problem, we have attempted here to employ an extremely simple technique of plasma-treatment to create oxygen vacancies (V_o) on the oxide surface to improve the performance of catalytic methanol reforming reaction (MRR). In this communication, we report for the first time fabrication and characterization of O_2 -plasma activated CuO-ZnO inverse opals as high-performance microreformers for methanol. As can be seen from Figure 7.1, our key strategy in this work is to fabricate 3DOM nanoarchitectures consisting of macropores as well as mesopores to ensure a high surface area, and generation of

oxygen vacancies (V_o) through O_2 -plasma treatment to produce additional active entities for MRR.

7.2 Structural Characterization of O_2 Plasma-treated CuO-ZnO

Inverse Opals

The CuO-ZnO inverse opals were synthesized directly inside the microreactor by simple wet-chemical methods, using the colloidal crystal templating (CCT) approach (Figure 7.2).[111] Polystyrene (PS) opals were first self-assembled inside the microchannels of a microreactor, followed by infiltration with metal precursors (Cu^{2+} , Zn^{2+}) within the voids, and final removal of the opal templates by calcinations. After synthesis, the inverse opals were exposed to O_2 plasma for 3, 5, 10, and 15 min. The microstructural characterization was carried out by using several analytical techniques including electron microscopy (EM), X-ray diffraction (XRD), X-ray photoelectron spectroscopy (XPS), micro-Raman spectroscopy, X-ray absorption spectroscopy (XAS) and N_2 adsorption/desorption. The catalytic performance of O_2 -plasma treated CuO-ZnO 3DOM nanoarchitectures in MRR was systematically evaluated.

Figure 7.3 shows the morphology and microstructure of hierarchical 3DOM nanostructures. The scanning electron microscopy (SEM) image illustrates a continuous oxide framework consisting of an interconnected pore network permeating throughout the structure (Figure 7.3a). The nanoarchitectures

fabricated exhibit a uniform pore size of ~ 300 nm, interconnected by ~ 220 nm windows between the adjacent pores. This represents a shrinkage of about 40% during calcinations since PS beads used as sacrificial templates were of ~ 500 nm size. One of the most significant advantages on the hierarchical 3DOM nanoarchitectures, which are clearly distinct from the traditional catalysts, is the high void fraction resulting in large surface area they offer for effective surface contact between the reactants and catalysts. To further elucidate the inner architectures of the inverse opals, the surface area and porosity were estimated from the nitrogen adsorption-desorption isotherms (Figure 7.4). The nanoarchitectures exhibited a typical type IV isotherm according to the IUPAC classification. The Brunauer-Emmertt-Teller (BET) analysis of the isotherm confirmed the presence of the mesoporous structure with a high specific surface area of $281 \text{ m}^2 \text{ g}^{-1}$, as well as a bimodal pore size distribution of ~ 3.1 and ~ 6 nm, as determined through the Barrett-Joyner-Halenda (BJH) desorption pore distribution method. As a result, this nanoarchitecture provides an isotropic porous structure with easily accessible pore openings from any directions, which is extremely desirable for various electrochemical and catalytic applications. The crystal structure of these inverse opals was studied by XRD analysis, which matched with the JCPDS (No.80-1268) of CuO and JCPDS (No.79-0208) of ZnO. A typical transmission electron microscopy (TEM) image of CuO nanocrystal

(NC) on the ZnO support shows that the surface of CuO NC with a particle size of about 10 nm is partially covered by ZnO, preventing it from sintering during MRR. Additionally, several disordered wormhole-like mesopores (indicated by the circles) are also observed. This agrees very well with the BET results. A higher-resolution TEM image (Figure 7.3b) reveals that the (111) plane of the CuO NC is in contact with the (101) plane of ZnO support. Further investigations with elemental mappings via energy-filtered TEM revealed the presence of uniformly dispersed CuO NCs surrounded by ZnO supports inside the hierarchically inverse opals (Figure 7.5).

In order to gain further insight into the evolution of defects during O₂ plasma-exposure, micro-Raman analyses were performed. Figure 7.3c presents the typical Raman spectra of CuO-ZnO 3DOM nanoarchitectures for different durations of plasma-exposure. The spectra show several peaks characteristic of various vibrational modes of ZnO and CuO. The presence of a sharp and dominant E₂ (high) mode at 438 cm⁻¹, which is associated with the vibration of oxygen atoms in ZnO, indicates the wurtzite nature of ZnO.[124] After plasma treatment, this mode becomes weak and significantly broader, presumably due to the plasma-induced lattice disorder and a change in band structure of ZnO.[124] However, further increase in plasma-exposure time to over 10 min possibly leads to the repair of the structural defects via excess O-doping and results in

re-appearance of a strong E_2 (high) mode. On the other hand, the broad peak at 500-700 cm^{-1} can be deconvoluted into two Lorentzian components viz, A_1 (LO) & E_1 (LO) mode at 575 cm^{-1} (originating from the V_o of ZnO) and B_g mode at 630 cm^{-1} related to CuO, respectively.[124,125] Thus, the concentration of V_o was calculated by integrating the intensity of the 575 cm^{-1} peak and taking its ratio with the sum of the 575 and 438 cm^{-1} peaks. The concentration of V_o on ZnO thus obtained, was plotted as a function of plasma-exposure time (Figure 7.6), which reaches a maximum value at 10 min of plasma-exposure, manifesting the highest concentration of V_o produced by O_2 plasma treatment. In contrast, excess plasma-exposure may cause compensative effect leading to filling up of the oxygen vacancies by O-doping.



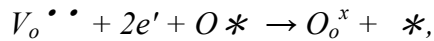
In order to understand the modification of electronic structure in CuO-ZnO inverse opals with O_2 -plasma treatment, XPS measurements were carried out, the results of which are illustrated in Figure 7.7. The O 1s core level spectra of CuO-ZnO 3DOM nanoarchitectures after plasma treatment in O_2 in Figure 7.7A display a slight shift of the main peak towards higher binding energy, likely as a result of the modification in band bending.[126-128] Furthermore, to probe the nature of charge-transfer in CuO-ZnO nanoarchitectures after O_2 -plasma treatment, the XPS spectra for Cu 2p and Zn $2p_{3/2}$ were recorded and are presented in Figure 7.7B and Figure 7.7C, respectively. The shifts in binding energies of the Cu 2p and

Zn 2p_{3/2} spectra after O₂ plasma-treatment are likely due to the transfer of electron from ZnO to CuO. This is consistent with the increase in density of V_o on ZnO surface with plasma treatment, which involves loss of electrons from ZnO.

7.3 Test of Methanol Reforming Reaction

Figure 7.8 compares the effects of material architecture and O₂-plasma treatment on the methanol conversion and rates of hydrogen production during MRR, respectively. After hydrogen pre-reduction, all experiments were run for 20 hours with working catalysts (Cu-ZnO inverse opals). The chemical state of metallic Cu (served as active species) could be determined via XAS measurements (Figure 7.9). Minor deviations were observed in repeated runs, which are indicated by the small error bars in the figures. Notably, the methanol conversion and hydrogen production rates in a microreactor with O₂-plasma treated Cu-ZnO inverse opals for plasma-exposure time of 10 min are nearly 100% and 300 mmol g_{cat}⁻¹ h⁻¹ at a temperature as low as 230 °C, respectively, which are significantly higher than those obtained with the conventional dense-film microstructures (non-inverse opals). SEM image of the Cu-ZnO non-inverse opals clearly shows presence of randomly oriented microstructures (Figure 7.10). The 3-fold enhancement in catalytic activity and consequently hydrogen production rate obtained here correlate well with the introduction of high specific surface area and effective surface modification with O₂-plasma

treatment. Owing to special pore structure, the occurrence of fast gas-solid reactions benefits significantly from proceeding inside the porous transport pathways of 3DOM nanoarchitectures. In addition, O₂-plasma treatment is shown to increase the surface concentration of V_o, which provides more active sites for MRR, based on the equation:



where V_o $\bullet \bullet$, O_o^x, and * are oxygen vacancy, lattice oxygen, and surface active site, respectively.[129] Accordingly, it is well recognized that both hierarchical pore-channel networks as well as surface density of V_o are crucial to the observed excellent catalytic activity. On the other hand, only minor amounts of CO were detected by CO detector in the outlet gas stream. The CO concentration of only 130-170 ppm at 230 °C was detected for the O₂-plasma treated 3DOM nanoarchitectures with plasma exposure time of 10 min. This result can be attributed to a higher surface density of V_o as a result of the O₂-plasma treatment. It is believed that the V_o can generate lattice oxygen that, in turn, catalyzes the CO oxidation reaction.[122] Previous investigations have pointed out that the presence of V_o plays an important role in CO oxidation reaction due to the fact that they provide sites for oxygen activation by formation of O₂⁻ anion radicals.[130] Likewise, the energy calculations also confirm that the presence of V_o promotes CO oxidation reaction.[131] Thus, the unique

nanoarchitecture developed in this study certainly provides a promising alternative for catalytic generation of high purity hydrogen without requiring a complex combination of multiple CO-clean systems to produce clean electrical energy from small fuel cells for automotive applications. Last but not the least, the advantage of O₂-plasma treated inverse opals is further exemplified by the outstanding stability (a minimal degradation rate of only 10% after 80 hours of continuous operation) in MRR, which is significantly superior to the 31% reduction for the commercial catalysts (Figure 7.8b). The XRD results on pre- and post-reaction inverse opals show no apparent difference in the crystal structure. SEM observations of the post-reaction inverse opals also confirm that the microstructure is essentially unchanged, although some small fraction of macropores appeared to have collapsed.

7.4 Summary

We have successfully demonstrated an easy route to fabricate a novel CuO-ZnO catalyst with well-defined inverse opal nanostructure on the inner surface of microchannels, via direct synthesis, for microreformer applications. The 3DOM nanoarchitectures have distinct advantages in terms of enhanced catalytic activities since they possess a high specific surface area as well as enable effective transport of reactant molecules to the active sites. The V_o-rich Cu-ZnO inverse opal obtained in this study at a low-reaction temperature of only 230 °C yields complete conversion

methanol, high hydrogen production rate ($300 \text{ mmol g}_{\text{cat}}^{-1} \text{ h}^{-1}$), low CO formation (130-170 ppm), and outstanding stability (after continuous 80 hours of operation), making it exceedingly promising toward MRR. The present results prove that catalytic performance of Cu-ZnO catalysts for MRR can indeed be improved through control not only of hierarchical pore-channel networks but also of V_0 induced by O_2 -plasma treatment. These efforts open up new opportunities in the development of highly active and selective nanoarchitectures for a wide range of different catalytic reaction systems.



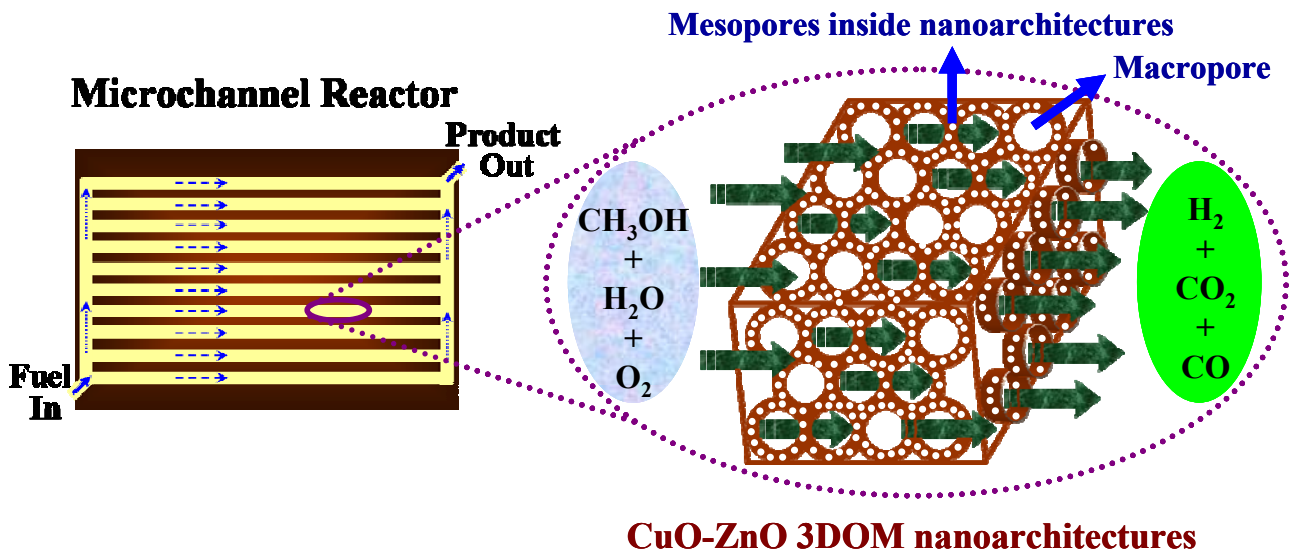


Figure 7.1 Schematic diagram of the novel catalyst CuO-ZnO inverse opals

fabricated on the inner surface of microchannel reactor.

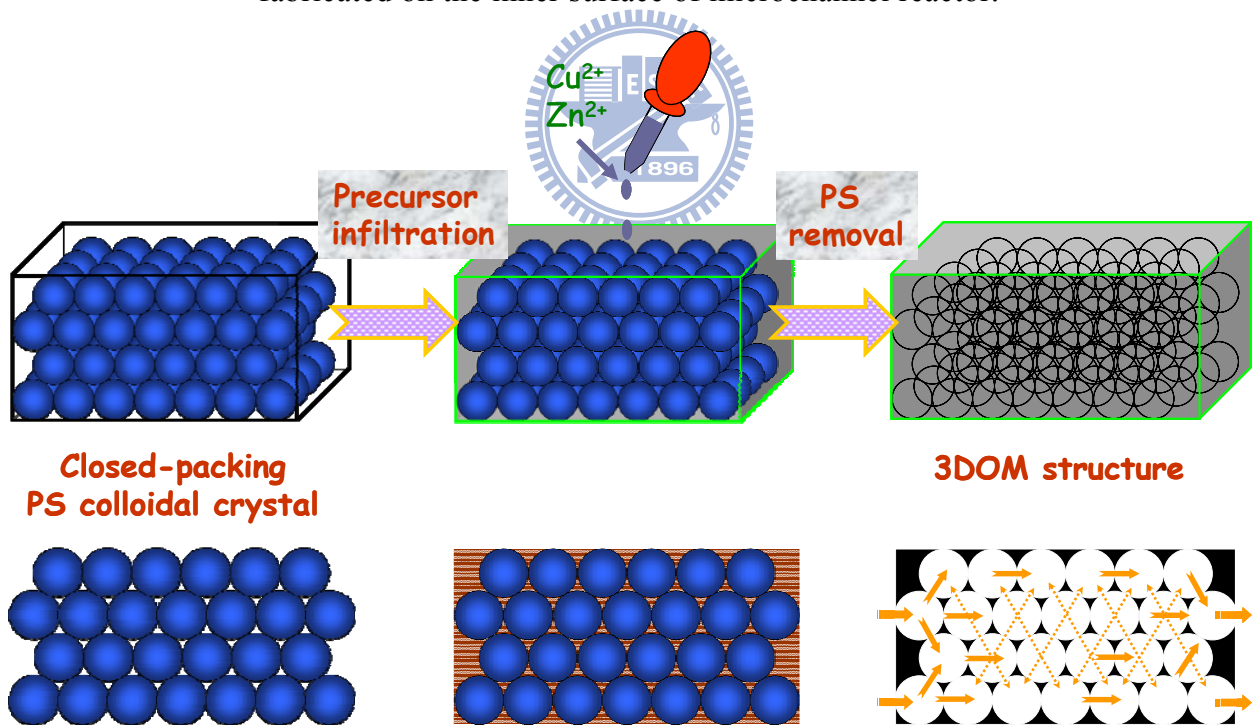


Figure 7.2 Procedure for the preparation of CuO-ZnO inverse opals using

polystyrene colloidal crystal templates.

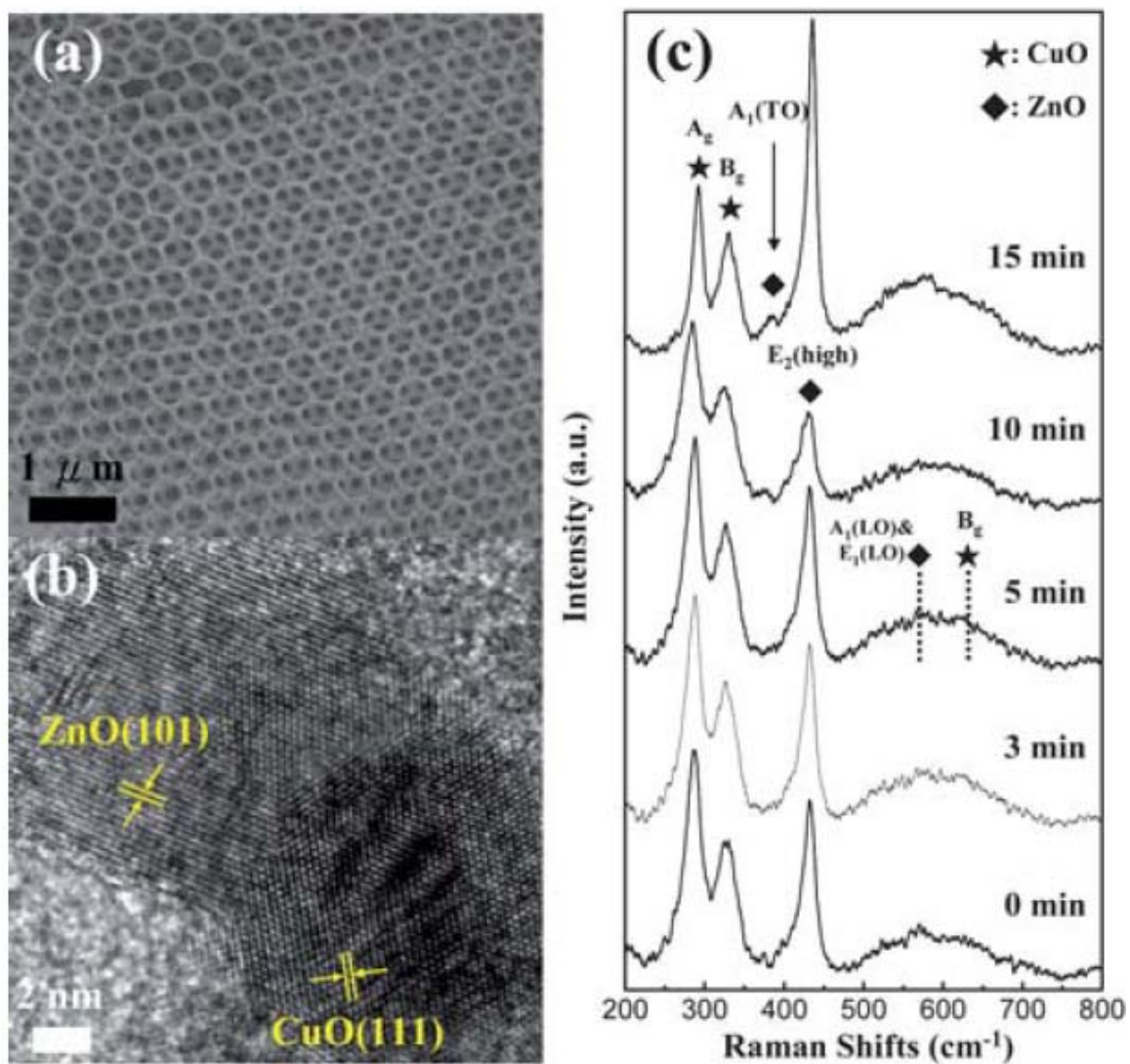


Figure 7.3 (a) SEM image and (b) HRTEM image of CuO-ZnO 3DOM nanoarchitectures. (c) Micro- Raman spectra of CuO-ZnO inverse opals with different O₂-plasma exposure durations.

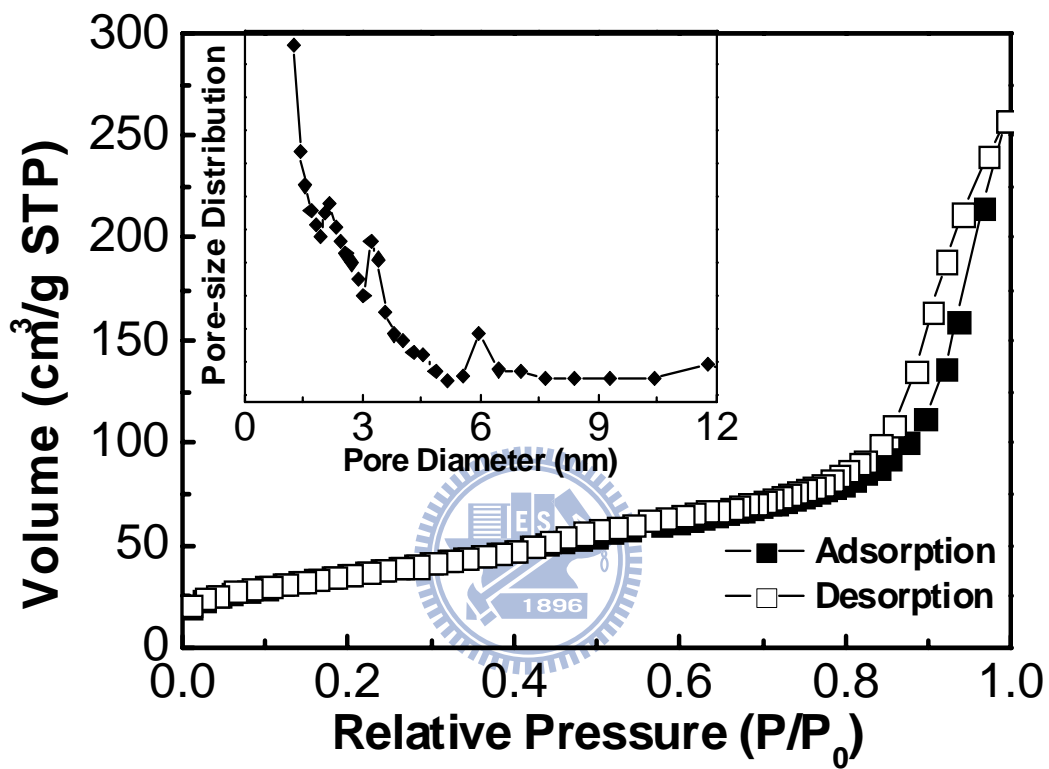


Figure 7.4 N₂ adsorption-desorption isotherm and pore-size distribution (inset) of CuO-ZnO inverse opals without O₂-plasma treatment.

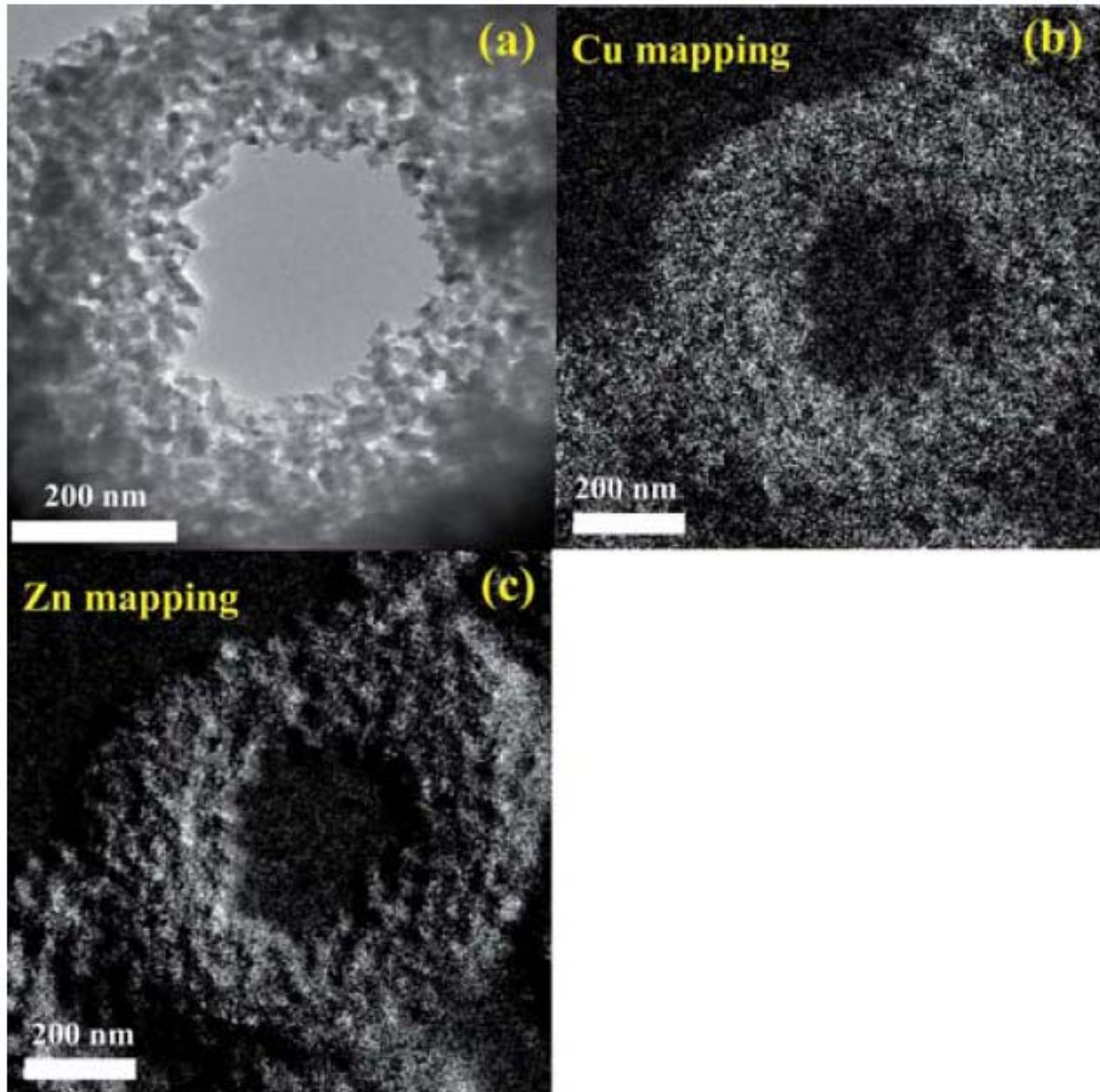


Figure 7.5 (a) TEM image of CuO-ZnO inverse opals. Corresponding energy-filtered TEM (b) copper and (c) zinc mapping images of CuO-ZnO inverse opals.

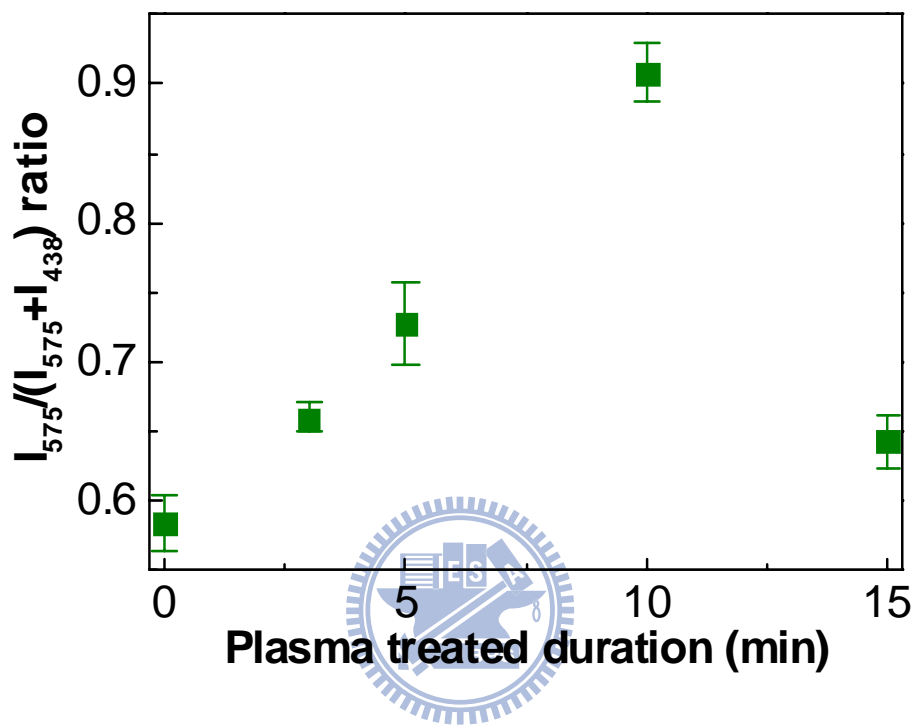


Figure 7.6 Relative ratio of the integrated 575 cm^{-1} peak intensity to the sum of the 438 and 575 cm^{-1} peaks as a function of O_2 -plasma exposure time for CuO-ZnO inverse opals.

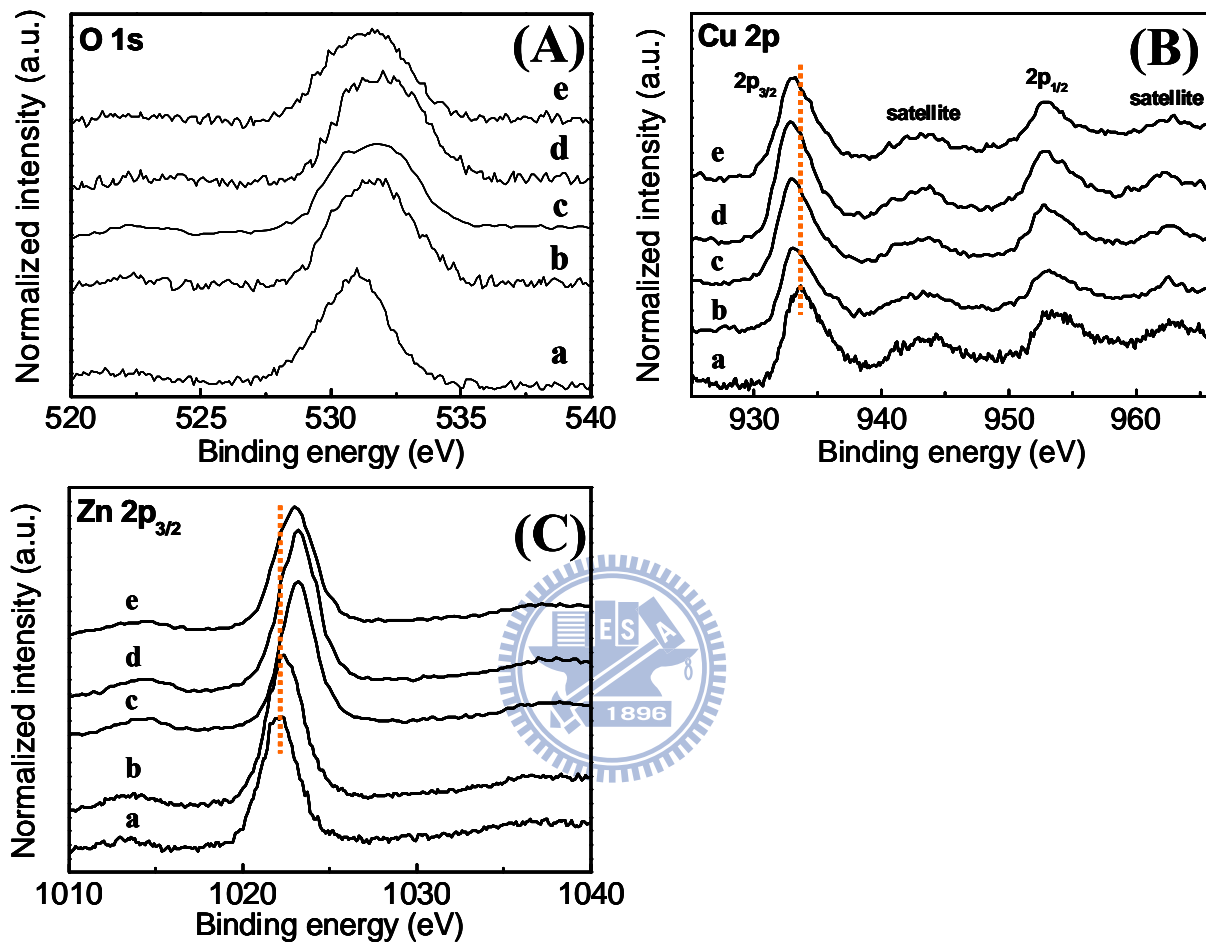


Figure 7.7 XPS spectra of (A) O 1s, (B) Cu 2p, and (C) Zn 2p_{3/2} transitions for CuO-ZnO 3DOM nanoarchitectures after O₂-plasma treatment for (a) 0, (b) 3, (c) 5, (d) 10, and (e) 15 min, respectively.

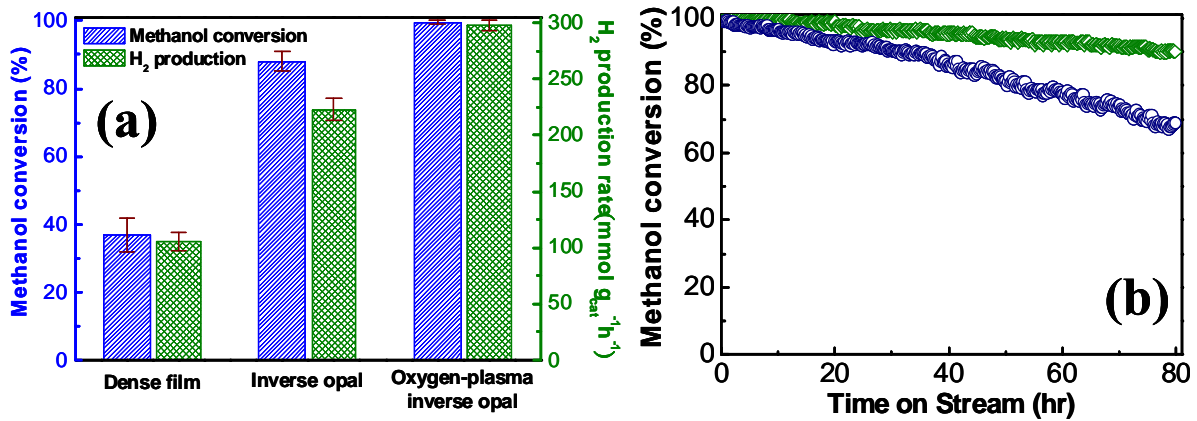


Figure 7.8 (a) Rates of Methanol conversion and H₂ production for Cu-ZnO catalysts with dense film, inverse opal, and O₂-plasma treated inverse opal nanostructure, respectively. (b) Stability tests of MRR with O₂-plasma treated Cu-ZnO inverse opal for plasma exposure time of 10 min (◇) and commercial catalysts (○). Reaction conditions: H₂O/O₂/MeOH = 1/0.125/1, Reaction

temperature = 230 °C, W/F = 21 kg_{cat} s mol⁻¹_{methanol}.

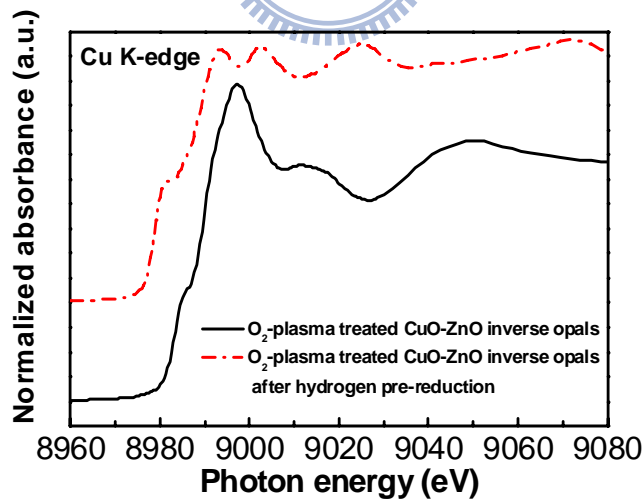


Figure 7.9 Cu K-edge X-ray absorption near-edge spectroscopy (XANES) of O₂-plasma treated CuO-ZnO inverse opals and O₂-plasma treated CuO-ZnO inverse opals after H₂ reduction. From XANES analysis, after H₂ reduction of O₂-plasma treated CuO-ZnO inverse opals, all the CuO will turn to metallic Cu.

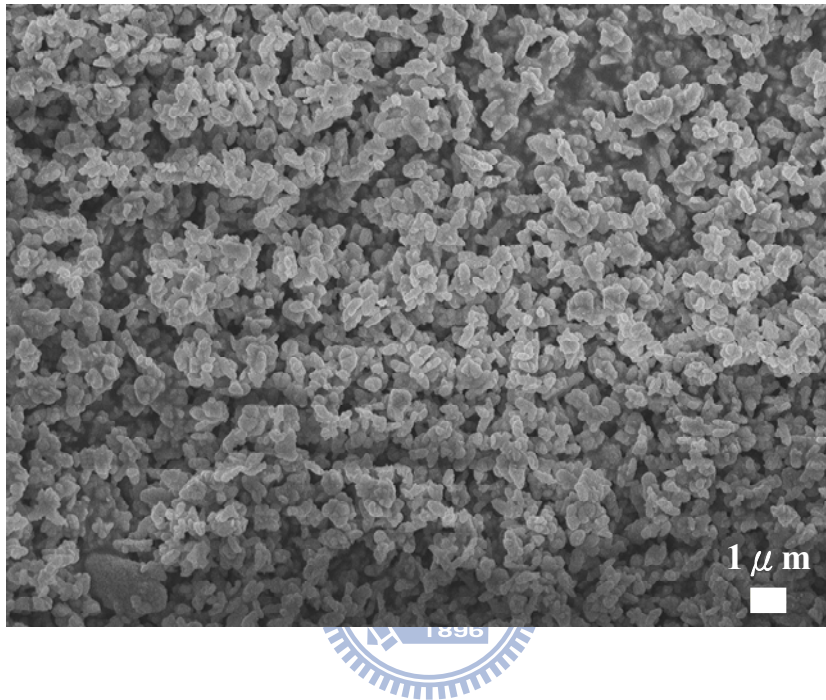


Figure 7.10 SEM image of Cu-ZnO catalysts with non-inverse opal nanostructure.

Chapter 8

Enhanced Photocatalytic Activity with Carbon-Modified ZnO Inverse Opals for Solar Water-Splitting

8.1 Introduction

The success in the development of inverse opals in the past decade suggests their indispensable role in a wide range of fields, from optical computing and telecommunication to photocatalyst and photovoltaic cell.[111] Particularly, increasing the effective optical path length of incident light to promote a more efficient absorption of solar photons through highly periodic nanoarchitectures presents a potential alternative and attractive approach to enhance the efficiency of solar-related applications.[132,133] For example, by reducing the group velocity of light at energies near the edge of the photonic stop-band, a higher probability of absorption was achieved and the photodegradation efficiency of inverse opals doubled.[133] In addition, well-ordered nanoarchitectures of photonic crystals have also been successfully utilized in the modification of the absorption bands of dye sensitizers due to the photonic bandgap effect in solar cells.[132] As a result of the recent ecological and energy crises related to fossil fuel dependence, there is a growing interest in the development of novel and nanostructured materials for the

production of clean energy.[115,134] Hydrogen is an effective energy source that can combine with oxygen in a fuel cell to produce electricity and water without generating pollutants, and thus represents an environmentally benign fuel of the future. However, today the main production of hydrogen comes from catalytic reforming of hydrocarbon fuels, consuming natural resources and generating carbon dioxide as an undesired byproduct.[35,100] Thus, central on direct solar energy conversion to hydrogen via photoelectrochemical (PEC) water-splitting is a fascinating route with advantages of green processing and energy savings.[23,25,42] The light-harvesting efficiency of photoelectrodes is of great importance for hydrogen generation using solar-powered water-splitting. In this regard, evolution of hierarchical inverse-opal nanoarchitectures is exceedingly essential for their immense potential of efficient solar driven hydrogen production due to the extraordinary properties of photonic bandgap and slow photons, which can significantly improve the confinement and localization effect of incident light thereby enhancing the effective interaction of light with photoactive materials.

In the search for a semiconductor which can facilitate the efficient storage of solar energy in the form of hydrogen via PEC cells, ZnO remains a favorable material.[135-137] With the appropriate flat band potential, low electrical resistance, nontoxic nature, low cost, and resource abundance, its use as a photoelectrode in the application of PEC water-splitting at a scale corresponding to the world energy

demand is realistic.[138] The seminal achievements to study ZnO as an oxygen-evolving photoanode for the light-driven decomposition of water detailed its promising aspects and limitations. As major drawbacks, ZnO possesses quick recombination of photoinduced electron-hole pairs, poor optical absorption ability toward visible-light irradiation, and photoinstability in aqueous solution, which intrinsically confine the integrated performance of solar energy conversion devices.[139] Recently, extensive research efforts have been devoted to straightforwardly overcome these disadvantages during the photocatalytic reactions by surface modification of ZnO, such as doping by carbon and hybridization with carbon-containing species.[140,141] Therefore, it is reasonable to expect that an effective integration of ZnO inverse opal and carbon hybridization would lead to a highly desirable photoanode with enhanced solar-hydrogen efficiency and long-term durability in an aqueous environment. In this communication, we elucidate for the first time the synergistic effect of optical amplification with surface hybridization on the enhanced solar conversion efficiency of ZnO inverse opals modified by carbon in a non-sacrificial electrolyte. By *in-situ* incorporating carbon into the matrix of ZnO inverse opals through direct pyrolysis of the blends of ZnO and polymer opal, higher probability of absorption is achieved and the lifetimes of photoinduced electron-hole pairs are extended as well as significant photoresponse in the visible region is obtained.

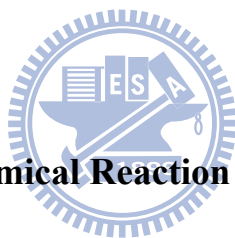
8.2 Structural Characterization of Carbon-modified ZnO Inverse Opals

Figure 8.1 shows the morphology and microstructure of hierarchical inverse-opal nanoarchitectures. The scanning electron microscopy (SEM) image illustrates a continuous oxide framework consisting of an interconnected pore network permeating throughout the structure (Figure 8.1a). The nanoarchitectures fabricated exhibit a uniform pore size of ~ 360 nm, interconnected by ~ 220 nm windows between the adjacent pores. This represents a shrinkage of about 30% during calcinations since PS beads used as sacrificial templates were of ~ 500 nm size. One of the most significant advantages of the inverse opals, which are clearly distinct from the traditional photoelectrodes, is hierarchical pore-channel networks they offer for effective surface contact between the incident light and photoelectrodes. A high-resolution transmission electron microscopy (HRTEM) image of inverse opal is presented in Figure 8.1b, yielding the spacing of the (101) lattice plane of the hexagonal ZnO crystal to be 0.24 nm. Besides, Figure 8.1c and 8.1d provide additional bright-field and high-angle annular-dark-field (HAADF) scanning TEM images, showing that Zn atoms are homogeneously distributed in the whole structures due to the large difference of atomic number between Zn and O. Further investigations with elemental mappings via energy-filtered TEM reveal the presence of uniformly dispersed carbon atoms inside the ZnO inverse opals (Figure 8.2a and

8.2b). The formation of remained carbon could be attributed to the low calcination temperature at 300 °C, which is not enough to completely remove opal template.

In order to obtain better understanding on the electronic structures of the carbon-modified ZnO inverse opals, we performed systematic XPS and XAS studies. The C 1s core level spectra of carbon-modified ZnO inverse opals in Figure 8.2c display a main peak at 285 eV and a shoulder peak around 288.3 eV. The main peak, which is normally located at 284.6 eV, arises from adventitious elemental carbon or graphite-like bonding, while the shoulder peak corresponds to C-O bonding species.[93] Obviously, a slight up-shift of the main peak position with the occurrence of a shoulder peak could be obtained as a result of the strong interaction between carbon and ZnO by means of incorporation of carbon atoms into the ZnO lattice. Furthermore, extended X-ray absorption fine structure (EXAFS) spectra taken around the Zn K-edge of carbon-modified ZnO inverse opals are presented in Figure 8.2d. A apparent decrease in relative intensity and interatomic distance of the first-shell and second-shell (Zn-O and Zn-Zn bonding) over carbon-modified ZnO inverse opals would be observed compared to pure ZnO structure. The reason may be mainly due to the strong distortion of the ZnO lattice resulted from positioning of carbon in ZnO framework. Figure 8.3 shows the O K-edge XAS spectra of carbon-modified ZnO inverse opals. The spectral features can be interpreted as follows: the region between 530 and 538 eV can be attributed to the hybridization

between O 2p and Zn 4s states followed by the region between 539 and 550 eV which is due to the hybridization between O 2p and Zn 4p states.[142] The increase in relative intensity of spectral feature at ~531-535 eV observed in carbon-modified ZnO inverse opals compared to pure ZnO structure indicates the increase of the unoccupied density of states (DOS) of O 2p-Zn 4s hybridized states, which may be caused by strong hybridization of C-O bonds.[142] In addition, the broadening of the absorption peak at ~537 eV over carbon-modified ZnO inverse opals in comparison with pure ZnO structure is assigned to the presence of oxygen vacancies, suggesting that carbon incorporation would induce oxygen vacancies in ZnO lattice.[142]



8.3 Test of Photoelectrochemical Reaction

In order to address the quantitative correlation between carbon incorporation and light absorption of carbon-modified ZnO inverse opals, we performed incident-photon-to-current-conversion efficiency (IPCE) measurements to study the photoactive wavelength regime as shown in Figure 8.4a. In addition to achieve the maximum IPCE value of 95%, it should be noted that the IPCE of carbon-modified ZnO inverse opals at the incident wavelength of 400 nm is up to 26.6%, implying that carbon modification substantially improves the light collection and conversion efficiency in the visible region of interest in comparison with pure ZnO structure. This result is in good agreement with UV-vis absorption data (Figure 8.5).

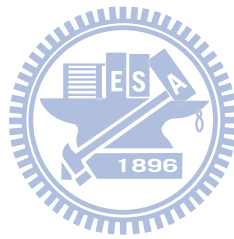
Systematic electrochemical measurements were carried out to evaluate the PEC properties of photoanodes fabricated from carbon-modified ZnO inverse opals. Figure 8.4b shows a set of linear sweep voltammograms without sacrificial reagents in the dark and with illumination of 100 mW/cm². Dark scan linear sweep voltammograms from -0.19 to +1.0 V show a small current in the range of 10⁻⁷ A/cm². In comparison to ZnO noninverse-opal structures, carbon-modified ZnO inverse opals exhibit a striking enhancement in photoresponse with a photocurrent density of 1 mA/cm² at +1.0 V, which is even superior to that of other ZnO-based or TiO₂-based photoanodes in recent reports.[135-137,143,144] Significantly, there is a saturation of photocurrent at more positive potential observed in carbon-modified ZnO inverse opals, indicating efficient charge separation induced by the surface modification of ZnO with carbon upon illumination. The reason could be attributed to the formation of oxygen vacancies resulted from carbon incorporation into ZnO framework via XAS results. The proposed schematic diagram of charge-transfer process in our system is illustrated in Figure 8.6. The oxygen vacancies may work as electron acceptors and trap the photogenerated electrons temporarily to reduce the surface recombination of electrons and holes. Here, the oxygen vacancies can be considered to be the active sites of the ZnO photoanode. Furthermore, in order to quantitatively explore the photoactivity of carbon-modified ZnO inverse opals, the efficiency (η) of photon-to-hydrogen generation is calculated by an equation in

which the contribution due to applied potential is subtracted from the total efficiency.[137] The plot of efficiency versus applied potential (Figure 8.4c) shows the maximum value of efficiency is 0.75% at an applied potential of +0.3 V, which is higher than the recent reported values for ZnO-based or TiO₂-based photoanodes.[136,137,143] Last but not least, the advantage of carbon-modified ZnO inverse opals is further exemplified by the good stability (a minimal degradation rate of only 7% after 5 h of continuous running) in the photo-oxidation process at pH = 7 (Figure 8.4d). The photogenerated holes are the dominant roles for ZnO materials during photocorrosion reaction. In our system, the photogenerated holes rapidly transferring to the solution for water-oxidation reaction may successfully facilitate the inhibition of the photocorrosion due to high efficiency of charge separation induced by carbon modification of ZnO structures. Therefore, the merit of the cooperative effect, i.e. optical amplification and surface hybridization, can be unambiguously highlighted here via IPCE, linear sweep voltammograms, photon-to-hydrogen efficiency, and stability data.

8.4 Summary

We have successfully demonstrated an easy-to-fabricated route to directly prepare carbon-modified ZnO inverse opals on the ITO substrate as photoanodes. While hierarchical inverse-opal nanoarchitectures enthrall the idea of increasing the optical path length of solar light for optical amplification, there exists a wealth of carbon

modifications that can independently enhance the separation of photoinduced electron-hole pairs, visible-light absorption, and photostability for ZnO photoanode. It is anticipated that this model hybrid photoanode will enable us to design high-activity, high-stability, visible-light-driven photoelectrodes in the future.



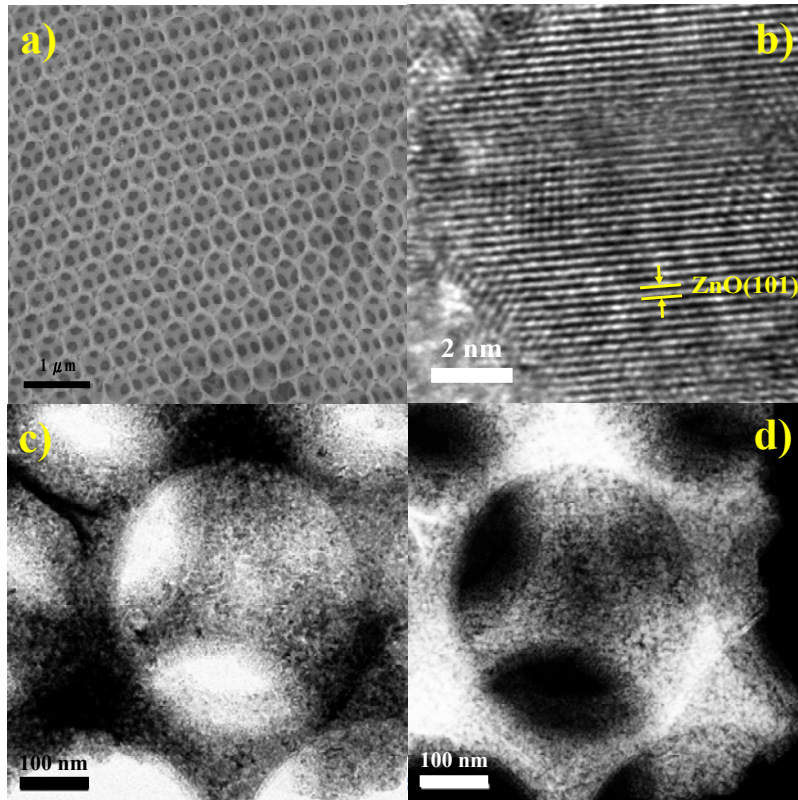


Figure 8.1 (a) SEM image and (b) HRTEM image of carbon-modified ZnO inverse opals. (c) Bright-field and (d) Z-contrast TEM images of carbon-modified ZnO inverse opals.

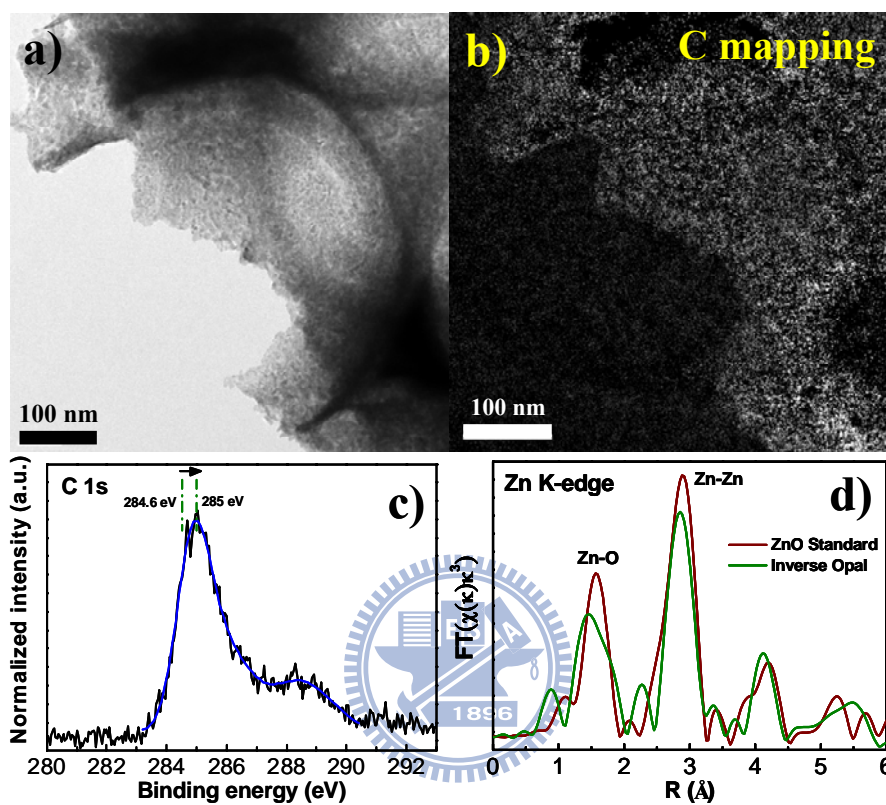


Figure 8.2 (a) Typical TEM image of carbon-modified ZnO inverse opals. Corresponding energy-filtered TEM (b) carbon mapping image of carbon-modified ZnO inverse opals. (c) XPS spectrum of C 1s peak of carbon-modified ZnO inverse opals. (d) Zn K-edge EXAFS spectra of carbon-modified ZnO inverse opals and pure ZnO structures.

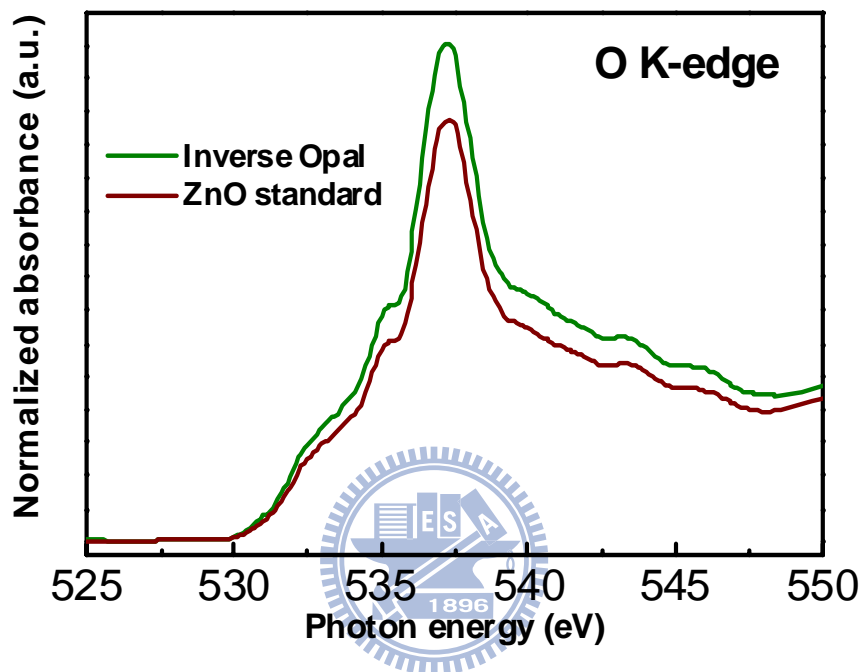


Figure 8.3 O K-edge XAS spectra of carbon-modified ZnO inverse opals and pure ZnO structures.

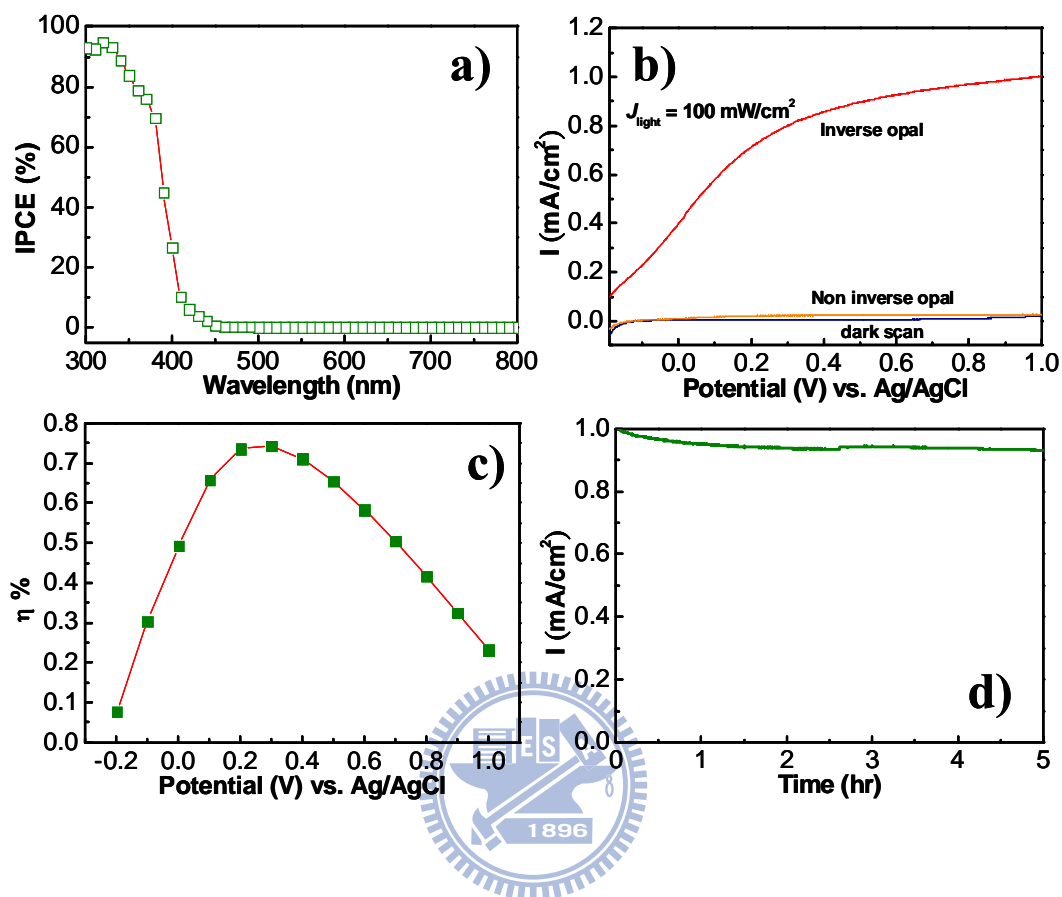


Figure 8.4 (a) Measured IPCE spectra of carbon-modified ZnO inverse opals in the region of 300 to 800 nm at a potential of +0.25 V (vs. Pt) in two-electrode system. (b) Linear sweep voltammograms, collected at a scan rate of 10 mV/s at applied potentials from -0.19 to +1.0 V (vs. Ag/AgCl) for carbon-modified ZnO inverse opals in the dark, ZnO noninverse-opal structures, and carbon-modified ZnO inverse opals at 100 mW/cm². (c) Photoconversion efficiency of the PEC cell with carbon-modified ZnO inverse opal photoelectrode as a function of applied potential. (d) Amperometric I-t curves of the carbon-modified ZnO inverse opals collected at a potential of +1.0 V (vs. Ag/AgCl) for 5 h.

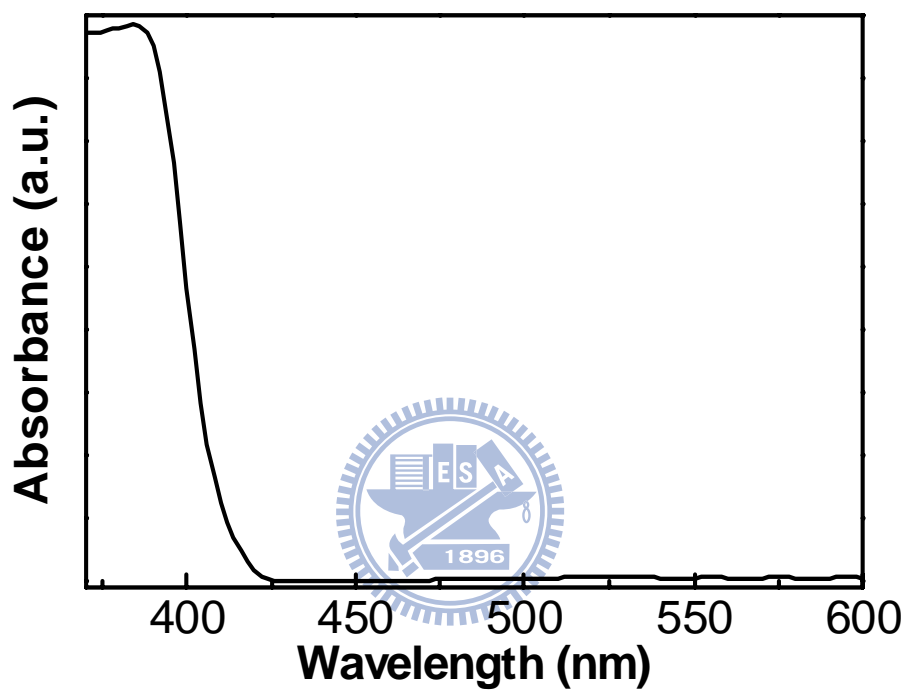


Figure 8.5 UV-vis spectra of carbon-modified ZnO inverse opals showing a slight red shift of absorption wavelength to the visible region.

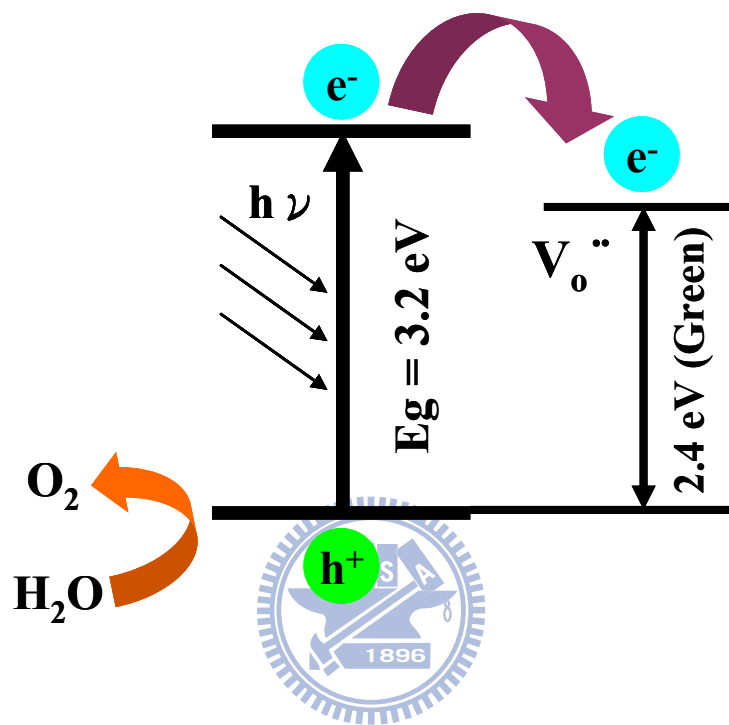


Figure 8.6 Schematic diagram representing the charge-transfer process of the carbon-modified ZnO inverse opals.

Chapter 9

Conclusions

9.1 Effects of Nitrogen-Doping on the Microstructure, Bonding and Electrochemical Activity of Carbon Nanotubes

Vertically aligned CN_x NTs have been synthesized using microwave plasma enhanced chemical vapor deposition with different nitrogen flow rate. The results show that nitrogen incorporation provides a simple pathway to engineering/modifying the microstructure and electronic bonding structure, which is crucial to the ET kinetics of the CN_x NT electrode. *In-situ* N doping of the CNTs at an optimal 3.5 at. % N is effective in promoting substitutional graphite-like defect structure, which is favorable for fast ET in electrochemistry.

9.2 Novel Copper-Zinc Oxide Nanoarchitectures as Microreformation Catalysts for Hydrogen Production

Firstly, we have successfully demonstrated an easy-to-fabricate route to prepare arrayed ZnO NR@Cu NP heterostructures on the inner surface of microchannels. The superb catalytic performance and stability of the Cu NP-decorated ZnO NR nanostructures can be attributed to the larger surface area and enhanced dispersion of fine Cu NPs, formation of microstrain, the modification of electronic structure of

Cu species, and the existence of SMSI effect.

Secondly, we have demonstrated an effective MW-treatment technique to enhance the catalytic activity of CuO NT/ZnO NR nanostructures for MRR. It is believed that formation of defects, microstrains and SMSI due to the selective heating by MW-treatment may have contributed to such enhancement in catalyst performance.

Thirdly, we have successfully demonstrated an easy route to fabricate a novel CuO-ZnO catalyst with well-defined inverse opal nanostructure on the inner surface of microchannels. The V_o -rich Cu-ZnO inverse opal obtained in this study at a low-reaction temperature of only 230 °C yields complete conversion methanol, high hydrogen production rate ($300 \text{ mmol g}_{\text{cat}}^{-1} \text{ h}^{-1}$), low CO formation (130-170 ppm), and outstanding stability (after continuous 80 hours of operation), making it exceedingly promising toward MRR.

9.3 Enhanced Photocatalytic Activity with Carbon-Modified ZnO Inverse Opals for Solar Water-Splitting

We have successfully demonstrated an easy-to-fabricated route to directly prepare carbon-modified ZnO inverse opals on the ITO substrate as photoanodes. While hierarchical inverse-opal nanoarchitectures enthrall the idea of increasing the optical path length of solar light for optical amplification, there exists a wealth of carbon modifications that can independently enhance the separation of photoinduced

electron-hole pairs, visible-light absorption, and photostability for ZnO photoanode.



References

- [1] M. Z. Jacobson, W. G. Colella, D. M. Golden, *Science* **2005**, 308, 1901.
- [2] B. C. H. Steele, A. Heinzl, *Nature* **2001**, 414, 345.
- [3] P. Thounthong, B. Davat, S. Rael, P. Sethakul, *IEEE Ind. Electron. Mag.* **2009**, 3, 32.
- [4] A. M. Zainoodin, S. K. Kamarudin, W. R. W. Daud, *Int. J. Hydrogen Energy* **2010**, 35, 4606.
- [5] S. Basri, S. K. Kamarudin, W. R. W. Daud, Z. YaaRub, *Int. J. Hydrogen Energy* **2010**, 35, 7957.
- [6] C. L. Sun, L. C. Chen, M. C. Su, L. S. Hong, O. Chyan, C. Y. Hsu, K. H. Chen, T. F. Chang, L. Chang, *Chem. Mater.* **2005**, 17, 3749.
- [7] L. C. Chen, C. Y. Wen, C. H. Liang, W. K. Hong, K. J. Chen, H. C. Cheng, C. S. Shen, C. T. Wu, K. H. Chen, *Adv. Funct. Mater.* **2002**, 12, 687.
- [8] B. M. Klein, *Nature* **1999**, 399, 108.
- [9] J. C. Carrero-Sanchez, A. L. Elias, R. Mancilla, G. Arrellin, H. Terrones, J. P. Laclette, M. Terrones, *Nano Lett.* **2006**, 6, 1609.
- [10] G. Abbas, P. Papakonstantinou, G. R. S. Iyer, I. W. Kirkman, L. C. Chen, *Phys. Rev. B* **2007**, 75, 195429.
- [11] Z. Y. Deng, J. M. F. Ferreira, Y. Sakka, *J. Am. Ceram. Soc.* **2008**, 91, 3825.
- [12] S. Sa, H. Silva, L. Brandao, J. M. Sousa, A. Mendes, *Appl. Catal. B: Environ.* **2010**, 99, 43.
- [13] Y. Choi, H. G. Stenger, *J. Power Sources* **2005**, 142, 81.
- [14] R. Becker, H. Parala, F. Hipler, O. P. Tkachenko, K. V. Klementiev, W. Grünert, H. Wilmer, O. Hinrichsen, M. Muhler, A. Birkner, C. Wöll, S. Schäfer, R. A. Fischer, *Angew. Chem. Int. Ed.* **2004**, 43, 2839.
- [15] T. Ressler, B. L. Kniep, I. Kasatkin, R. Schlögl, *Angew. Chem. Int. Ed.* **2005**, 44, 4704.
- [16] S. Vukojević, O. Trapp, J. D. Grunwaldt, C. Kiener, F. Schüth, *Angew. Chem. Int. Ed.* **2005**, 44, 4978.

- [17] I. Kasatkin, P. Kurr, B. Kniep, A. Trunschke, R. Schlögl, *Angew. Chem. Int. Ed.* **2007**, *46*, 7324.
- [18] L. C. Wang, Y. M. Liu, M. Chen, Y. Cao, H. Y. He, G. S. Wu, W. L. Dai, K. N. Fan, *J. Catal.* **2007**, *246*, 193.
- [19] E. N. Muhamad, R. Irmawati, Y. H. Taufiq-Yap, A. H. Abdullah, B. L. Kniep, F. Girgsdies, T. Ressler, *Catal. Today* **2008**, *131*, 118.
- [20] M. Pagliaro, A. G. Konstandopoulos, R. Ciriminna, G. Palmisano, *Energy Environ. Sci.* **2010**, *3*, 279.
- [21] L. J. Minggu, W. R. W. Daun, M. B. Kassim, *Int. J. Hydrogen Energy* **2010**, *35*, 5233.
- [22] S. Dutta, *Int. J. Hydrogen Energy* **1990**, *15*, 379.
- [23] K. Honda, A. Fujishima, *Nature* **1972**, *238*, 37.
- [24] A. J. Bard, M. A. Fox, *Acc. Chem. Res.* **1995**, *28*, 141.
- [25] N. S. Lewis, *Nature* **2001**, *414*, 589.
- [26] Y. Li, J. Z. Zhang, *Laser Photonic Rev.* **2010**, *4*, 517.
- [27] M. Baldauf, W. Preidel, *J. Power Sources* **1999**, *84*, 161.
- [28] A. Kuver, W. Vielstich, *J. Power Sources* **1998**, *74*, 211.
- [29] S. K. Kamarudin, W. R. W. Daud, S. L. Ho, U. A. Hasran, *J. Power Sources* **2007**, *163*, 743.
- [30] G. W. Yang, G. Y. Gao, G. Y. Zhao, H. L. Li, *Carbon* **2007**, *45*, 3036.
- [31] J. W. Guo, T. S. Zhao, J. Prabhuram, R. Chen, C. W. Wong, *Electrochem. Acta* **2005**, *51*, 754.
- [32] T. Fujigaya, M. Okamoto, N. Nakashima, *Carbon* **2009**, *47*, 3227.
- [33] J. Prabhuram, T. S. Zhao, Z. X. Liang, R. Chen, *Electrochem. Acta* **2007**, *52*, 2649.
- [34] L. Schlapbach, A. Züttel, *Nature* **2001**, *414*, 353.
- [35] D. R. Palo, R. A. Dagle, J. D. Holladay, *Chem. Rev.* **2007**, *107*, 3992.
- [36] A. S. Patil, T. G. Dubois, N. Sifer, E. Bostic, K. Gardner, M. Quah, C. Bolton, *J. Power Sources* **2004**, *136*, 220.

- [37] Q. F. Li, R. H. He, J. O. Jensen, N. J. Bjerrum, *Chem. Mater.* **2003**, *15*, 4896.
- [38] J. K. Lee, J. B. Ko, D. H. Kim, *Appl. Catal. A* **2004**, *278*, 25.
- [40] R. van de Krol, Y. Q. Liang, J. Schoonman, *J. Mater. Chem.* **2008**, *18*, 2311.
- [41] T. Bak, J. Nowotny, M. Rekas, C. C. Sorrell, *Int. J. Hydrogen Energy* **2002**, *27*, 991.
- [42] S. U. M. Khan, M. Al-Shahry, W. B. Ingler, *Science* **2002**, *297*, 2243.
- [43] O. Khaselev, J. A. Turner, *Science* **1998**, *280*, 425.
- [44] R. Hoyle, J. Sotomayor, G. Will, D. Fitzmaurice, *J. Phys. Chem. B* **1997**, *101*, 10791.
- [45] S. U. M. Khan, J. Akikusa, *J. Electrochem. Soc.* **1998**, *145*, 89.
- [46] S. U. M. Khan, J. Akikusa, *J. Phys. Chem. B* **1999**, *103*, 7184.
- [47] T. Lindgren, H. L. Wang, N. Beermann, L. Vayssieres, A. Hagfeldt, S. E. Lindquist, *Sol. Energy Mater. Sol. Cells* **2002**, *71*, 231.
- [48] N. Beermann, L. Vayssieres, S. E. Lindquist, A. Hagfeldt, *J. Electrochem. Soc.* **2000**, *147*, 2456.
- [49] S. Saito, *Science* **1997**, *278*, 77.
- [50] G. Che, B. B. Lakshmi, E. R. Fisher, C. R. Martin, *Nature* **1998**, *393*, 346.
- [51] S. Agrawal, M. J. Frederick, F. Lupo, P. Victor, O. Nalamasu, G. Ramanath, *Adv. Funct. Mater.* **2005**, *15*, 1922.
- [52] A. A. Mamedov, N. A. Kotov, M. Prato, D. M. Guldi, J. P. Wicksted, A. Hirsch, *Nat. Mater.* **2002**, *1*, 190.
- [53] A. Javey, Q. Wang, A. Ural, Y. Li, H. Dai, *Nano Lett.* **2002**, *2*, 929.
- [54] A. Cao, R. Baskaran, M. J. Frederick, K. Turner, P. M. Ajayan, G. Ramanath, *Adv. Mater.* **2003**, *15*, 1105.
- [55] K. Keren, R. S. Berman, E. Buchstab, U. Sivan, E. Braun, *Science* **2003**, *302*, 1380.
- [56] N. Chopra, M. Majumder, B. J. Hinds, *Adv. Funct. Mater.* **2005**, *15*, 858.
- [57] A. Gomathi, S. R. C. Vivekchand, A. Govindaraj, C. N. R. Rao, *Adv. Mater.* **2005**, *17*, 2757.

- [58] C. L. Sun, H. W. Wang, M. Hayashi, L. C. Chen, K. H. Chen, *J. Am. Chem. Soc.* **2006**, *128*, 8368.
- [59] D. Shi, J. Lian, W. Wang, G. Liu, P. He, Z. Dong, L. Wang, R. C. Ewing, *Adv. Mater.* **2006**, *18*, 189.
- [60] M. S. Raghuvver, A. Kumar, M. J. Frederick, G. P. Louie, P. G. Ganesan, G. Ramanath, *Adv. Mater.* **2006**, *8*, 547.
- [61] C. H. Wang, H. Y. Du, Y. T. Tsai, C. P. Chen, C. J. Huang, L. C. Chen, K. H. Chen, H. C. Shih, *J. Power Sources* **2007**, *171*, 55.
- [62] W. C. Fang, K. H. Chen, L. C. Chen, *Nanotechnology* **2007**, *18*, 485716.
- [63] S. S. Wong, E. Joselevich, A. T. Woolley, C. L. Cheung, C. M. Lieber, *Nature* **1998**, *394*, 52.
- [64] R. J. Chen, Y. Zhang, D. Wang, H. Dai, *J. Am. Chem. Soc.* **2001**, *123*, 3838.
- [65] B. M. Quinn, C. Dekker, S. G. Lemay, *J. Am. Chem. Soc.* **2005**, *127*, 6146.
- [66] D. G. McCulloch, S. Praver, A. Hoffman, *Phys. Rev. B* **1994**, *50*, 5905.
- [67] J. Kastner, T. Pichler, H. Kuzmany, S. Curran, W. Blau, D. N. Weldon, M. Delamesiere, S. Draper, H. Zandbergen, *Chem. Phys. Lett.* **1994**, *221*, 53.
- [68] J. W. Jang, C. E. Lee, S. C. Lyu, T. J. Lee, C. J. Lee, *Appl. Phys. Lett.* **2004**, *84*, 2877.
- [69] C. Ronning, H. Feldermann, R. Merk, H. Hofsass, *Phys. Rev. B* **1998**, *58*, 2207.
- [70] J. P. Zhao, Z. Y. Chen, T. Yano, T. Ooie, M. Yoneda, J. Sakakibara, *J. Appl. Phys.* **2001**, *89*, 1634.
- [71] H. Ago, T. Kugler, F. Cacialli, W. R. Salaneck, M. S. P. Shaffer, A. H. Windle, R. H. Friend, *J. Phys. Chem. B* **1999**, *103*, 8116.
- [72] J. H. Mohr, W. Schmickler, *Phys. Rev. Lett.* **2000**, *84*, 1051.
- [73] P. M. Ajayan, *Chem. Rev.* **1999**, *99*, 1787.
- [74] J. F. Evans, T. Kuwana, *Anal. Chem.* **1977**, *49*, 1632.
- [75] R. R. Davda, J. A. Dumesic, *Angew. Chem. Int. Ed.* **2003**, *42*, 4068.
- [76] G. A. Deluga, J. R. Salge, L. D. Schmidt, X. E. Verykios, *Science* **2004**, *303*, 993.

- [77] B. L. Kniep, T. Ressler, A. Rabis, F. Girgsdies, M. Baenitz, F. Steglich, R. Schlögl, *Angew. Chem. Int. Ed.* **2004**, *43*, 112.
- [78] B. Frank, F. C. Jentoft, H. Soerijanto, J. Kröhnert, R. Schlögl, R. Schomäcker, *J. Catal.* **2007**, *246*, 177.
- [79] O. J. Kwon, S. M. Hwang, J. H. Chae, M. S. Kang, J. J. Kim, *J. Power Sources* **2007**, *165*, 342.
- [80] J. S. Suh, M. T. Lee, R. Greif, C. P. Grigoropoulos, *J. Power Sources* **2007**, *173*, 458.
- [81] A. Stefanescu, A. C. van Veen, C. Mirodatos, J. C. Beziat, E. Duval-Brunel, *Catal. Today* **2007**, *125*, 16.
- [82] Y. Kawamura, N. Ogura, T. Yamamoto, A. Igarashi, *Chem. Eng. Sci.* **2006**, *61*, 1092.
- [83] A. Kundu, J. E. Ahn, S. S. Park, Y. G. Shul, H. S. Han, *Chem. Eng. J.* **2008**, *135*, 113.
- [84] L. Vayssieres, *Adv. Mater.* **2003**, *15*, 464.
- [85] C. Bock, C. Paquet, M. Couillard, G. A. Botton, B. R. MacDougall, *J. Am. Chem. Soc.* **2004**, *126*, 8028.
- [86] C. D. Wagner, W. M. Riggs, L. E. Davis, J. F. Mouler, *Handbook of X-Ray Photoelectron Spectroscopy*, Perkin Elmer Corporation, MN, **1979**.
- [87] S. Velu, K. Suzuki, C. S. Gopinath, *J. Phys. Chem. B* **2002**, *106*, 12737.
- [88] D. Grandjean, H. L. Castricum, J. C. Heuvel, B. M. Weckhuysen, *J. Phys. Chem. B* **2006**, *110*, 16892.
- [89] C. Z. Yao, L. C. Wang, Y. M. Liu, G. S. Wu, Y. Cao, W. L. Dai, H. Y. He, K. N. Fan, *Appl. Catal. A: Gen.* **2006**, *297*, 151.
- [90] M. Turco, G. Bagnasco, C. Cammarano, P. Senese, U. Costantino, M. Sisani, *Appl. Catal. B: Environ.* **2007**, *77*, 46.
- [91] M. Law, L. E. Greene, J. C. Johnson, R. Saykally, P. Yang, *Nat. Mater.* **2005**, *4*, 455.
- [92] R. Si, M. Flytzani-Stephanopoulos, *Angew. Chem. Int. Ed.* **2008**, *47*, 2884.
- [93] Y. G. Lin, Y. K. Hsu, C. T. Wu, S. Y. Chen, K. H. Chen, L. C. Chen, *Diamond & Relat. Mater.* **2009**, *18*, 433.

- [94] F. Raimondi, G. G. Scherer, R. Kötz, A. Wokaun, *Angew. Chem. Int. Ed.* **2005**, *44*, 2190.
- [95] J. C. Frost, *Nature* **1988**, *334*, 577.
- [96] P. H. Matter, D. J. Braden, U. S. Ozkan, *J. Catal.* **2004**, *223*, 340.
- [97] Y. K. Lin, Y. H. Su, Y. H. Huang, C. J. Hsu, Y. K. Hsu, Y. G. Lin, K. H. Huang, S. Y. Chen, K. H. Chen, L. C. Chen, *J. Mater. Chem.* **2009**, *19*, 9186.
- [98] Y. G. Lin, Y. K. Hsu, S. Y. Chen, L. C. Chen, K. H. Chen, *J. Mater. Chem.* **2010**, DOI: 10.1039/c0jm02605k.
- [99] B. L. Kniep, F. Girgsdies, T. Ressler, *J. Catal.* **2005**, *236*, 34.
- [100] Y. G. Lin, Y. K. Hsu, S. Y. Chen, Y. K. Lin, L. C. Chen, K. H. Chen, *Angew. Chem. Int. Ed.* **2009**, *48*, 7586.
- [101] B. L. Hayes, *Microwave Synthesis: Chemistry at the Speed of Light*, CEM Publishing: Matthews, NC, 2003.
- [102] C. O. Kappe, *Angew. Chem. Int. Ed.* **2004**, *43*, 6250.
- [103] T. A. Nissinen, Y. Kiros, M. Gasik, M. Leskelä, *Chem. Mater.* **2003**, *15*, 4974.
- [104] D. D. Young, J. Nichols, R. M. Kelly, A. Deiters, *J. Am. Chem. Soc.* **2008**, *130*, 10048.
- [105] C. J. Ko, Y. K. Lin, F. C. Chen, *Adv. Mater.* **2007**, *19*, 3520.
- [106] Y. Li, B. Tan, Y. Wu, *Chem. Mater.* **2008**, *20*, 567.
- [107] N. Ashkenov, B. N. Mbenkum, C. Bundesmann, V. Riede, M. Lorenz, D. Spemann, E. M. Kaidashev, A. Kasic, M. Schubert, M. Grundmann, G. Wagner, H. Neumann, V. Darakchieva, H. Arwin, B. Monemar, *J. Appl. Phys.* **2003**, *93*, 126.
- [108] T. Yu, X. Zhao, Z. X. Shen, Y. H. Wu, W. H. Su, *J. Cryst. Growth* **2004**, *268*, 590.
- [109] L. Seyfried, F. Garin, G. Maire, J. M. Thiebaut, G. Roussy, *J. Catal.* **1994**, *148*, 281.
- [110] K. J. Rao, B. Vaidhyanathan, M. Ganguli, P. A. Ramakrishnan, *Chem. Mater.* **1999**, *11*, 882.
- [111] A. Stein, F. Li, N. R. Denny, *Chem. Mater.* **2008**, *20*, 649.

- [112] I. -K. Sung, Christian, M. Mitchell, D. -P. Kim, P. J. A. Kenis, *Adv. Funct. Mater.* **2005**, *15*, 1336.
- [113] G. Guan, R. Zapf, G. Kolb, Y. Men, V. Hessel, H. Loewe, J. Ye, R. Zentel, *Chem. Commun.* **2007**, 260.
- [114] G. A. Umeda, W. C. Chueh, L. Noailles, S. M. Haile, B. S. Dunn, *Energy Environ. Sci.* **2008**, *1*, 484.
- [115] T. Ishida, M. Haruta, *Angew. Chem. Int. Ed.* **2007**, *46*, 7154.
- [116] J. D. Holladay, Y. Wang, E. Jones, *Chem. Rev.* **2004**, *104*, 4767.
- [117] V. Meille, *Appl. Catal. A* **2006**, *315*, 1.
- [118] S. Vukojević, O. Trapp, J. D. Grunwaldt, C. Kiener, F. Schüth, *Angew. Chem. Int. Ed.* **2005**, *44*, 7978.
- [119] J. A. Rodriguez, P. Liu, J. Hrbek, J. Evans, M. Pérez, *Angew. Chem. Int. Ed.* **2007**, *46*, 1329.
- [120] C. T. Campbell, C. H. F. Peden, *Science* **2005**, *309*, 713.
- [121] J. Papavasiliou, G. Avgouropoulos, T. Ioannides, *Appl. Catal. B: Environ.* **2007**, *69*, 226.
- [122] Z. Y. Pu, X. S. Liu, A. P. Jia, Y. L. Xie, J. Q. Lu, M. F. Luo, *J. Phys. Chem. C* **2008**, *112*, 15045.
- [123] C. H. Liang, Z. Q. Ma, H. Y. Lin, L. Ding, J. S. Qiu, W. Frandsen, D. S. Su, *J. Mater. Chem.* **2009**, *19*, 1417.
- [124] P. K. Giri, S. Bhattacharyya, D. K. Singh, R. Kesavamoorthy, B. K. Panigrahi, K. G. M. Nair, *J. Appl. Phys.* **2007**, *102*, 093515.
- [125] H. F. Goldstein, D. S. Kim, P. Y. Yu, L. C. Bourne, *Phys. Rev. B* **1990**, *41*, 7192.
- [126] B. J. Coppa, R. F. Davis, R. J. Nemanich, *Appl. Phys. Lett.* **2003**, *82*, 400.
- [127] K. H. Tam, C. K. Cheung, Y. H. Leung, A. B. Djurisić, C. C. Ling, C. D. Beling, S. Fung, W. M. Kwok, W. K. Chan, D. L. Phillips, L. Ding, W. K. Ge, *J. Phys. Chem. B* **2006**, *110*, 20865.
- [128] J. B. K. Law, J. T. L. Thong, *Nanotechnology* **2008**, *19*, 205502.
- [129] N. Laosiripojana, S. Assabumrungrat, *Appl. Catal. B: Environ.* **2008**, *82*, 103.

- [130] C. Bozo, N. Guilhaume, J. M. Herrmann, *J. Catal.* **2001**, *203*, 393.
- [131] T. X. T. Sayle, S. C. Parker, C. R. A. Catlow, *Surf. Sci.* **1994**, *316*, 329.
- [132] S. Nishimura, N. Abrams, B. A. Lewis, L. I. Halaoui, T. E. Mallouk, K. D. Benkstein, J. van de Lagemaat, A. J. Frank, *J. Am. Chem. Soc.* **2003**, *125*, 6306.
- [133] J. I. L. Chen, G. von Freymann, S. Y. Choi, V. Kitaev, G. A. Ozin, *Adv. Mater.* **2006**, *18*, 1915.
- [134] K. Sivula, R. Zboril, F. Le Formal, R. Robert, A. Weidenkaff, J. Tucek, J. Frydrych, M. Gratzel, *J. Am. Chem. Soc.* **2010**, *132*, 7436.
- [135] K. S. Ahn, Y. Yan, S. Shet, K. Jones, T. Deutsch, J. Turner, M. Al-Jassim, *Appl. Phys. Lett.* **2008**, *93*, 163117.
- [136] A. Wolcott, W. A. Smith, T. R. Kuykendall, Y. Zhao, J. Z. Zhang, *Adv. Funct. Mater.* **2009**, *19*, 1849.
- [137] X. Yang, A. Wolcott, G. Waang, A. Sobo, R. C. Fitzmorris, F. Qian, J. Z. Zhang, Y. Li, *Nano Lett.* **2009**, *9*, 2331.
- [138] E. Hendry, M. Koeberg, B. O'Regan, M. Bonn, *Nano Lett.* **2006**, *6*, 755.
- [139] M. A. Fox, M. T. Dulay, *Chem. Rev.* **1993**, *93*, 341.
- [140] H. Zhang, R. Zong, Y. Zhu, *J. Phys. Chem. C* **2009**, *113*, 4605.
- [141] Y. Li, X. Zhou, X. Hu, X. Zhao, P. Fang, *J. Phys. Chem. C* **2009**, *113*, 16188.
- [142] S. Krishnamurthy, C. McGuinness, L. S. Dorneles, M. Venkatesan, J. M. D. Coey, J. G. Lunney, C. H. Patterson, K. E. Smith, T. Learmonth, P. A. Glans, T. Schmitt, J. H. Guo, *J. Appl. Phys.* **2006**, *99*, 08M111.
- [143] A. Wolcott, W. A. Smith, T. R. Kuykendall, Y. Zhao, J. Z. Zhang, *Small* **2009**, *5*, 104.
- [144] Y. J. Hwang, A. Boukai, P. D. Yang, *Nano Lett.* **2009**, *9*, 410.

Curriculum Vitae

Name : Yan-Gu Lin

11.01.1980 Born in Taichung (Taiwan)

1998-2002 Undergraduate study in the department of materials science and engineering at Feng Chia University

2002-2004 Graduate study in the department of materials science and engineering at Feng Chia University



2004-2010 PhD study in the department of materials science and engineering at Chiao Tung University

PhD Thesis : Study on One-Dimensional N-doped CNT and Three-Dimensional Cu/ZnO Nanostructures for Electrochemical Characteristics and Hydrogen Production Applications

Publications

Yan-Gu Lin

SCI Paper

1. **Y. G. Lin**, Y. K. Hsu, S. Y. Chen, L. C. Chen, and K. H. Chen, “*Microwave-Activated CuO Nanotip/ZnO Nanorod Nanoarchitectures for Efficient Hydrogen Production*” **Journal of Material Chemistry** (in press,2010). (IF:4.795)
2. Y. K. Hsu, Y. C. Chen, **Y. G. Lin**, L. C. Chen, and K. H. Chen, ”*Reversible phase transformation of MnO₂ nanosheets in an electrochemical capacitor investigated by in situ Raman spectroscopy*” **Chemical Communications** (in press,2010). (IF:5.504)
3. **Y. G. Lin**, Y. K. Hsu, S. Y. Chen, L. C. Chen, and K. H. Chen, “*O₂ Plasma-activated CuO-ZnO Inverse Opals as High-performance Methanol Microreformer*” **Journal of Material Chemistry** (in press,2010). (IF:4.795)
4. **Y.G. Lin**, Y.K. Hsu, Y.K. Lin, S.Y. Chen, K.H. Chen, and L.C. Chen, “*Novel Nanostructured ZnO Nanorod@Cu Nanoparticle Catalysts for Microreformer Devices*” **Angewandte Chemie International Edition**, Vol. 48, pp7586-7590 (2009) (IF:11.829)
5. Y.K. Lin, Y.H. Su, Y.H. Huang, C.J. Hsu, Y.K. Hsu, **Y. G. Lin**, K. H. Huang, S. Y. Chen, L.C. Chen, and K.H. Chen, “*Efficient Hydrogen Production Using Cu-based Catalysts Prepared via Homogeneous Precipitation*” **Journal of Material Chemistry**, Vol. 19, pp9186-9194 (2009) (IF: 4.795).
6. C.L. Sun, Y.K. Hsu, C. Bock, **Y.G. Lin**, E. A. Baranova, X.H. Wu, L.C. Chen, K.H. Chen, and B. MacDougall, “*Ternary PtRuNi Nanocatalysts Supported on N-doped Carbon Nanotubes: Deposition Process, Materials Characterization, and Electrochemistry*” **Journal of The Electrochemical Society**, Vol. 156,

ppB1249-B1252 (2009) (IF: 2.437)

7. Y.K. Hsu, J.L. Yang, **Y.G. Lin**, S.Y. Chen, L.C. Chen, and K.H. Chen, “*Efficient Synthesis of PtRu/CNTs/Carbon Cloth Electrode for the Anodic Oxidation of Methanol*” **Diamond and Related Materials**, Vol. 18, pp557-562 (2009) (IF: 2.092)
8. **Y.G. Lin**, Y.K. Hsu, C.T. Wu, S.Y. Chen, K.H. Chen, and L.C. Chen, “*Effects of nitrogen-doping on the microstructure, bonding and electrochemical activity of carbon nanotubes*” **Diamond and Related Materials**, Vol.18, pp433-437 (2009) (IF: 2.092)
9. **Y.G. Lin**, Y.K. Hsu, S.Y. Chen, K.H. Chen, and L.C. Chen, “*Novel Copper-Zinc Oxide Arrayed Nanoatalysts for Hydrogen Production Applications*” **ECS Transactions**, Vol. 13, pp165-168 (2008)

International Conferences

Oral

1. **Y.G. Lin**, Y.K. Hsu, S.Y. Chen, L.C. Chen, and K.H. Chen, **2010**, “*Novel Copper-Zinc Oxide Nanoarchitectures as Microreformation Catalysts for Hydrogen Production*”, **217th ECS Meeting**, April 26-30, Vancouver, Canada.
2. **Y.G. Lin**, Y.K. Hsu, S.Y. Chen, L.C. Chen, and K.H. Chen, **2009**, “*Morphological Control of Catalytically Active Cu-ZnO Nanostructures for Hydrogen Generation*” **EMRS Spring Meeting**, Jun. 8-12, Strasbourg, France.
3. **Y.G. Lin**, Y.K. Hsu, S.Y. Chen, L.C. Chen, and K.H. Chen, **2008**, “*Binary Nanostructures for Hydrogen Generation*” **Pre-Symposium of 14th International Congress on Catalysis**, Jul. 8-12, Kyoto, Japan.
4. **Y.G. Lin**, Y.K. Hsu, Y.K. Lin, C.N. Chuang, S.Y. Chen, L.C. Chen, and K.H. Chen, **2008**, “*Novel Copper-Zinc Oxide Arrayed Nanoatalysts for Hydrogen Production Applications*” **213th ECS Meeting**, May 18-22, Phoenix, USA.

5. **Y.G. Lin**, Y.K. Hsu, J.L. Yang, S.Y. Chen, K.H. Chen, and L.C. Chen, **2007**,
“*Electrocatalytic activity and structural studies of nitrogen doping effects on array multi-walled carbon nanotube electrodes*” **54th AVS Meeting**, Oct. 14-19, Seattle, USA.
6. J.L. Yang, Y.K. Hsu, **Y.G. Lin**, S.Y. Chen, L.C. Chen, and K.H. Chen, **2007**,
“*Synthesis and Optimization of Pt-Ru/CN_xNTs/CC nanocatalysts for methanol electro-oxidation*” **211th ECS Spring Meeting**, May 6-10, Chicago, USA.

Poster

1. Y.K. Hsu, **Y.G. Lin**, L.C. Chen, and K.H. Chen, **2008**, “*Enhanced stability of Pt nanocatalysts on carbon nanotubes electrode by H₂ plasma treatment for methanol electro-oxidation*” **2^{ed} International conference on New Diamond and Nano Carbons**, May 26-29, Taipei, Taiwan.
2. **Y.G. Lin**, Y.K. Hsu, J.L. Yang, C.H. Wang, H.Y. Du, W.C. Wang, J.H. Huang, H.C. Shih, S.Y. Chen, K.H. Chen, and L.C. Chen, **2008**, “*Modification of CNTs for Fuel Cell and Capacitor Application*” **2^{ed} International conference on New Diamond and Nano Carbons**, May 26-29, Taipei, Taiwan.
3. C.L. Sun, Y.K. Hsu, C. Bock, **Y.G. Lin**, E.A. Baranova, X.H. Wu, K.H. Chen, L.C. Chen, and B. MacDougall, **2008**, “*PtRuNi Full-Cell Electrocatalysts Supported by N-doped Carbon Nanotubes*” **2^{ed} International conference on New Diamond and Nano Carbons**, May 26-29, Taipei, Taiwan.
4. Y.K. Hsu, W.H. Su, **Y.G. Lin**, J.L. Yang, C.L. Sun, S.Y. Chen, C.R. Lin, K.H. Chen, and L.C. Chen, **2006**, “*Ternary PtRuNi Nanocatalysts Dispersed on Multiwall Carbon Nanotubes for Methanol Electro-oxidation in Acid Medium*” **MRS Fall Meeting**, Nov. 27 - Dec. 1, Boston, USA.

Award

1. **2006** 年，[能源與光電薄膜科技研討會暨國科會專題計畫研究成果發表會](#)，**壁**

報論文獎。作者：Y.G. Lin, Y.K. Hsu, Y.H. Hsieh, Y.K. Lin, T. Mathew, K.H. Chen, L.C. Chen, and S.Y. Chen。題目：Oxidative steam reforming of methanol over Cu/ZnAlGa-oxide catalysts for the production of hydrogen for fuel cells: catalyst characterization and performance evaluation。

2. **2009 MRS Fall Meeting "SCIENCE AS ART" 2nd Place Winner**, Boston, USA.

